

## Solid oxygen revisited

Yu.A. Freiman

*Verkin Institute for Low Temperature Physics and Engineering, 47 Prospect Nauky, 61103  
Kharkov, Ukraine  
E-mail:yuri.afreiman@gmail.com; freiman@ilt.kharkov.ua*

H.J. Jodl

*Fachbereich Physik, Universität Kaiserslautern,  
Erwin Schrödinger Strasse, D67663 Kaiserslautern, Germany  
European Laboratory for Nonlinear Spectroscopy (LENs),  
University of Florence, Via Carrara 1, I-50019 Florence, Italy  
E-mail:jodl@physik.uni-kl.de; jodl@lens.unifi.it*

Yanier Crespo

*International Center for Theoretical Physics (ICTP), IT-34014 Trieste, Italy  
E-mail:yaniercr@hotmail.com*

### Contents

1	Introduction	3
2	Low-temperature phase diagram	7
3	$\epsilon$ phase	9
3.1	Structure and properties of the $\epsilon$ phase	9
3.2	The nature of the chemical bond in the $\epsilon$ phase	15
4	$\zeta$ phase	23
4.1	$\epsilon - \zeta$ (insulator-metal) phase transition	23
4.2	Raman and single-crystal x-ray studies of the $\zeta$ phase	24
4.3	Persistence of oxygen molecules up to terapascal pressures	31
5	High-pressure high-temperature part of the phase diagram	32

5.1	Structure and properties of the $\eta$ phase	32
5.2	Phase transition to the $\eta'$ phase	37
6	Magnetic properties	43
6.1	Magnetic structure of the $\alpha$ phase	43
6.2	Giant magneto-volume effect	45
6.3	Susceptibility measurements under pressure	46
6.4	Magnetic properties of the $\delta$ phase	50
6.5	Magnetic collapse at the $\delta$ - $\epsilon$ transition	60
6.6	Magnetic properties of the $\epsilon$ phase	63
7	High-pressure high-temperature melting line	78
8	Solid oxygen in ultrahigh magnetic fields	82
8.1	Introductory remarks	82
8.2	Magnetization measurements	83
8.3	Magneto-transmission measurements	84
8.4	$H - T$ phase diagram	87
8.5	Concluding remarks	89
9	Summary and outlook	90
	References	93

*The paper provides an up-to-date review of the experimental and theoretical works on solid oxygen published over the past decade.*

*The most important results presented in this review are the following: Detection of magnetic collapse in neutron studies under the delta-epsilon transition.*

*Identification of the lattice structure of the  $\epsilon$  phase. In this structure the  $O_2$  molecules retain their individuality, but there is an additional link leading to the formation of clusters of molecular quartets with the structural formula  $(O_2)_4$ .*

*Discovery of the unique magnetic properties of the delta phase, which hosts three different magnetic structures in the domain of the same crystallographic structure.*

*The extension of the phase diagram to the high-pressure high-temperature region which was previously beyond the reach for experiment; the molecular  $\eta$  and  $\eta'$  phases were found and their structures were identified.*

*Behavior of the melting line up to 60 GPa (1750 K).*

*Discovery of a new molecular  $\theta$  phase in ultrahigh magnetic fields up to over 190 T and the construction of the thermodynamical magnetic-field-temperature  $H$ - $T$  phase diagram on the base of the ultrahigh-field magnetization, optical magneto-transmission, and adiabatic magnetocaloric effect measurements.*

*Prediction of the persistence of the molecular state of solid oxygen up to the pressure of 1.9 TPa which is significantly higher than the corresponding limits in solid hydrogen and nitrogen, other generic molecular solids.*

## **1 Introduction**

The phase diagrams of the three simplest diatomic crystals - hydrogen, nitrogen and oxygen, exhibit the majority of phenomena exemplified by the vast diversity of condensed matter substances. These include pressure and temperature induced structure transitions, pressure induced metallization and superconductivity, pressure induced polymerization, amorphization and molecular dissociation. That is why these solids with their structural simplicity are the best testing ground for accurate theoretical treatment. Together with these common phenomena each generic substance exhibit also some phenomena which make their phase diagrams quite individual. In the case of hydrogen, this is the existence of several spin-nuclear modifications and as a consequence numerous ortho - para effects. In the case of nitrogen, this is the triple chemical bond between the atoms in the nitrogen molecule. In the case of oxygen this is magnetism and as a result a very rich and complex phase diagram.

Oxygen is the third most abundant element in nature, after hydrogen and helium, and the most abundant element in the Earth's crust and oceans. Investigations of the properties of oxygen are an essential part of all natural sciences - Physics, Chemistry and Biology. The discovery of oxygen is usually attributed to Carl Wilhelm Scheele (Sweden), Joseph Priestley (Great Britain), and Antoine Lavoisier (France) [1]. The name "Oxygen" was proposed by Lavoisier. The dramatic issue of priority of this discovery is a subject of the play "Oxygen" by Carl Djerassi and Roald Hoffmann [2]. Faraday discovered that the oxygen molecule possesses a nonzero magnetic moment [3] which makes oxygen in gas, liquid, and solid modifications the only elemental magnetic system. Condensed oxygen was first obtained by the Polish physicists Wroblewski and Olszewski at the end of the XIX-th century (see [1]). The first study of solid oxygen - measuring of the solidification temperature was also performed in

Poland [4] at the very beginning of the XX-th century. As a magnetic system solid oxygen is unique in that the magnetic contribution to the binding energy is competitive in value with the van der Waals contribution. This finding of the Kharkov group [5–7] made it possible to reconcile the apparent contradictions between results of magnetic [8,9] and heat capacity studies [10,11]. The competition between the two major contributions to the ground-state energy leads to a strong interplay between magnetic, structural, and molecular orientational degrees of freedom, and results in a very rich phase diagram. At present, the existence of at least nine solid-state phase is established; the  $P$ - $T$  phase diagram of solid oxygen is studied up to pressures of over 130 GPa and temperatures over 1500 K [12–14]. As follows from the *ab initio* calculations [15], the molecular state survives up to 1.9 TPa (1 TPa =  $10^3$  GPa).

Starting from the earliest studies solid oxygen has been a playground of solid state physics. It displays a large variety of key solid-state phenomena, including quantum and anharmonic effects, low-dimensional effects, many-body effects, the interplay between different order parameters, temperature- and pressure-induced phase transitions like pressure-induced magnetic collapse, pressure-induced insulator-metal transition, pressure-induced superconductivity.

A comprehensive review of studies of solid oxygen [7] published in 2004 gives a sufficiently complete picture of the state of studies of structural, thermodynamic, optical and magnetic properties, performed throughout the twentieth century (the list of cited works includes more than 400 references). After the review, it seemed to us that the situation in this field of research can be described by a phrase well known in the history of physics, <sup>\*</sup> saying, "in this field, almost everything is already discovered, and all that remains is to fill a few holes". In reality, during the decade since the publication of this review, a large number of important findings were made in physics of solid oxygen (see Table 1). The progress in the field is in a considerable way due to instrumental developments in high pressure physics and technique in 1990s and 2000s, including high-pressure neutron technique, high-pressure magnetic susceptibility measurements technique, the technique of ultrahigh (100 T range) magnetic fields, the technique developed for high-pressure high-temperature studies of highly reactive (like hydrogen and oxygen) substances, etc.

The most important results that will be presented in this review are the following:

- The identification of the lattice structure of the  $\epsilon$  phase [17,18]. The efforts of nearly three decades of identifying the lattice structure of  $\epsilon$ -O<sub>2</sub> culminated in simultaneous publication in 2006 of results of x-ray diffraction diamond anvil cell experiments of the two groups. They discovered that in addition to the well-known O<sub>2</sub> and O<sub>3</sub> molecules existing in the free state, in solid oxygen pressurized up to 8 GPa a new modification of oxygen exists, which can be described by the structural formula (O<sub>2</sub>)<sub>4</sub>. In this structure the O<sub>2</sub> molecules retain their individuality, but there is an additional link leading to the formation of clusters of molecular quartets.

---

<sup>\*</sup> The Munich physics professor Philipp von Jolly advised Planck against going into physics [16]

Table 1  
Chronology of studies of solid oxygen 2004 - 2017

Date	Type of studies and main results	Authors
2004	First comprehensive review article	Yu. Freiman, H. Jodl [7]
	First neutron studies of the $\alpha$ , $\beta$ , and $\delta$ phases	I. Goncharenko et al. [27]
	First observation of the $\eta$ phase	M. Santoro et al. [12]
2005	Magnetic collapse in $\epsilon$ phase	I. Goncharenko [21]
	Raman, and IR study of $\alpha - \beta$ and $\alpha - \delta$ transitions.	J. Kreutz et al. [28]
2006	$O_8$ structure of the $\epsilon$ phase (single-crystal study)	L. Lundegaard et al. [17]
	$O_8$ structure of the $\epsilon$ phase (polycrystal study)	H. Fujihisa et al. [18]
2007	Melting line at high pressure	G. Weck et al. [29]
	$\epsilon - \zeta$ transition (theory)	Y. Ma et al. [30]
	Magnetoelastic nature of the $\epsilon$ phase	E. Gomonay, V. Loktev [31]
	Rhomboid $O_8$ molecules in solid oxygen	R. Steudel, M.W. Wong [32]
2008	IR study of magnetic properties	F. Gorelli et al. [33]
	Inelastic X-ray scattering of dense solid oxygen	Yue Meng et al. [34]
	Structurally induced insulator-metal transition	D.Y. Kim et al. [35]
	Bonding in the $\epsilon$ phase	J. Tse et al. [36]
	Identification of melting at high pressures	L.R. Benedetti et al. [37]
2009	Magnetism and vibrations in the $\epsilon$ phase	T. Anh Pham et al. [38]
	Single-crystal x-ray diffraction, structure of $\eta$ - $O_2$	L. Lundegaard et al. [19]
	Metallic $\zeta$ phase	G. Weck et al. [13]
	Mechanisms of pressure-induced phase transitions	H. Katzke, P. Tolédano [39]
2010	Magnetic structures in $\delta$ phase	S. Klotz et al. [20]
	Theory of magnetic properties of the $\delta$ phase	E. Gomonay, V. Loktev [40]
2011	First observation of the $\eta'$ phase	A. Goncharov et al. [14]
	Molecular oxygen tetramer	M. Bartolomei et al. [41]
2012	Persistence of oxygen molecules up to TPa pressures	J. Sun et al. [15]
	First-principle study on superconductivity	T. Ishikawa et al. [42]
2013	Chemical interaction and spin structure of $(O_2)_4$ .	M. Garcia-Revilla et al. [43]
2014	Novel phase induced by ultrahigh magnetic field	T. Nomura et al. [22]
	Magnetic susceptibility measurements up to 3.3 GPa	M. Mito et al. [44]
	Collective spin 1 singlet high-pressure phase	Y. Crespo et al. [45]

Table 2

Table 1 continued

Date	Type of studies and main results	Authors
2015	Raman and IR modes in $\epsilon$ and $\zeta$ phases	A. Ochoa-Calle et al. [46]
	Magnetic properties of solid oxygen under pressure	Yu. Freiman [47]
2016	Crystal structure in TPa regime	B. Cogollo-Olivo, J. Montoya [48]
2017	Antiferromagnetic vs. nonmagnetic $\epsilon$ phase	A. Ramires-Solis et al. [49]
	Magnetic-field - temperature phase diagram	T. Nomura et al. [25]
2018	Magnetism studied by neutron diffraction (review article)	S. Klotz [115]
	Solid oxygen revisited (review article)	Yu. Freiman et al. [142]

- The extension of the phase diagram to the high-pressure high-temperature range [12,14,19]; the discovery of the high-pressure high-temperature molecular  $\eta$  and  $\eta'$  phases and the identification of their structures. Previous static high-pressure studies of solid oxygen have been mostly limited to room or low temperatures because of highly reactive nature of oxygen under high temperature conditions.

- The measurements of the melting line up to 60 GPa (1750 K).

- The existence of three different magnetic structures was identified by Klotz et al. in the neutron study Ref. [20] in the domain of the  $\delta$  phase, called respectively HTC (high temperature commensurate), ITC(intermediate temperature commensurate), and LTC (low temperature commensurate).

- The magnetic collapse at the  $\delta - \epsilon$  transition identified in the neutron study by Goncharenko [21].

- Experimental studies of solid oxygen in ultrahigh pulsed destructive magnetic fields of up to over 190 T performed by Nomura *et al. group* [22–26]. The thermodynamical magnetic-field-temperature  $H$ - $T$  phase diagram of solid oxygen is discussed analyzing the results of the ultrahigh-field magnetization, optical magneto-transmission, and adiabatic magnetocaloric effect measurements.

- The persistence of molecular oxygen to about 1.9 TPa [15], predicted on the base of density-functional-theory calculations. This is more than an order of magnitude higher than molecular nitrogen, another generic molecular solid.

The paper provides an up-to-date review of the experimental and theoretical papers on solid oxygen published in the recent decade.

## 2 Low-temperature phase diagram

To date, the  $P$ – $T$  phase diagram of solid oxygen (Fig. 1) has been investigated in the region of pressures up to 140 GPa, temperatures up to 1750 K, and magnetic fields up to over 100 T. The existence of at least nine ( $\alpha$ ,  $\beta$ ,  $\gamma$ ,  $\delta$ ,  $\epsilon$ ,  $\zeta$ ,  $\eta$ ,  $\eta'$ ,  $\theta$ ) solid state phases have been established. At a pressure of 100 GPa and room temperatures, oxygen is transformed into a metallic state, which becomes superconducting at  $T_c = 0.6$  K [50]. Ab initio calculations [15] have shown that the molecular state is maintained up to 1.9 TPa.

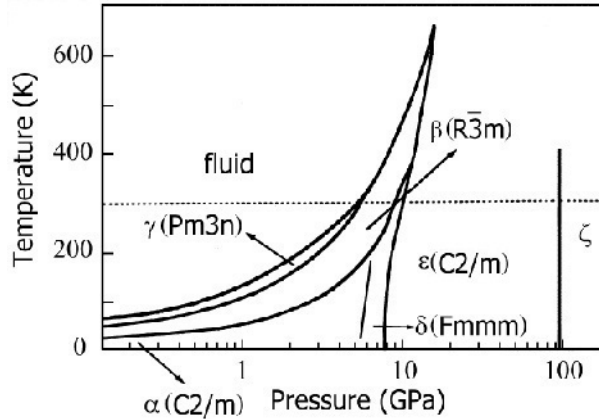


Fig. 1. Low-pressure low-temperature part of the phase diagram of solid oxygen. (From Ref. [7].)

For completeness we consider in this section structures of  $\alpha$  (Fig. 2 Left),  $\beta$  (Fig. 3),  $\gamma$  (Fig. 4), and  $\delta$  (Fig. 2 Right) phases which were discussed in detail in the review [7]. A detailed review of studies of the properties of solid oxygen in Ref. [7], published in 2004, gives a fairly complete picture of the state of research on its structural, thermodynamic, optical and magnetic properties, conducted throughout the twentieth century (the list of cited works contains more than 400 references). The crystal structure of low-temperature  $\alpha$  and  $\beta$  phases has been first determined in x-ray studies by Barrett et al. [51]. The fact that oxygen possesses magnetic properties has been first discovered by Faraday, who has found that gaseous oxygen is paramagnetic [3]. The paramagnetic nature of liquid oxygen has been found by Dewar [52]. Magnetic ordering in the low-temperature  $\alpha$  phase has been first proposed by Giauque and Johnston [53] based on entropy considerations and then confirmed in neutron diffraction studies by Alikhanov [54,55] and Collins [56]. Collins has also found that there is no long-range magnetic order in the  $\beta$  phase, however strong short-range magnetic order exists [56].

The first study of oxygen at pressures up to 10 GPa using diamond anvil has been conducted by Nicol et al. [57]. They have found a new phase, which has been dubbed "orange  $O_2$ " due to its characteristic orange color, and following the already known low-pressure phases  $\alpha$ -,  $\beta$  -, and  $\gamma$ - $O_2$ , designated as  $\delta$ - $O_2$ . The structure of this phase (Fig. 2 Right) has been identified as  $Fmmm$  in the x-ray study conducted at room

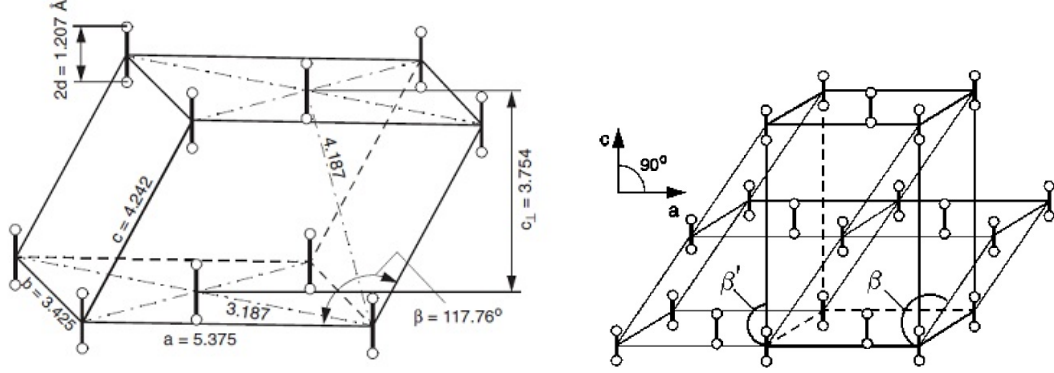


Fig. 2. Structure of  $\alpha$ -O<sub>2</sub> (left) and structure of  $\delta$ -O<sub>2</sub> (right). (From Ref. [7].)

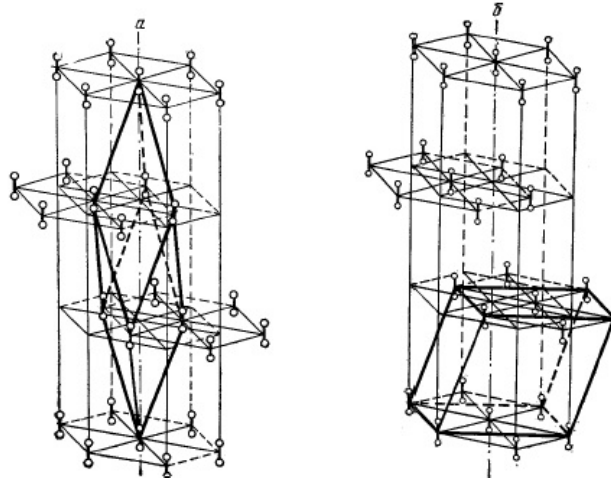


Fig. 3. Structure of  $\beta$ -O<sub>2</sub> in rhombohedral (left) and monoclinic (right) axes. (From Refs. [6,7].)

temperature by Schiferl et al. [58]. The transformation of the monoclinic  $\alpha$  phase into the orthorhombic  $\delta$  phase occurs through a small shift of the close-packed  $ab$ -planes. The spatial structure remains quasi-two-dimensional, and in both phases the centers of gravity of the molecules are located at the nodes of weakly deformed hexagonal cells. At the point of  $\alpha - \delta$  transition, the angle  $\beta'$  (Fig. 2 Right) becomes  $90^\circ$ . An important feature of  $\alpha$ -,  $\beta$ -, and  $\delta$ -O<sub>2</sub>, is the parallel arrangement of the molecules, which is commonly explained by the strong contribution of the exchange interaction to the anisotropic part of the intermolecular potential. Besides discovering the  $\delta$  phase, the same paper [57] was the first to describe the visual observation of the  $\delta - \epsilon$  phase transition. At room temperature and pressure of about 10 GPa, solid oxygen changes the color from light orange of  $\delta$ -O<sub>2</sub> to the deep red color of a new phase, which has been designated as  $\epsilon$ -O<sub>2</sub>. The region of stability of "red oxygen" extends up to a pressure of 96 GPa, where the transition to a non-magnetic metal  $\zeta$  phase occurs. The arrangement of the molecules in the  $\zeta$  phase is still unknown.

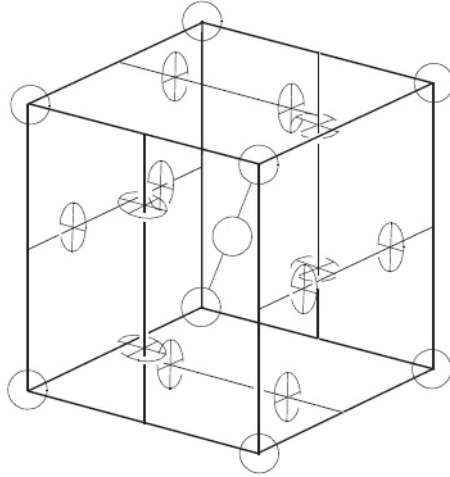


Fig. 4. Structure of  $\gamma$ -O<sub>2</sub>. (From Ref. [7].)

### 3 $\epsilon$ phase

#### 3.1 Structure and properties of the $\epsilon$ phase

At room temperatures the light orange crystal of  $\delta$ -O<sub>2</sub> at approximately 10 GPa transforms to dark red  $\epsilon$ -O<sub>2</sub>. The  $\epsilon$  phase was discovered by Nicol, Hirsch, and Holzapfel in 1979 [57] in the first loading the diamond anvil cell for experiments with oxygen. A radical transformation of the lattice at the  $\delta - \epsilon$  transition is evidenced by a giant volume jump amounting 5-6 % at room temperatures [59,60], the appearance of a strong infrared absorption [61,62], the dramatic color change to dark red, and magnetic collapse [21]. Evidently, a kind of pressure-induced Peierls distortion takes place at this transition. The very substantial density increase not only favors the formation of  $\epsilon$ -O<sub>2</sub> at high pressure but is also responsible for its stability over a remarkably large range of pressures.

Discussing the nature of the  $\delta - \epsilon$  phase transition the Florence-Kaiserslautern group (R. Bini, F. Gorelli, H. Jodl, M. Santoro) put forward the hypothesis that this transition is caused by a molecular association of the O<sub>2</sub> molecules into diamagnetic O<sub>4</sub> units (Refs. [63–66]). Two main arguments supporting this hypothesis (see Secs. 5.3.4, 5.3.4, and 8.3.3 from Ref. [7]) were obtained from the spectroscopy: a large infrared activity of  $\epsilon$ -O<sub>2</sub> (see Fig. 68 in Ref. [7]), and the disappearing of the  ${}^3\Sigma_g^- \rightarrow {}^1\Delta_g$  (0-0) and (0-1) electronic transitions at

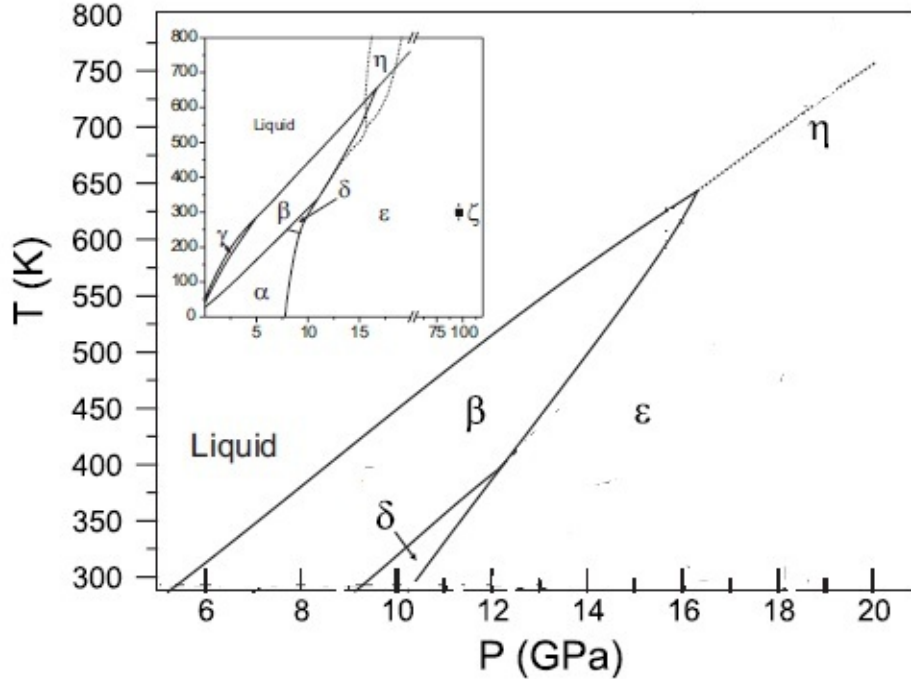


Fig. 5. Phase diagram of oxygen to 20 GPa and 800 K. The solid lines show the phase boundaries as reported by Yen and Nicol Ref. [68]. The inset shows the extended phase diagram of oxygen to 120 GPa and 800 K (Refs. [68,69,74]). In both the main figure and the inset, the dotted line is the extension to the melting line that reported by Weck et al. [29], while the dashed lines show the phase boundaries between the liquid,  $\delta$ ,  $\beta$ , and  $\eta$  phases proposed by Santoro et al. [12]. (Modified from Ref. [19].)

the  $\delta - \epsilon$  transformation (Fig. 133 in Ref. [7]). As will be shown in the next section, the association actually takes place but not two, but four molecules of oxygen.

The  $\epsilon$  phase takes up a largest part of the investigated range of the phase diagram (Fig. 5) extending from the  $\delta - \epsilon$  transition line which starts at  $\sim 7.6$  GPa at zero temperature [67] and continues to higher temperatures as the  $\beta - \epsilon$  ( $T_{\delta\epsilon\beta} = 386 \pm 5$  K,  $P_{\delta\epsilon\beta} = 11.5 \pm 0.3$  GPa [68]) and  $\eta - \epsilon$  ( $T_{\beta\epsilon\eta} = 540 \pm 20$  K,  $P_{\beta\epsilon\eta} = 15.7 \pm 0.2$  GPa [12]) phase transition lines. Starting from the  $\eta - \eta' - \epsilon$  triple point ( $T_{\eta\eta'\epsilon} \approx 700$  K,  $P_{\eta\eta'\epsilon} \approx 20$  GPa [14]) the range of the  $\epsilon$  phase is bound by the weakly pressure dependent  $\eta' - \epsilon$  transition line. From the high-pressure side at  $P > 96$  GPa it is bound by the metallic  $\zeta$  phase [69,70,60].

Within one month in 2006 two groups (Fujihisa et al. [18], August 2006 and Lundegaard et al. [17], September 2006) published data about the hitherto unknown crystallographic structure of the  $\epsilon$  phase. The first group used a powder-like sample of  $O_2$  [18], the other one worked

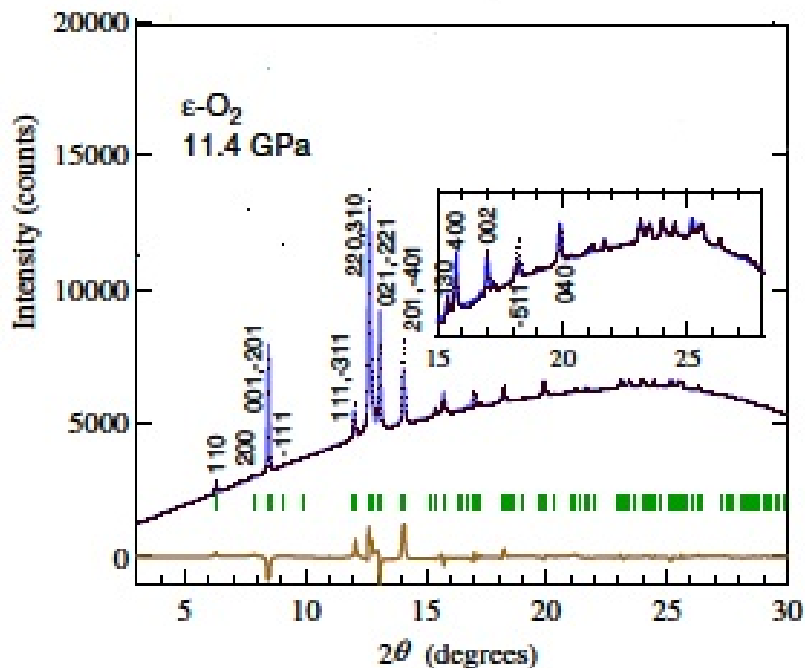


Fig. 6. (color online). Observed diffraction pattern of  $\epsilon$ -O<sub>2</sub> at 11.4 GPa (dots) and the calculated profile (curve) after the Rietveld refinement. The insets show enlarged views of the high angle part of the patterns. (Modified from Ref. [18].)

with a single crystal sample of O<sub>2</sub> [17]. Both groups used similar experimental equipment: synchrotron x-ray diffraction in combination with CCD area detectors to monitor diffraction pattern, a DAC to produce high pressure and ruby scale to determine local pressure. Fujihisa et al. covered the pressure range from 4 to 100 GPa while Lundegaard et al. studied the pressure range 13 - 18 GPa. Sample preparation of two groups was different: the powder-like sample of solid O<sub>2</sub> of the Japanese group was produced by cryoloading the DAC; the joint Scotland-French-Canadian group used a single crystal of  $\epsilon$  oxygen grown from a 8.6 mol.% O<sub>2</sub> in He mixture at 450 K and 22.5 GPa.

The quality of the diffraction data obtained by the Japanese group can be seen in Fig. 6. Rietveld analysis delivered both the atomic coordinates and the lattice parameters  $a, b, c, \beta$  (Fig. 7a), and molar volume (Fig. 7b). The lattice parameters of the  $\epsilon$  phase shown in Fig. 7(a, b) agree at low pressures with the known data in literature of the  $\delta$  phase and at high pressure with the data for the  $\zeta$  phase. The molar

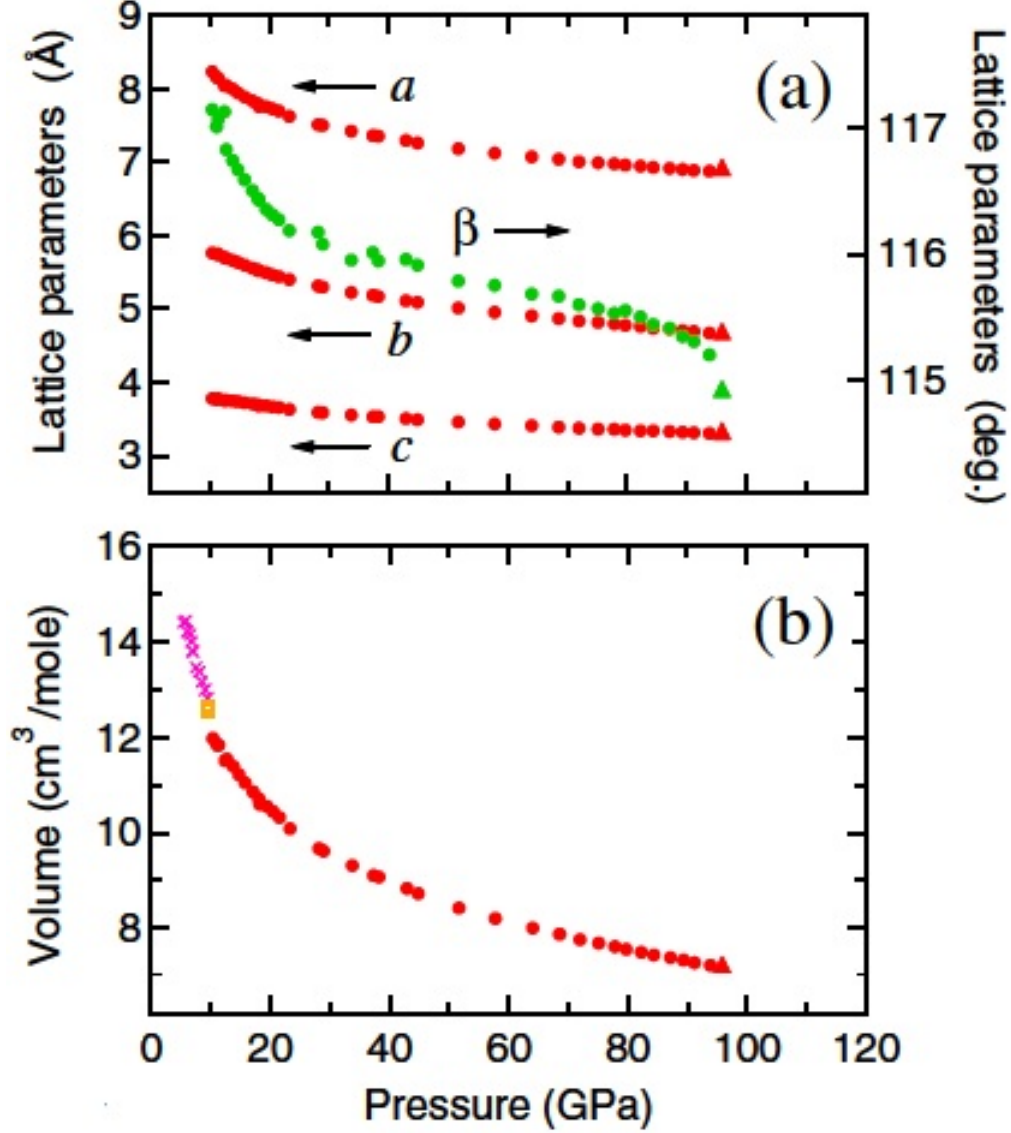


Fig. 7. (color online). Pressure dependence of the structural parameters of  $\epsilon$ -O<sub>2</sub>: (a) the lattice parameters  $a$ ,  $b$ ,  $c$ , and  $\beta$ , (b) the molar volume. Triangles at 96 GPa in (a) and (b) are single crystal work data from Ref. [71]. Cross marks and open squares in (b) represent the data for  $\beta$ -O<sub>2</sub> and  $\delta$ -O<sub>2</sub>. (Modified from Ref. [18].)

volume jumps at the  $\beta - \delta$  and  $\delta - \epsilon$  first order phase transitions are 1.6% and 5.4%, respectively. In the  $\epsilon$  phase when pressure increases from 10 GPa to 95 GPa the molar volume reduced by 40% (Fig. 7b). In the behavior of the monoclinic angle  $\beta$  (Fig. 7a) there are three different pressure ranges. From 10 GPa to 25 GPa  $\beta$  decreases rather rapidly; in the range 25 – 80 GPa  $\beta$  decreases very slowly but above 80 GPa it drops with increasing rate which can be considered as a precursor for the transition to the  $\zeta$  phase at 96 GPa [18].

Results of these studies revealed a unique structure of the  $\epsilon$  phase

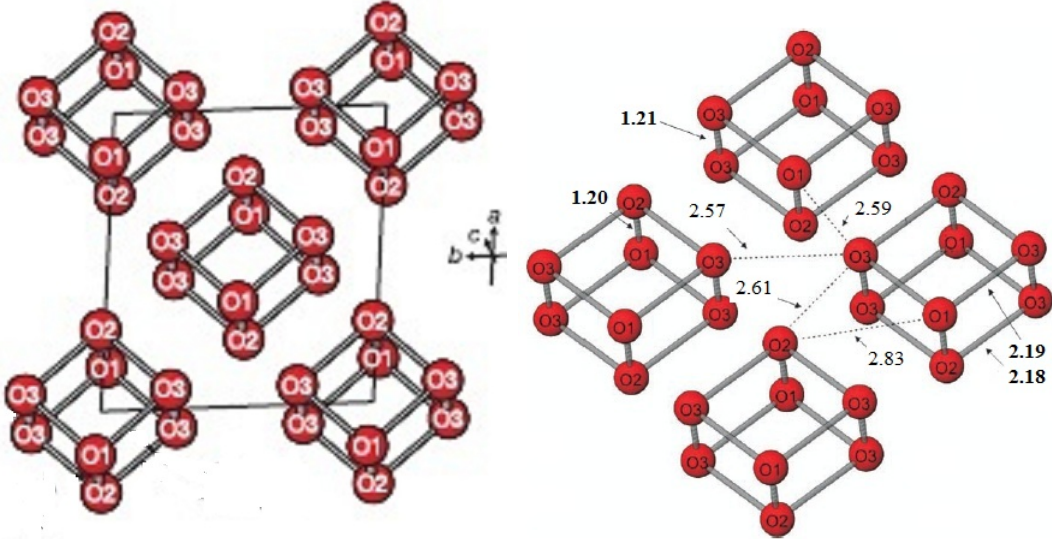


Fig. 8. (color online). The structure of  $\epsilon$ -oxygen as viewed perpendicular to the  $ab$  plane. Left: the groups of molecules forming the  $(\text{O}_2)_4$  units are connected by thick lines. Right: The inter- and intra  $\text{O}_8$ -molecular distances at 17.6 GPa (in  $\text{\AA}$ ). (Modified from Ref. [17].)

in which  $\text{O}_2$  molecules preserve their individuality, but an additional weak chemical bond results in the formation of clusters of molecular quartets. The structure of the  $\epsilon$  phase, as viewed perpendicular to the  $ab$  plane, is shown in Fig. 8. In the description of the structure we will be closely following the single-crystal study Ref. [17]. As in the  $\beta$  and  $\delta$  phases [75,76,7],  $\epsilon$ - $\text{O}_2$  comprise layers of collinear  $\text{O}_2$  molecules, the axes of which within  $1^\circ$  are oriented perpendicular to the layers which lie in the  $ab$  plane. The layers comprise two types of  $\text{O}_2$  molecules — those containing two symmetry-equivalent O3 atoms and the centers of which are constrained by symmetry to lie exactly in the  $ab$  planes at  $z = 0$  and  $z = 1$ , and those comprising symmetry-inequivalent O1 and O2 atoms, and the centers of which are unconstrained. The symmetry of the structure does not require that the O-O bond lengths of the O3-O3 and O1-O2 molecules be the same, nor that the molecules be oriented perpendicular to the  $ab$  plane. However, the bond lengths of all the  $\text{O}_2$  molecules are the same  $1.20(3) \text{ \AA}$  within error at all pressures, which is in good agreement with the O-O bond length in the gas phase ( $1.207 \text{ \AA}$ ) [7].

It should be noted that the structures obtained from the different studies [17,18] are not completely identical: the single-crystal data [17] yield a more complete refinement of the atomic positions compared with the powder method. The important difference is that the molec-

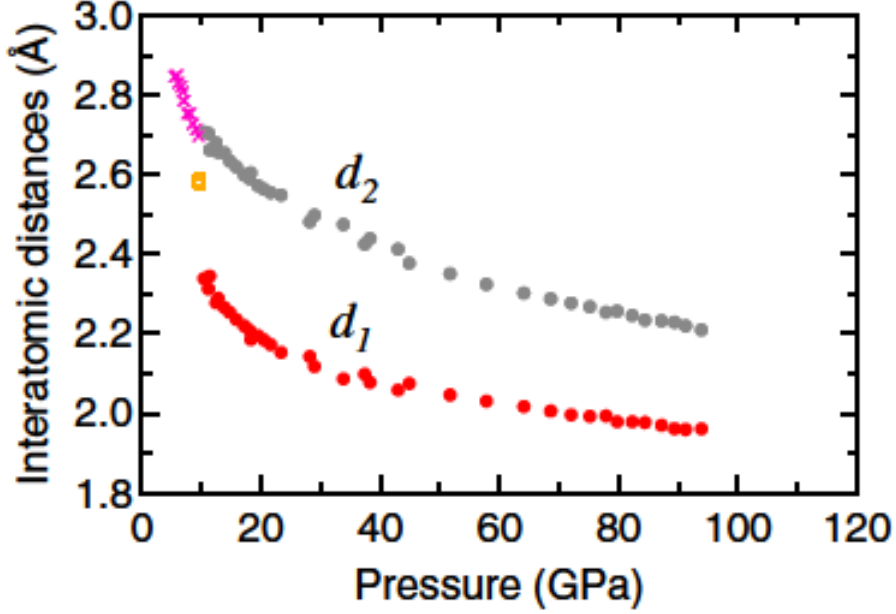


Fig. 9. (color online). Pressure dependence of the shortest intermolecular distance inside the  $O_8$  unit ( $d_1$ ) and the shortest intermolecular distance between the nearest  $O_8$  units ( $d_2$ ). Cross marks and open squares represent the data for  $\beta$ - $O_2$  and  $\delta$ - $O_2$ . (Modified from Ref. [18].)

ular axis in the powder diffraction  $O_8$  units are slightly nonorthogonal to the  $ab$  planes.

The pressure dependencies of the shortest intermolecular distances inside the  $O_8$  units ( $d_1$ ) and the shortest intermolecular distances between the nearest  $O_8$  units ( $d_2$ ) are shown in Fig. 9. The crosses and open squares indicate the intermolecular distances  $d_1$  and  $d_2$  for the  $\beta$  and  $\delta$  phases where they are degenerate. As can be seen,  $d_1$  in the  $\epsilon$  phase is significantly shorter than the distances in the  $\beta$  and  $\delta$  phases. It is this contraction which leads to the large volume reduction of 5.4% at the  $\delta - \epsilon$  transition and is responsible for the appearance of the  $O_8$  cluster in the  $\epsilon$  phase. From the behavior of the lattice parameters  $d_1$  and  $d_2$  (Fig. 9) at pressures close to the  $\delta - \epsilon$  phase transition Fujihisa *et al* [18] concluded that the  $O_8$  units are formed directly at this phase transition. The  $d_2$  decreases to 2.2 Å at 95 GPa. This value is comparable to the  $d_1$  at 15 GPa and is short enough for the electron orbitals to overlap. This fact suggests that the transition to the  $\zeta$  phase may occur by the connection of  $O_8$  clusters. Localized electrons in the  $O_8$  cluster would spread in the  $ab$  plane and result in a two-dimensional metallic state.

The striking feature of the structure is the association of four  $O_2$  molecules into rhomb-shaped  $(O_2)_4$  molecular units, which are symmetry equivalent and centered on the lattice points at  $(0,0,0)$  and  $(0.5,0.5,0)$ . In contrast to the structures of the  $\alpha$ -,  $\beta$ -, and  $\delta$ -phases, the distances between the  $O_2$  units within these layers are not equal, but distinct rhomboid-shaped  $O_8$  unit in the form  $(O_2)_4$  of the  $D_{2h}$  symmetry can be identified with three characteristic shortest distances: 1.2 – 1.21 Å within the  $O_2$  units, 2.18 – 2.19 Å between two nearest neighboring  $O_2$  units within the  $O_8$  molecules, and 2.57 – 2.61 Å between neighboring  $O_8$  units (see Fig. 8 (Right)) [17]. The shortest interlayer distance is 2.50 Å. (For comparison, the van der Waals distance between two oxygen atoms is 3.04 Å (van der Waals radius of oxygen atom is 1.52 Å.) The characteristic bond angles in the  $O_8$  units are:  $84^\circ$  ( $\angle O3-O1-O3$  and  $\angle O3-O2-O3$ ),  $96^\circ$  ( $\angle O1-O3-O2$ ), and  $90^\circ$  (e.g.  $\angle O3-O1-O2$ ). Thus, it has been found that, in addition to well-known molecules  $O_2$  (oxygen) and  $O_3$  (ozone) existing in a free state in solid oxygen under pressure of  $\sim 8$  GPa there exists one more oxygen molecule which can be described by the structural formula  $(O_2)_4$ . It should be stressed "that the remarkable formation of the  $O_8$  species in solid oxygen is the first case in which compression of an element results in a novel small molecule that was not observed or even speculated about before [32]" .

### 3.2 *The nature of the chemical bond in the $\epsilon$ phase*

Why does this structure form? Generally, there are two opposite patterns which chemical bonds undergo under high pressure: the most typical phenomenon is a pressure-driven dissociation when the chemical bonds in a solid break under high pressure. In the case of molecular diatomic solids like nitrogen or iodine the molecules dissociate into atoms which form an atomic (iodine) or polymeric (nitrogen) solid. The second option is a pressure-driven association when atoms or small molecules developing new chemical bonds associate into larger clusters. To predict which of the two opposite tendencies will realize in experiment, in high-pressure physics frequently use so-called rule of thumb: elements under pressure often behave like heavier members of their group in the Mendeleev periodic table. Oxygen is the light-

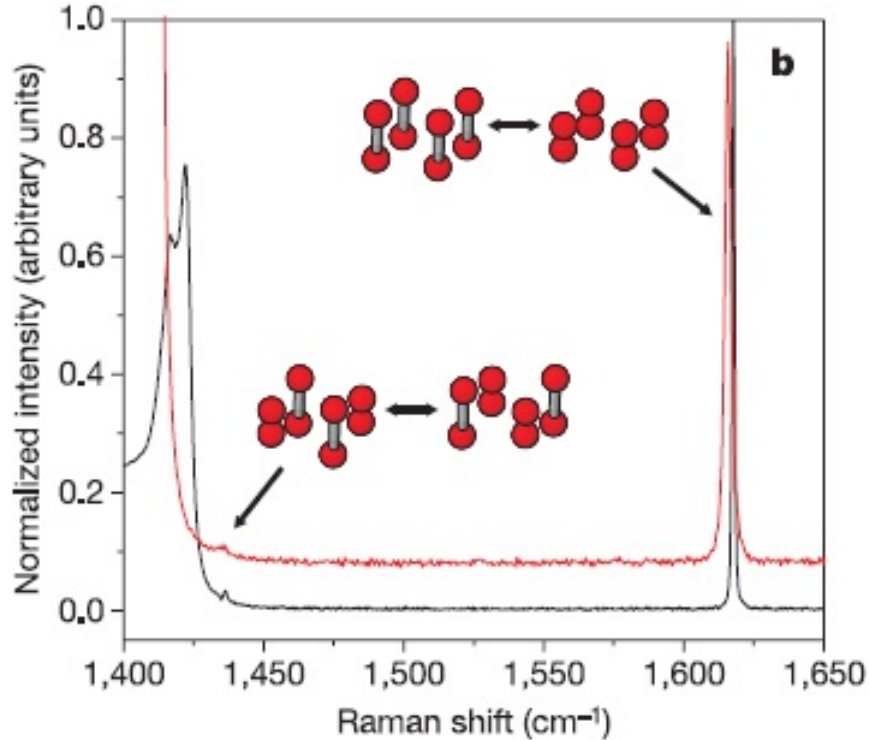


Fig. 10. (color online). Raman (red) and Fourier transform-Raman (black) spectra of  $\epsilon$ -oxygen. (From Ref. [17].)

est element in Group VI, with sulphur being the next heaviest family member. At room pressure and temperature, solid sulphur has the lattice of  $S_8$  molecules, with the atoms arranged in eight-membered rings. According to this rule of thumb one had to expect that oxygen under pressure will be associating into eight-membered rings, as sulphur does. However, the  $\epsilon$ -oxygen structures [17,18] show that a simple analogy with  $S_8$  molecules is misleading; the  $O_2$  molecules are arranged in  $(O_2)_4$  rhombohedra which looks like a flattened cube. While preserving their original diatomic character oxygen molecules associate under pressure into clusters of four pairs.

To have a consistent picture, the x-ray results of structural studies [17,18] should be in agreement with data of Raman and IR spectroscopy. There is a large body of spectroscopic information referred to the  $\epsilon$  phase [61–66], (see also Ref. [7] Secs. 5.3, 5.4). To integrate all the spectroscopic results (pressure induced very large intensity of IR active modes, number of Raman and IR active modes and their pressure and temperature dependence) the model for the  $\epsilon$  phase consisting out of  $O_4$  units has been proposed [65]. The normal modes of the  $O_4$  molecule with the  $D_{2h}$  symmetry (symmetric  $A_g$  and antisym-

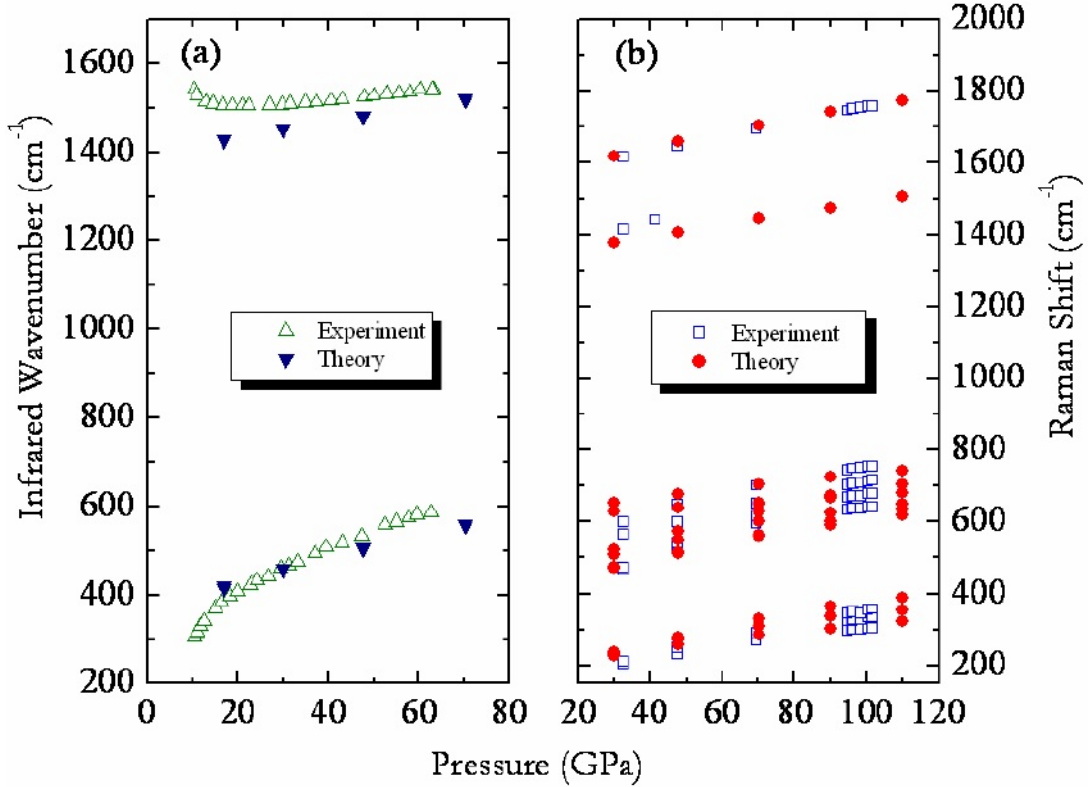


Fig. 11. (color online). Raman and IR spectra of  $\epsilon$  oxygen. (From Ref. [77].)

metric  $B_{3u}$  O-O stretching, in plane  $B_{1g}$  and out of plane  $A_g$  bending, symmetric and antisymmetric O<sub>2</sub>-O<sub>2</sub> stretching) and their optical activity are shown in Table 25 and Fig. 71 in Ref. [7]. After the discovery of the (O<sub>2</sub>)<sub>4</sub> structure of the  $\epsilon$  phase the spectroscopic model had to be revised [17]. An (O<sub>2</sub>)<sub>4</sub> unit of the  $D_{2h}$  symmetry has nine Raman and seven infrared modes. The vibrational modes were calculated for an isolated (O<sub>2</sub>)<sub>4</sub> unit without taking into account the crystal field effects. The comparison with the observed spectroscopic data at 17.6 GPa yielded three infrared modes ( $B_{3u}$  at 1500 cm<sup>-1</sup>,  $B_{2u}$  at 1443 cm<sup>-1</sup> and  $B_{1u}$  at 292 cm<sup>-1</sup>), in agreement with the reported infrared spectroscopic data [63,78]. There should be also four  $A_g$  Raman active modes, three of which, at 1600 cm<sup>-1</sup>, 342 cm<sup>-1</sup> and 161 cm<sup>-1</sup> have already been observed [67]. The fourth Raman mode, at approximately 1380 cm<sup>-1</sup>, corresponding to the antisymmetric stretching motion of the four O<sub>2</sub> molecules coupled in diagonal pairs, is a signature of the (O<sub>2</sub>)<sub>4</sub> unit. This mode was expected to be very weak and has not been observed supposedly because it lies very close to the Raman signal from the diamond anvils of the pressure cell. It was observed in the Raman scattering study performed on single-crystal samples with

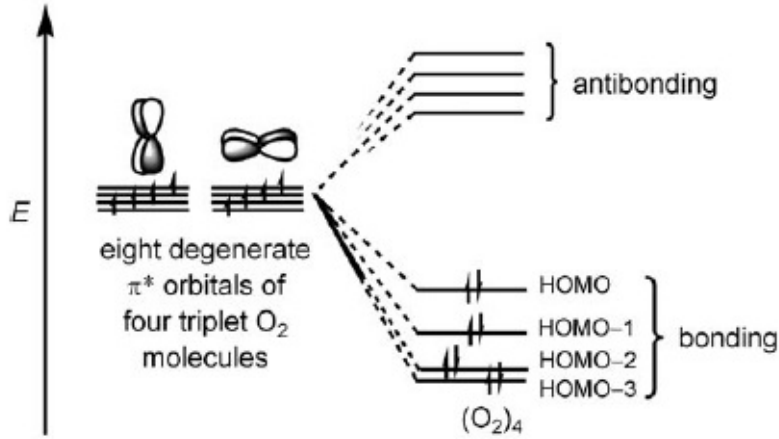


Fig. 12. Schematic energy diagram showing the interactions of eight degenerate  $\pi^*$  orbitals of four  $O_2$  molecules to form the bonding and antibonding molecular orbitals of the rhomboid  $(O_2)_4$  species. (From Ref. [32].)

high-quality optical surfaces. A weak Raman-active line was observed to emerge from the Raman signal from the diamond anvils at pressures above 30 GPa [17]. At 33 GPa, the new Raman line was observed at  $1,430\text{ cm}^{-1}$  (Fig. 10) and was interpreted to be the fourth Raman active mode of the  $(O_2)_4$  molecular unit. A comparison of experimental and calculated IR and Raman vibrational frequencies over the entire stability range of the  $\epsilon$  phase from Ref. [77] are shown in Fig. 11.

While  $O_8$  molecular units have not previously been observed or even anticipated in any oxygen phase, the  $O_2$ - $O_2$  gas-phase dimers of  $D_{2h}$  geometry with an equilibrium spacing of  $3.56\text{ \AA}$  are known in literature [79,80]. The same geometry was observed in the case of the  $O_2$ - $O_2$  dimers existing as impurities in solid Ne matrix [81]. Pauling [82] proposed that the formation of such a dimer requires that the chemical spin-spin contribution should be essential. The concept of  $\pi^*$ - $\pi^*$  bonding between the open-shell  $O_2$  molecules explains the formation of closed-shell  $O_8$ . *Ab initio* quantum chemical calculations of the exchange interaction due to the overlap of the open shell  $\pi^*$  orbitals were performed in Ref. [83]. The  $\pi^*$ - $\pi^*$  interaction is a two-electron stabilizing interaction involving the two open-shell  $\pi^*$  orbitals of the  $O_2$  molecule. In the case of  $(O_2)_4$  four sets of  $\pi^*$ - $\pi^*$  interactions involving eight degenerate singly occupied  $\pi^*$  orbitals of four  $O_2$  molecules will lead to eight molecular orbitals, four bonding and four antibonding. The eight electrons occupy the four bonding orbitals, resulting in an overall spin-paired molecule (Fig. 12). The quantum chemical

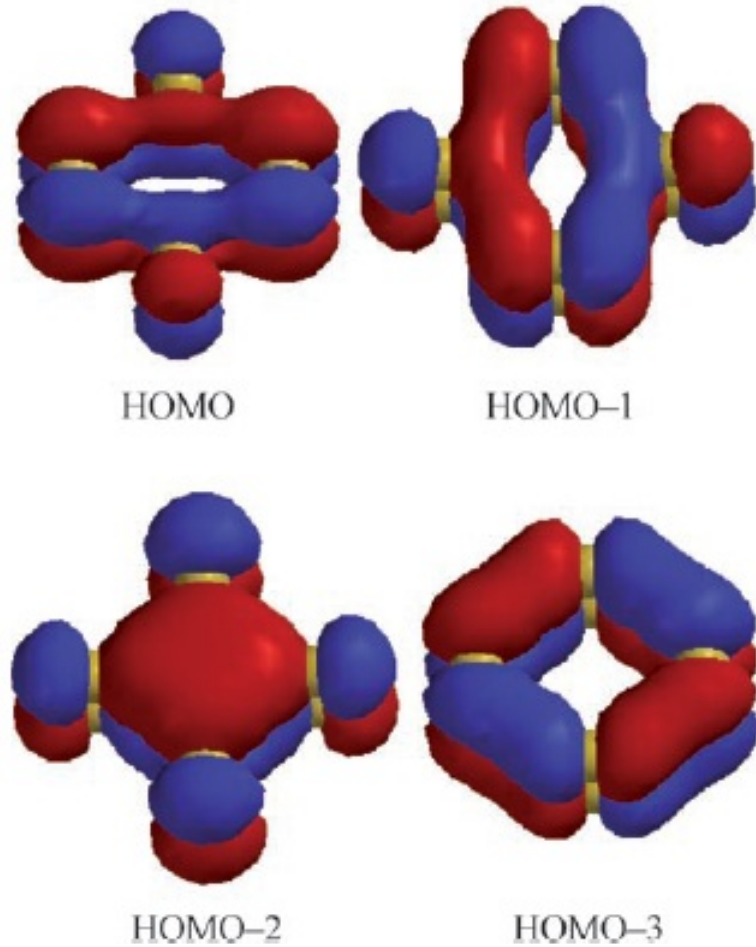


Fig. 13. (color online). Four highest occupied molecular orbitals of the rhomboid  $(\text{O}_2)_4$  molecule. (From Ref. [32].)

calculations confirmed that the ground state of rhomboid  $(\text{O}_2)_4$  is a singlet [32]. The crucial role of  $\pi^*-\pi^*$  interactions in rhomboid  $(\text{O}_2)_4$  is reflected in the shapes of the four highest occupied molecular orbitals shown in Fig. 13. Due to the bonding between open shell  $\pi^*$  orbitals both the gas-phase dimer  $(\text{O}_2)_2$  and  $(\text{O}_2)_4$  are chemically weakly bonded units. Indeed, while in the case of the strong intramolecular O-O bond the bond length within each  $\text{O}_2$  molecule is practically unaltered by pressure, the inter- $\text{O}_2$  distances both within, and between, the  $(\text{O}_2)_4$  units compress at the same rate of 0.011–0.014  $\text{\AA}/\text{GPa}$  (Fig. 9) emphasizing the weakness of the interaction between the  $\text{O}_2$  molecules that form the  $(\text{O}_2)_4$  units. The increase of the intensity of the infrared modes in the  $\epsilon$  phase in the range up to 30 GPa shows that there is a progressive strengthening of the inter- $\text{O}_2$  bonds over this pressure range [62,61].

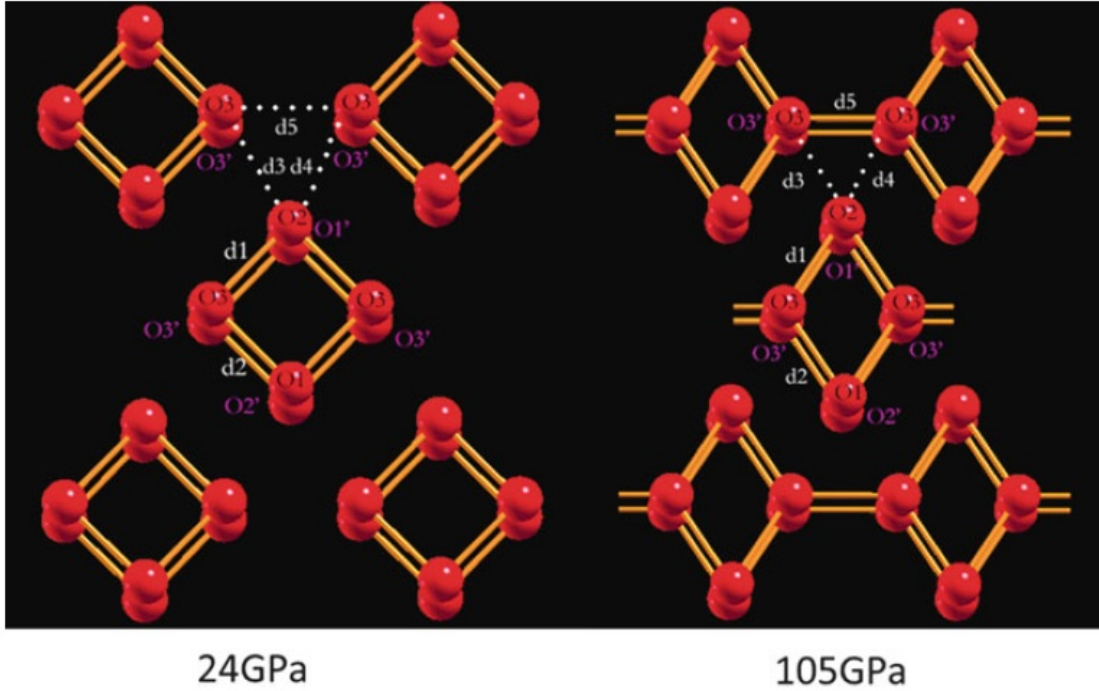


Fig. 14. (color online). Structure of  $(\text{O}_2)_4$  units in solid  $\epsilon$ - $\text{O}_2$  at 24 GPa and in the overpressurized  $\epsilon$  phase at 105 GPa. (From Ref. [85].)

In a free  $\text{O}_2$ - $\text{O}_2$  cluster the two-electron covalent bond originates from the pairing of two electrons each from the  $\pi^*$  orbital of the participating  $\text{O}_2$  molecules [32]. The fact that a much longer intermolecular distance was observed in  $\epsilon$  oxygen suggests that the nature of chemical bonding in the solid oxygen is different from that in the isolated cluster [36]. Important features of the nature of chemical bonding in the  $(\text{O}_2)_4$  clusters in  $\epsilon$  oxygen in comparison with the isolated  $(\text{O}_2)_4$  were revealed in the analysis performed in Ref. [36] through a topological analysis of charge density using the Bader's atoms-in-molecules (AIM) method [84]. The basic idea AIM analysis is to extract bonding information from the electron density.

Results of this analysis [36] indicate that the  $\text{O}_2$  molecules forming the rhomb-shaped clusters in the  $\epsilon$  phase are stabilized via donor-acceptor resonance structures, i.e. the donation of a paired  $\pi^*$  electron from one  $\text{O}_2$  into the empty  $\pi^*$  orbital of the other. In this interpretation, the  $\text{O}_2$  converted from a spin-uncoupled state of a free molecule into a spin-paired state (two electrons occupying one of the  $\pi^*$  orbital) to facilitate interactions with the neighboring  $\text{O}_2$  forming the cluster. Thus, this can be described as a true spin-coupled two-electron covalent bond. This description is consistent with the fact that the magnetic moment

of solid  $\text{O}_2$  has already decreased from  $2 \mu_B$  at the zero pressure structure to less than  $0.5 \mu_B$   $\delta$  phase preceding the  $\delta - \epsilon$  transition [21]. Therefore, interactions between  $\text{O}_2$  in the cluster cannot be due to simple spin pairing of electrons from the isolated molecules.

The shape of the  $(\text{O}_2)_4$  cluster is found to distort from a square prism to a diamond shape prism with increasing pressure. The OOO bond angle decreases gradually from  $88^\circ$  at 20 GPa to  $80^\circ$  near the  $\epsilon - \zeta$  transition at 97 GPa [17,18]. The distortion leads to changes in the structure and the electron density topology.

Considering the spin multiplicity is unavoidable when studying the properties of  $(\text{O}_2)_4$  molecule making this problem highly nontrivial since the DFT methods do not take into account the multiconfigurational character of the molecular oxygen clusters. In order to study properties of the  $(\text{O}_2)_4$  molecule under pressure and obtain a reliable characterization of the singlet state Bartolomei et. al. [41] performed high level multiconfigurational *ab initio* calculations. The singlet state, as a ground state for the  $\epsilon$  phase, first suggested by Gomonay and Loktev in Ref [31], is also the ground state of an isolated  $(\text{O}_2)_4$  molecule and thus it is also consistent with the magnetic collapse taking place at the  $\delta$ - $\epsilon$  transition.

The calculated interaction energy of the  $(\text{O}_2)_4$  molecule as a function of the square side  $d$  for the maximum spin multiplicity (nonet) and the singlet states are shown in Fig. 15. This figure shows that the interaction potential is a van der Waals-like potential with equilibrium square side next to  $3.0 \text{ \AA}$  in the gas phase. As can be seen from this figure the potential well of the singlet state is deeper and shifted to lower distances when compare with the one of the nonet state. This implies that in this system, like in the dimer ([41]), the exchange interaction favors the states with low spin multiplicity. It can be also seen that, while for the nonet state the pairwise approximation is in good agreement with the supermolecular calculation for the singlet state this is only true for large values of the square side  $d$ , while for small distances a softening of the repulsive wall is found showing the importance of many body effects and the exchange correlation energies in this range of interaction distances ( $d < 3\text{\AA}$ ).

Using the obtained interaction potential inside the molecule Bartolomei *et. al.* [41] developed a simple method to simulate the epsilon phase. They considered that all clusters are represented by a collections of cuboids and that they increase/decrease their size  $a$  at the same time. At a given pressure the center of mass of the clusters are fixed and determined by the experimental lattice parameters. Within this model the cell energy can be obtained as:

$$E(a) = V^{intra}(d) + \frac{1}{2} \sum_{i,j} V_{ij}^{inter}(r_{ij}) \quad (1)$$

where  $V^{intra}$  is the supermolecular  $(O_2)_4$  singlet potential and  $V_{ij}^{inter}$  is a spin average pair potential between the molecules  $i$  and  $j$  belonging

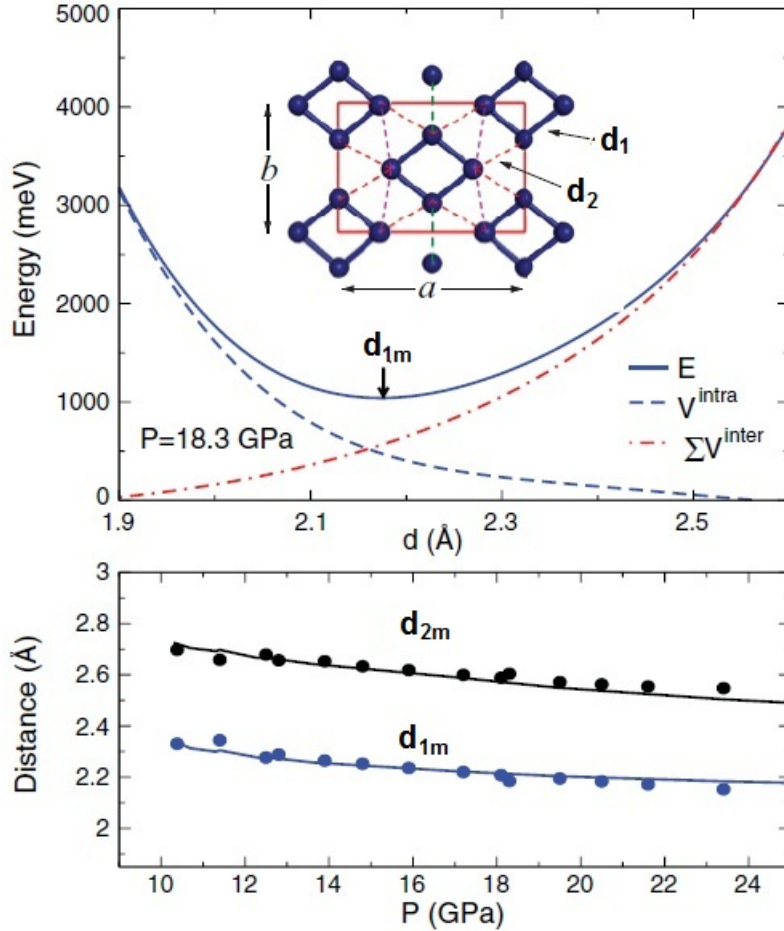


Fig. 15. (color online). Upper panel: energy of a layer of  $\epsilon$ -O<sub>2</sub> as a function of the cluster size for a pressure of 18.3 GPa (solid line). In the inset, the model unit cell is shown. A minimum of the energy is obtained for the intracluster distance  $d_{1m}$ . Lower panel: Pressure dependence of  $d_{1m}$  and  $d_{2m}$  (lines) compared with data of Ref. [18] (circles). (From Ref. [41].)

to different clusters. Using this model the values of the inter ( $d_{1m}$ ) and intramolecular ( $d_{2m}$ ) distances that minimizes the cell energy can be obtained and compared with the experimental values. Figure 15 shows the results obtained for  $d_{1m}$  and  $d_{2m}$  using this model and compared with experimental values taken from Ref. [18]. As can be seen the pressure dependence of this two calculated quantities are in good agreement with the observations. Despite the simplicity of this model it validates the supermolecular  $(\text{O}_2)_4$  singlet potential as a good approximation for this system and that the softening observed on the repulsion wall is realistic. It shows also that the most important many body effects take place inside the  $(\text{O}_2)_4$  molecule.

## 4 $\zeta$ phase

### 4.1 $\epsilon - \zeta$ (insulator-metal) phase transition

The insulator-metal transition has been first found in the absorption edge and reflectivity measurements [69,70], and confirmed in optical studies (see Ref. [7] Sec. 5.3 and references therein), x-ray diffraction [60,71], Raman [67,71], IR absorption [61], and resistivity [86,50] measurements. Results of these studies have been reviewed in Ref. [7]. In short, they are as follows.

By using a high brilliance synchrotron radiation source Akahama *et al.* [60] in the angle-dispersive powder x-ray studies up to 116 GPa found the structural phase transition to a new high-pressure  $\zeta$  phase. It was observed visually that after the transition at 96 GPa the oxygen sample became as shiny as the metal gasket [60]. The same behavior has also been found by Desgreniers *et al.* [69]. They have reported that at pressures about 95 GPa an increase in the Drude-like near-infrared reflectivity is observed. It was attributed to the onset of creation of nearly free electrons by a pressure-induced band overlap. A subsequent single-crystal x-ray diffraction study [71] indicated that from 96 GPa to 106 GPa a continuous displacive phase transition takes place to a new structure. Raman spectroscopy studies confirmed the structural change and the molecular nature of the  $\zeta$  phase [87], the vibron being the signature of the intramolecular bond. The volume reduction at

the  $\epsilon - \zeta$  phase transition is smaller than  $0.1 \text{ cm}^3/\text{mol}$  or  $\Delta V/V < 1.4\%$  [60]. Such value is too small compared with that expected in the molecular dissociation. The experimental evidence that the molecular dissociation does not take place up to at least 120 GPa was obtained by Weck *et al.* [71] and Goncharov *et al.* [87] in Raman studies.

In measurements of the electrical resistance of solid oxygen Shimizu *et al.* [86] observed a rapid decrease in the resistance with increasing pressure. The estimated resistivity at the highest applied pressure of 95 GPa was typical for semiconductors at room temperatures. This result was a direct evidence for the appearance of a conductive state of solid oxygen under pressure. The observation of a change in the slope of the resistance-temperature curve [86] (Fig.139 [7]) together with metallic character of reflectivity [69] evidences that at pressures exceeding 95 GPa solid oxygen becomes metallic. In subsequent measurements the same group discovered [50] that at low temperatures of 0.6 K metallic oxygen becomes superconducting with critical magnetic field about 2000 G.

#### 4.2 Raman and single-crystal x-ray studies of the $\zeta$ phase

The molecular excitations of  $\epsilon$  oxygen have been studied previously by Raman and IR spectroscopy [61,67]. The problem was that the intensity of the vibron excitations strongly decreased under pressure when approaching the  $\epsilon - \zeta$  transition and could not be followed in the metallic phase above 96 GPa. The vibron width increases linearly with pressure and reaches  $10 \text{ cm}^{-1}$  at 96 GPa. Above 96 GPa, due to the inhomogeneous broadening the vibron width increases dramatically merging the vibron into the background above 100 GPa. At 110 GPa, when the new structure is stabilized, the vibron mode reappears but with a negative frequency jump of  $60 \text{ cm}^{-1}$ . Goncharov *et al.* [87] published results of the detailed room-temperature Raman measurements of solid oxygen through the  $\epsilon - \zeta$  transition and in  $\zeta$  phase up to 134 GPa (Figs. 137, 138 in Ref. [7]). The obtained data showed unambiguously that the  $\zeta$  phase is molecular.

Understanding of the mechanism of the  $\epsilon - \zeta$  phase transition and the nature of the evolution of the  $\zeta$  phase with pressure became pos-

sible only after elucidation of the structure of  $\epsilon$  phase in the single-crystal [17] and powder diffraction [18] studies. By using the same x-ray single-crystal diffraction method that was used to solve the structure of the  $\epsilon$  phase Weck et al. performed angle dispersive x-ray diffraction measurements (ADX) [13] of single-crystal samples of solid oxygen. The samples were embedded in helium which was used as a quasi-hydrostatic pressure transmitting medium. The evolution of the diffraction peaks was consistent with previously found in the single-crystal energy dispersive x-ray diffraction (EDXD) experiment [71]. The displacive nature of the transition manifests itself by the "sliding" of diffraction peaks during the transition. The structural transition to the  $\zeta$  phase is completed above 106 GPa.

An earlier work of Serra et al. proposed the  $C2/m$  structure with four molecules per unit cell [88]. More recently, two competitive lowest enthalpy structures were proposed from calculations [30]: one of space group  $C2/c$ , containing four  $O_2$  molecules per unit cell, arranged in a chainlike herringbone structure, and a second one, suggested as being the best candidate, isosymmetric to the  $\epsilon$  phase, with chainlike connections between the  $O_8$  units. However, the underestimation of the band gap in DFT calculations has made it difficult to resolve the link between metallization and structural changes. Two recent GW calculations, meant to improve the calculation of the band gap, have indicated that the insulator-metal transition occurs along with the structural transformation [35,36]. In all calculations, however, an unusually large disagreement between the calculated and the measured transition pressures remains.

Analysis of diffraction intensities of the reflexes observed after the phase transition to the zeta phase was completed did not allow to make an unambiguous choice between monoclinic unit cells of space groups  $C2/m$  or  $C2/c$ , two possible candidates for the  $\zeta$  phase space group. Though analyzing the  $d$ -spacings data Weck et al. [13] decided in favor of  $C2/m$ , the most solid evidences for the choice of the space group and unit cell assignment were obtained from the Raman spectroscopy measurements. There are four molecules in the  $C2/m$  primitive cells of  $\zeta$ - $O_2$ , and  $\epsilon$ - $O_8$ , so we have 12 Raman active ( $7A_g + 5B_g$ ) nine of which have been observed in the Raman measurements [87,13] (Fig. 16). Since the  $C2/c$  unit cell has only six Raman active modes ( $3A_g$

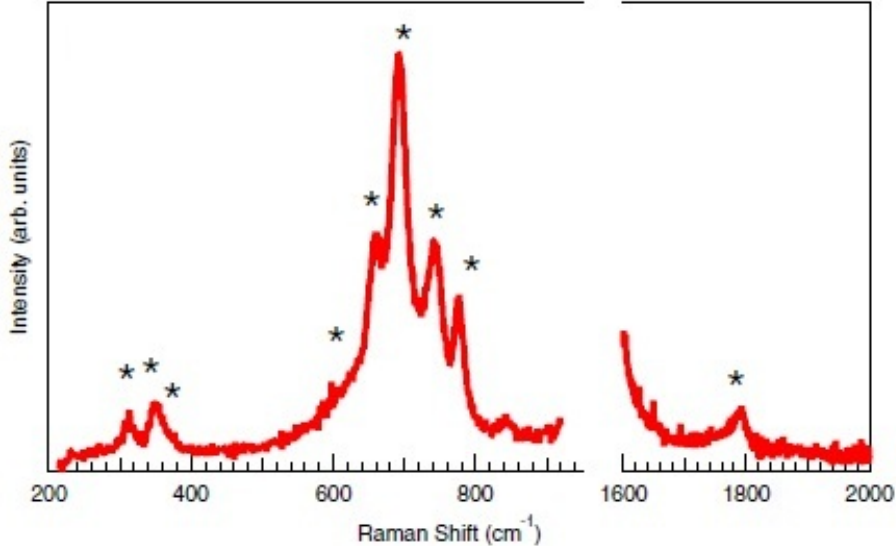


Fig. 16. (color online). Raman spectrum of crystal of solid oxygen in helium at 118 GPa at 300 K. The stars indicate the positions of the observed Raman active bands. (From Ref. [13].)

+  $3B_g$ ), that is less than it was observed experimentally, the spectroscopic results unambiguously excluded the  $C2/c$  unit cell from the consideration. The pressure dependencies of the Raman-active modes calculated by Ma et al. [30] in comparison with the experimental data obtained by Goncharov et al. [87] are shown in Fig. 17. As can be seen, the most significant frequency changes at the  $\epsilon - \zeta$  phase transition affect the three experimentally observed low-lying modes in the  $\epsilon$  phase in the  $200 - 500 \text{ cm}^{-1}$  range, which transformed with abrupt frequency changes into two modes ( $\nu_a$  and  $\nu_b$ ) in  $\zeta\text{-O}_2$ . It is from the significant frequency changes, that Goncharov et al. [87] concluded that this phase transition is unlikely to be isostructural. However, in theory developed by Ma et al. [30] it was shown that the observed behavior of the spectrum is rather accurate assuming the isostructural phase transition picture (Fig. 17). In particular, the three modes in  $\epsilon\text{-O}_8$  are transformed upon formation of  $\zeta - C2/m$  into a downshifted mode  $A_g$  and two almost degenerated upshifted modes ( $A_g$  and  $B_g$ ) which are related to the intermolecular vibration along the shortened  $b$  axis. In the theory they lay very close to each other precluding an easy observation of two separate Raman-active modes. The downshifted  $A_g$  mode was attributed to the intermolecular vibration of the  $(\text{O}_2)_4$  clusters. A small negative drop in the vibron frequency less than  $\sim 1\%$  observed at the  $\epsilon - \zeta$  transition [87] is also consistent with the theory by Ma *et al* where it was attributed to the slight increase of the in-

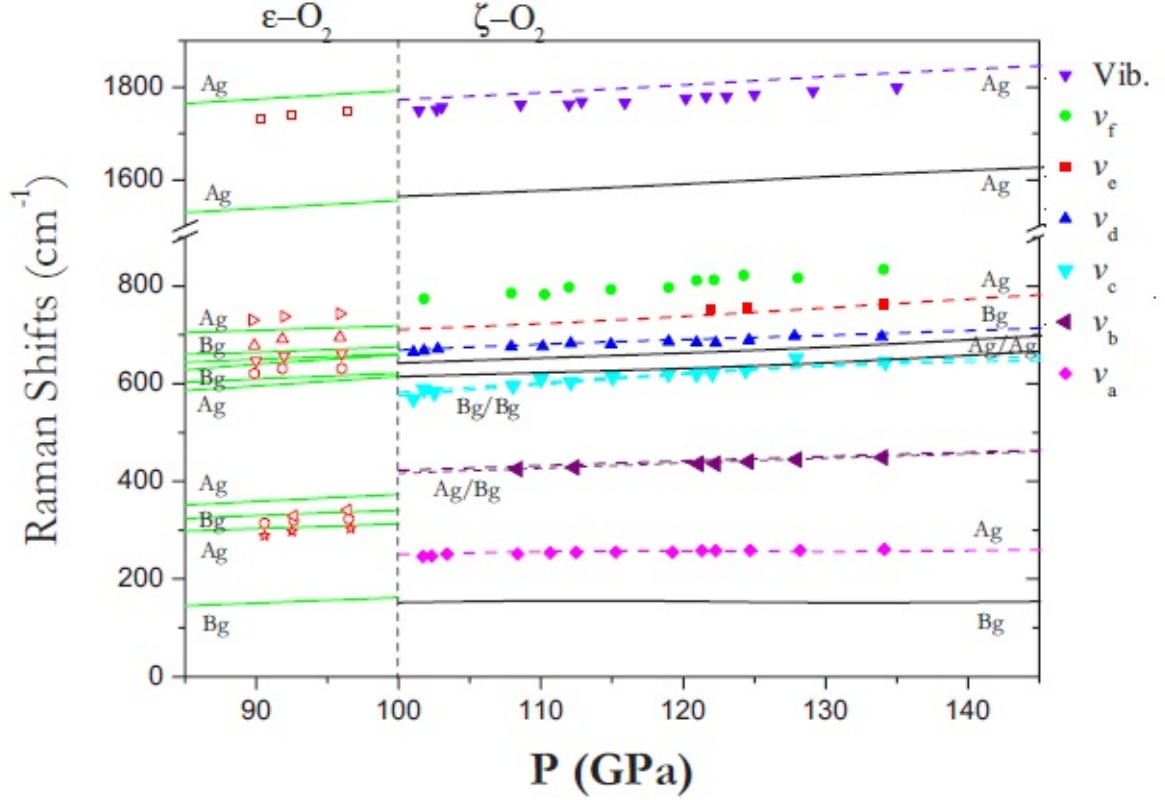


Fig. 17. (color online). Calculated Raman frequencies *vs.* experimental data from Ref. [87]. (From Ref. [30].)

tramolecular bond length from  $1.197 \text{ \AA}$  in  $\epsilon\text{-O}_8$  to  $1.199 \text{ \AA}$  in  $\zeta\text{-}C2/m$  at 100 GPa.

The pressure dependence of the lattice parameters obtained both in the ADXD [13] and EDXD [71] single-crystal measurements is shown in Fig. 18. The onset of a first-order phase transition is clearly seen from the abrupt change of lattice parameters taking place at  $\approx 100$  GPa, at a slightly higher pressure than the metallic transition. A large contraction of about 10% is observed in the **b** direction with the *a* lattice parameter showing an increase of about 6% and a small contraction of about 3% in the **c** direction. Thus, the  $\epsilon - \zeta$  transition is essentially an "intraplane" transformation.

The x-ray diffraction data [13] demonstrate that this transition proceeds gradually with pressure between 96 GPa and 106 GPa. After the phase transition, the  $\text{O}_8$  units turn out to be connected along the **b** direction, so that the intra- $\text{O}_8$  distance and inter- $\text{O}_8$  distance become equal, which means the dissociation of two  $\text{O}_8$  units in the unit cell

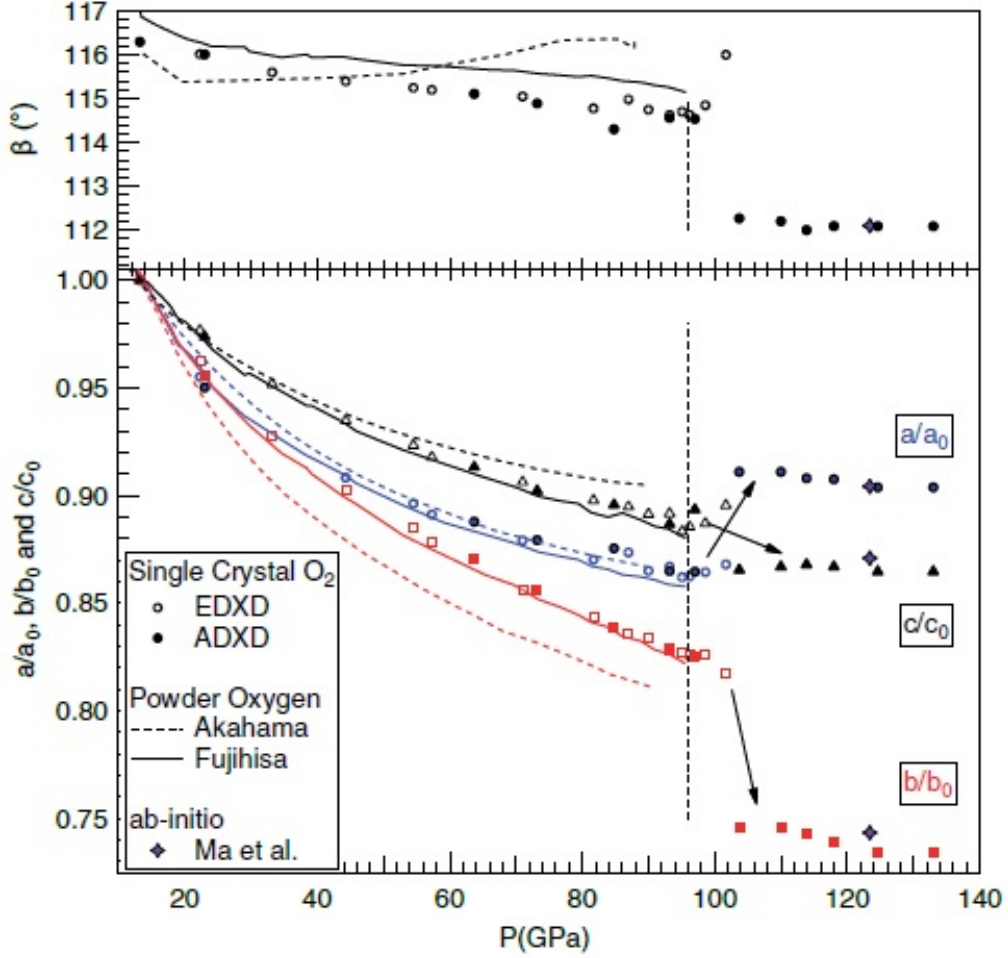


Fig. 18. (color online). Pressure dependence of the lattice constants  $a$  (blue),  $b$  (red),  $c$  (black) and angle  $\beta$  of the  $C2/m$  monoclinic cell:  $a_0 = 7.970\text{\AA}$ ,  $b_0 = 5.633\text{\AA}$ ,  $c_0 = 3.711\text{\AA}$  and  $\beta = 116.3^\circ$  at 13.2 GPa [17]. Open symbols: Ref. [71]. Full symbols: Ref. [13]. Dashed line: Ref. [60]. Full Line: Ref. [18]. The vertical dashed line indicates the metallic transition pressure. (From Refs. [13,89].)

into eight  $\text{O}_2$  molecules. At 96 GPa, the closure of the indirect band gap in the  $\epsilon$  phase induces a small displacive transition along the  $\mathbf{b}$  direction, which is completed at 106 GPa and is accompanied by a transition to the new molecular arrangement in the  $ab$  plane.

The equations of state of solid oxygen in the  $\epsilon$  and  $\zeta$  phases are shown in Fig. 19. The EDXD [71] and EDXD [13] experimental data are compared to the results of two DFT calculations [30,35].

The structure shown in Fig. 20 (upper left) exhibits isolated  $(\text{O}_2)_4$  clusters in the  $\epsilon$  phase. In this structure, there are three symmetry sites for oxygen atoms labeled as O1, O2, and O3 [17,18] in Fig. 20 (upper Figures). The three distances ( $d_1$ ,  $d_2$ , and  $d_3$ ) in Fig. 20 (upper

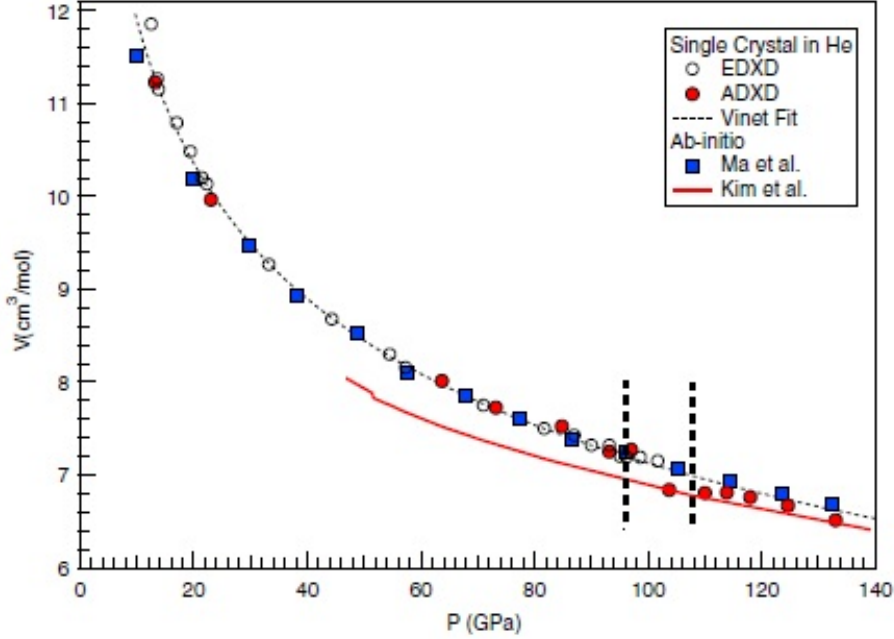


Fig. 19. (color online). Equations of state of solid oxygen, in the  $\epsilon$  and  $\zeta$  phases with a comparison between experiment (ADXN data from Ref. [13], EDXD data from Ref. [71]) and calculations of Ma et al. [30] and Kim et al. [35]. The vertical dashed lines indicate the pressure range of the displacive transition. (From Ref. [13].)

left) represent the characteristics of inter- and intradistances of the refined structure. For the  $\epsilon$  phase,  $d_1$  is significantly shorter than  $d_2$  and  $d_3$ , as shown in Fig. 20 (bottom). When  $\epsilon$ -oxygen is compressed, the intra-cluster and inter-cluster distances  $d_1$  and  $d_3$  decrease rapidly (Fig. 20 (bottom)) and at the transition pressure after the upward jump of  $d_1$  and downward jump of  $d_3$  they became equal. This results in the change of bonding in the  $ab$  plane. The enhanced bonding along  $d_3$  makes  $(\text{O}_2)_4$  clusters connected to each other, as shown in Fig. 20 (upper left). After overcoming  $d_1$ ,  $d_3$  goes almost parallel with  $d_1$  and makes chainlike connection along the  $b$  axis. As a result, the localized electrons in oxygen clusters spread out into the  $ab$  plane making the metallic  $\zeta$  phase [17,18,36].

From theoretical side [35], to look at the metallization of solid oxygen and to get well defined excited state properties one has to go beyond a standard DFT. For this, the so-called GW approximation to the self-energy  $\Sigma$  have been chosen. As suggests this study, there is no post-  $\zeta$  phase up to 250 GPa. It is noted that the predicted structures at 250 GPa are still molecular: e.g., for the  $\zeta - C2/m$  structure, the intramolecular O-O distance is 1.171 Å, much shorter than the shortest

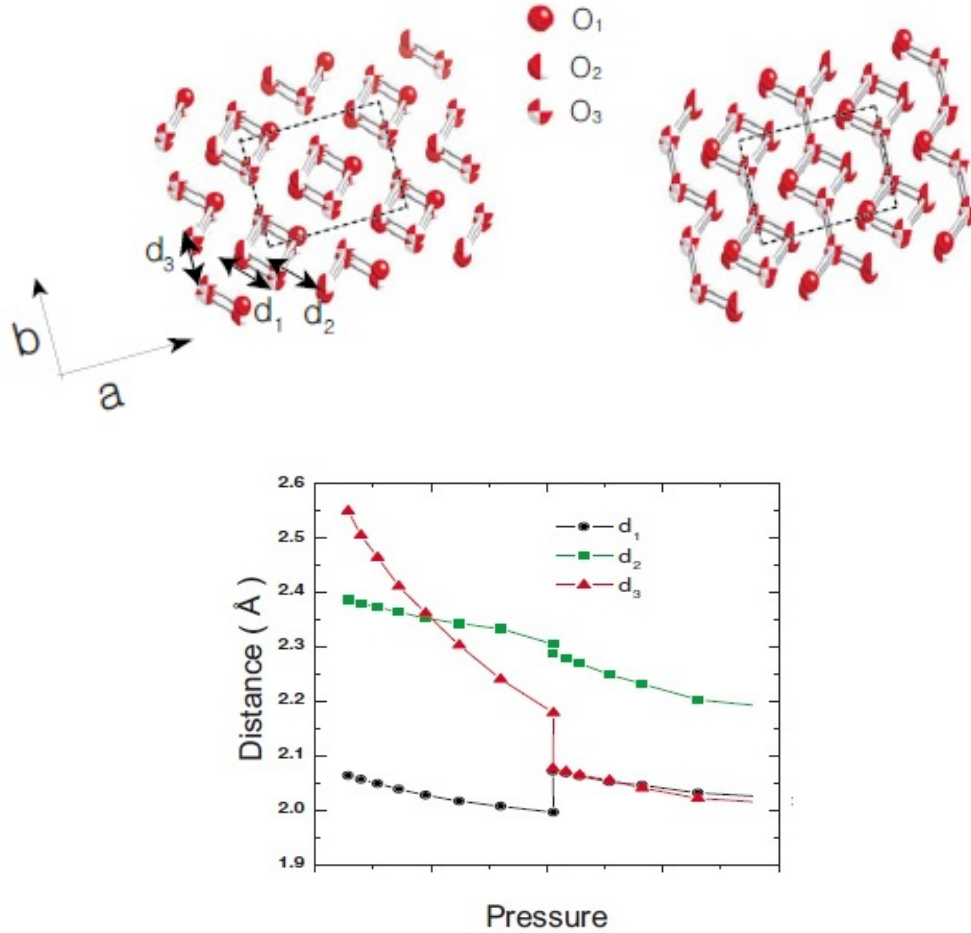


Fig. 20. (color online). The structure of  $\epsilon$  (upper left) and  $\zeta$  (upper right) phases as viewed perpendicular to the  $ab$  plane; the intra- and intermolecular distances as a function of unscaled pressure. (Modified from Ref. [35].)

intermolecular distance of  $1.902 \text{ \AA}$ .

In conclusion of this Section, the single-crystal x-ray diffraction data [13] have demonstrated the isosymmetric nature of the  $\epsilon - \zeta$  phase transition in solid oxygen. The combination of first-principle calculations with the diffraction data gave a convincing view of the atomic displacements leading to the new structure. There is a certain similarity between the structural changes induced by metallization in solid  $I_2$  and solid  $O_2$  [13]. In both cases, metallization by the closure of the band gap causes an instability of the lattice that evolves, through a displacive phase transition, into the denser structure along with the dissociation of molecular entities,  $I_2$  and  $O_8$ , respectively. A further transformation of metallic  $O_2$  into an atomic metal is predicted at much higher pressure, namely, above 250 GPa [30,15].

### 4.3 Persistence of oxygen molecules up to terapascal pressures

In the simplest molecular solids like O<sub>2</sub> or N<sub>2</sub> at ambient pressures the intramolecular forces and associated intramolecular vibration frequencies ( $\sim 1000 \text{ cm}^{-1}$ ) exceed by an order of magnitude the intermolecular ones ( $\sim 100 \text{ cm}^{-1}$ ). The corresponding intranuclear distances in the molecules (1.2074 Å in O<sub>2</sub>, 1.0977 Å in N<sub>2</sub>) is much shorter than the nearest intermolecular distances (3.187 Å in O<sub>2</sub>, 3.994 Å in N<sub>2</sub>). As pressure increases the intermolecular spacing becomes comparable with the intramolecular bond length. From *a priori* consideration it is clear that in this situation the diatomic molecular solid may become unstable to the transition to an atomic solid state, i.e. toward pressure induced dissociation transition. The question to which pressures oxygen molecules can survive is of importance for solid-state physics, for geochemistry (the estimated pressure at the center of Earth is 380 GPa), for planetary science.

Although the O=O double bond in the O<sub>2</sub> molecule is not as strong (the dissociation energy  $D_0 = 5.1156 \text{ eV}$  [7]) as the N≡N triple bonds ( $D_0 = 9.76 \text{ eV}$  [90]), O<sub>2</sub> polymerizes at a pressure an order of magnitude higher than N<sub>2</sub> ( $\approx 110 \text{ GPa}$  [91,92]). Unfortunately, there is no a simple qualitative theory which would permit to connect the pressure dissociative transition with the solid-state parameters of the substance. The DFT calculations by Ma et al. [30] showed that oxygen molecules persist to at least 250 GPa. The subsequent calculations [15] increased this estimate to 1.9 TPa which was called by the authors "intriguing".

The enthalpy-pressure relations for the most interesting structures found by Sun et al. [15] are plotted in Fig. 21. In these calculations DFT computations (the Perdew-Burke-Ernzerhof (PBE) generalized gradient approximation (GGA) exchange-correlation density functional) were combined with searching methods for predicting low-enthalpy structures of oxygen in the multi-TPa range. Figure 21 shows that at about 1.9 TPa molecular oxygen transforms into a square-spiral-like structure belonging to space group  $I4_1/acd$ . Similar structures have been found in other heavier group VI elements, such as sulfur and selenium [93]. The shortest O-O bond length in  $I4_1/acd$

structure at 2 TPa is about  $1.15 \text{ \AA}$ , which is longer than that of the molecular phase at the same pressure (about  $1.03 \text{ \AA}$ ). The shortest O-O distance between the chains is about  $1.55 \text{ \AA}$ , and the distance between the axes of neighboring square spirals is half of the lattice vector. The O-O-O angle in the helix is about  $98.7^\circ$ .

The low-pressure molecular phases are very close in enthalpy (Fig. 21, inset). Among these phases,  $P6_3/mmc$ ,  $C2/m$ ,  $R\bar{3}m$  become stable in turn on increasing the pressure from 0.5 to 1.9 TPa. More precise methods than DFT might be required to clarify the structural sequence as the enthalpy differences are so small.

## 5 High-pressure high-temperature part of the phase diagram

### 5.1 Structure and properties of the $\eta$ phase

The high-pressure high-temperature studies of oxygen are of great importance for the development of condensed-matter theory, specifically understanding the structural and electronic properties of highly com-

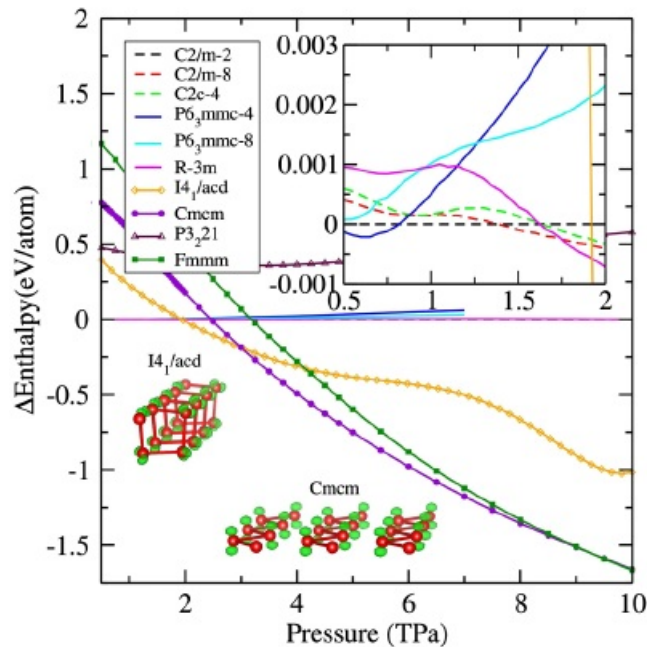


Fig. 21. (color online). Enthalpy-pressure relations for solid oxygen. The upper right inset shows the enthalpies of the molecular phases, while the insets in the lower left corner show the square-spiral structure of  $I4_1/acd$  and zigzag chains of  $Cmcm$ , respectively. (From Ref. [15].)

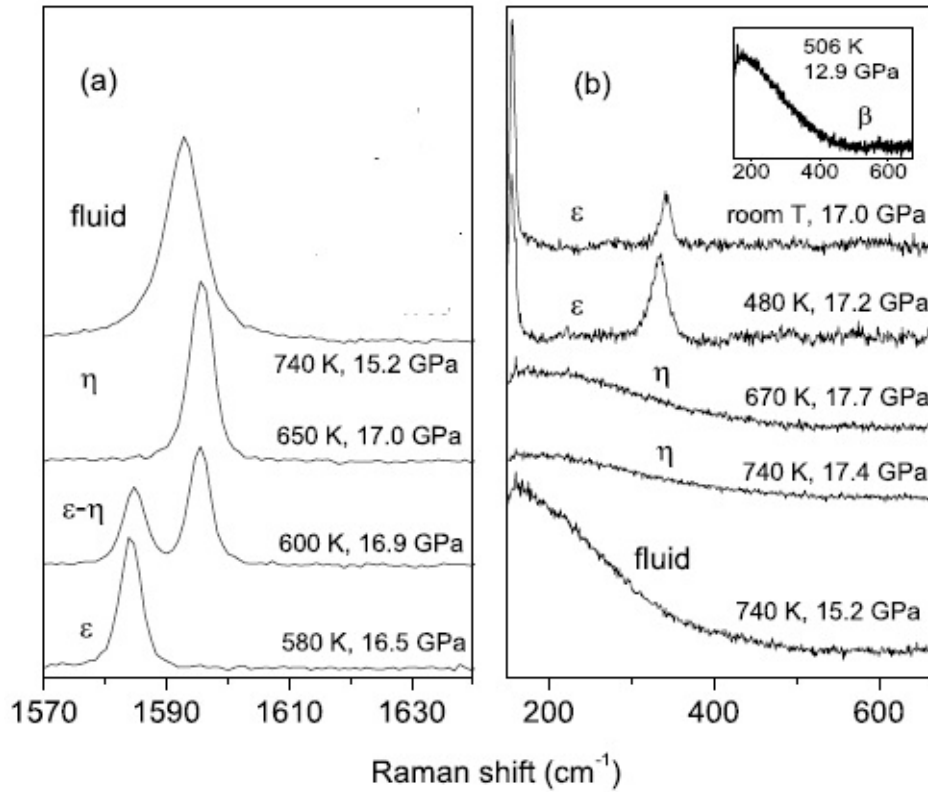


Fig. 22. Raman spectra of oxygen showing the transformation between  $\epsilon$ ,  $\eta$  and fluid phases: (a) vibrational modes; (b) lattice modes in the solid phases and density of states in fluid. (Modified from Ref. [12].)

pressed materials. The problems of structural stability, thermodynamics of oxygen, its chemical reactivity are of fundamental importance for geophysics as oxygen is the most abundant element in the Earth.

The first high-temperature diamond-anvil-cell Raman study of solid oxygen were performed as early as in 1982 year by Yagi, Hirsh, and Holzapfel who managed to measure the melting line and the  $\beta - \epsilon$  phase boundary up to 500 K (13 GPa) [94]. Yen and Nicol extended these measurements up to 20 GPa, 650 K [68]. Above 450 K, only visual observations were made, and on their basis the existence of the liquid- $\beta$ -  $\epsilon$  triple point was inferred. More recently, static  $P - T$  studies of oxygen using Raman techniques have been extended to 23 GPa and 1250 K [12]. This study reported the existence of a new molecular phase,  $\eta$ -O<sub>2</sub>, existing at high pressures and temperatures. Further studies using resistive [29] and laser heating [95] confirmed the existence of the high-temperature  $\eta$  phase.

Raman spectra of oxygen showing the transformation between the  $\epsilon$ ,  $\eta$  and fluid phases in the temperature range 580 - 740 K, and pressure

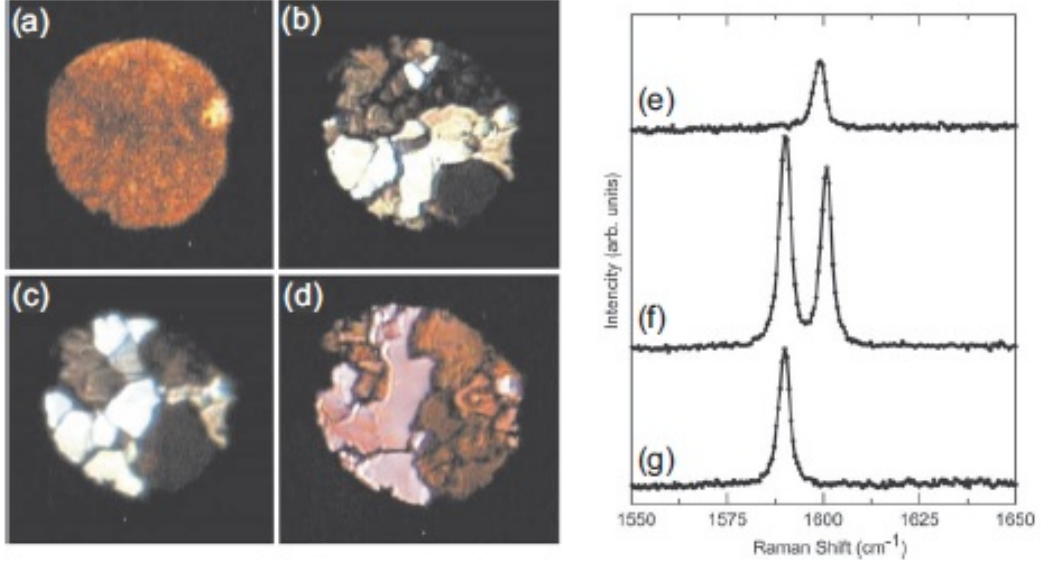


Fig. 23. (color online). Left: Microphotographs of the  $O_2$  sample at different  $P - T$  conditions (a-d): (a) Polycrystalline sample of  $\epsilon$ - $O_2$  at 18.1 GPa and 293 K. (b) Crystallites of  $\epsilon$ - and  $\eta$ - $O_2$  at 18.1 GPa and 675 K. (c) Crystallites of  $\eta$ - $O_2$  at 16.6 GPa and 650 K and (d) crystallites of  $\epsilon$ - $O_2$  after quenching to 16.1 GPa and 293 K. Right: Raman spectra of oxygen vibrons of the  $\epsilon$  and  $\eta$  phases (e-g): (e) a vibron from the  $\epsilon$  phase at the same  $P - T$  conditions as image (a), (f) the two vibrons from the mixed  $\epsilon$ - $\eta$  sample at the same  $P - T$  conditions as image (b); (g) a single vibron from the  $\eta$  phase at the same  $P - T$  conditions as image (c). (Modified from Ref. [19].)

range 15.2 - 17.0 GPa can be seen in Fig. 22 (a, b) [12]. The spectrum at 15.2 GPa was measured in the fluid phase Fig. 22 (a). At 580 K the peak of the  $\epsilon$  phase was observed. A new peak shifted to higher frequencies by about  $11 \text{ cm}^{-1}$  appears with increasing temperature; this peak is indicative of a phase transition and was ascribed depending on pressure either to  $\beta$  or to the  $\eta$ - $O_2$ . At 600 K the coexistence of  $\epsilon$  and  $\eta$  phases was observed, and the transition to the  $\eta$  phase is complete at 650 K. The correspondence between the photomicrographs of the samples in the  $P - T$  range of the  $\epsilon - \eta$  phase transition and their Raman spectra are shown in Fig. 23.

Spectral differences between the phases are also observed in the lattice modes [Fig. 22(b)]. At room temperature and 480 K the two intense peaks of the  $\epsilon$  phase are observed at about  $155$  and  $340 \text{ cm}^{-1}$ , respectively. In the  $\eta$  phase the spectrum is totally different: this frequency region is dominated by a very broad band with a shallow maximum around  $200 \text{ cm}^{-1}$ , which is indicative of a high degree of orientational disorder. A similar broad band is observed both in the

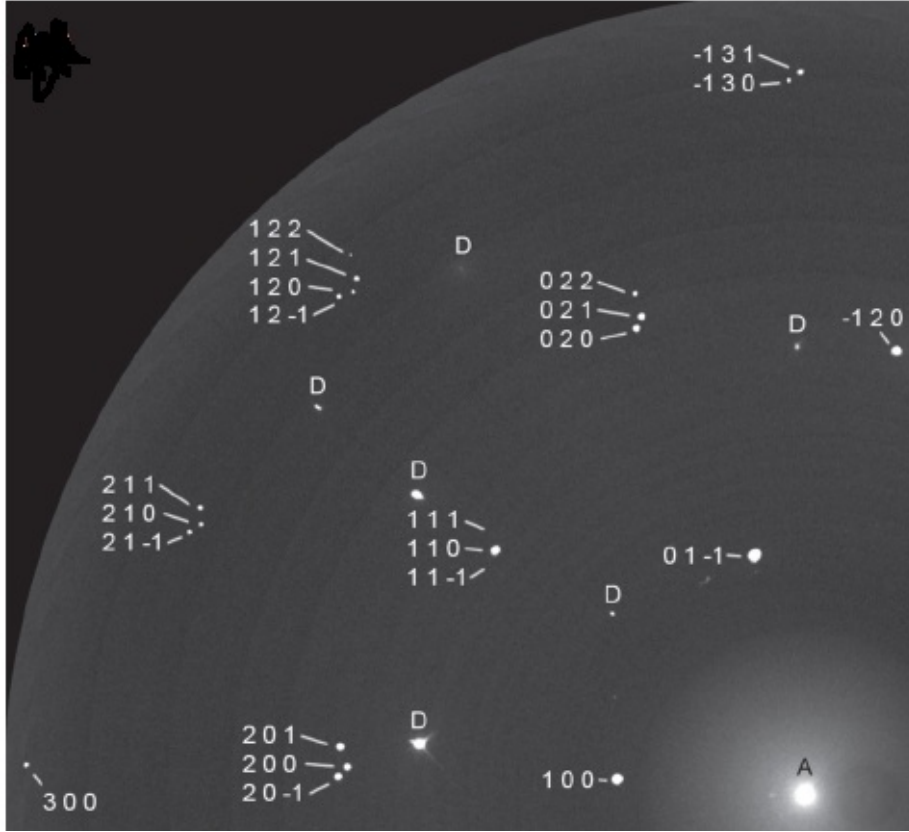


Fig. 24. Composite diffraction images showing representative data from the  $\eta$  phase. The reflections from the  $\eta$  phase are indexed on a hexagonal lattice and the absent  $(111)$  and  $(11\bar{1})$  reflections are consistent with the space group symmetry. Reflections from the diamond anvils are marked by the letter "D". "A" marks an artifact arising from the spiral readout of the image plate reader. (From Ref. [19].)

orientationally disordered fluid and orientationally ordered  $\beta$  phases [Fig. 22(b)(inset)].

Determination of the structure of the  $\eta$  phase was made possible through the use of the third generation synchrotron sources for single-crystal structural studies and the development of diamond seats with wide opening angles [96]. The oxygen samples were loaded cryogenically into diamond anvil cells equipped with rhenium gaskets. For the visual and Raman studies, a high-temperature piston-cylinder pressure cell was used with diamonds with  $300 \mu\text{m}$  culets, while for the diffraction studies a locally constructed membrane pressure cell equipped with large x-ray aperture ( $\pm 40^\circ$ ) diamond seats and diamonds with  $400 \mu\text{m}$  culets was used. The  $\eta$  phase data were collected over a  $20$  scan range at  $15.9 \text{ GPa}$  and  $625 \text{ K}$ . As a result, high quality single-crystal diffraction data were collected at high temperatures (Fig. 24) which made it possible to determine the structure of  $\eta$ -oxygen at  $15.9 \text{ GPa}$

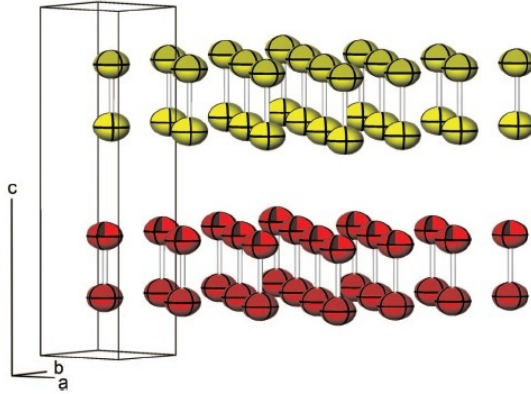


Fig. 25. (color online). The structure of  $\eta$  oxygen, showing the molecular layers that make up the structure. The two molecules within each unit cell are shown using different colors and are centered at  $(1/3, 2/3, 1/4)$  and  $(2/3, 1/3, 3/4)$ . The coloring of the molecules is the same as that used for the  $\eta$  phase in Fig. 26. (From Ref. [19].)

and 625 K. A total of 66 individual reflections were observable and analysis of the systematic absences showed them to be consistent with the centrosymmetric space group  $P6_3/mmc$ , in agreement with Ref. [97]. (It should be noted that the noncentrosymmetric space groups  $P6_2c$  and  $P6_3mc$  are also consistent with the x-ray data.)

In the determination of the  $\eta$  phase structure, in addition to the x-ray single-crystal data, some other structural data were used. In particular, the density data show that  $\eta$  oxygen has two  $O_2$  molecules per unit cell. Also, the obtained  $c/a$  ratio of 2.560(3) is very close to two-thirds of the  $c/a$  ratio of 3.833 in the  $\beta$  oxygen structure at 15.9 GPa at 293 K (as obtained by extrapolating the lower-pressure data of Uemura et al. [98], which comprises three layers of aligned  $O_2$  molecules). As a result, we have the structural model for  $\eta$  oxygen in which two  $O_2$  molecules within each unit cell aligned parallel to the  $c$ -axis are centered at  $(1/3, 2/3, 1/4)$  and  $(2/3, 1/3, 3/4)$  sites of space group  $P6_3/mmc$ . The resulting OO bond length of  $1.159(12)\text{\AA}$  is slightly shorter than the gas-phase value  $1.207\text{\AA}$  [7], in agreement with the values reported in previous x-ray diffraction studies of the  $\beta$  and  $\delta$  phases [75,76]. The resulting structure is shown in Fig. 25.

The structure of  $\eta$  oxygen is closely related to the other known high-pressure phases of oxygen, particularly the rhombohedral  $\beta$  phase [12]. Figure 26 shows the structures of the  $\alpha$ ,  $\beta$ ,  $\delta$ ,  $\epsilon$ , and  $\eta$  phases, each observed perpendicular to the sheets of  $O_2$  molecules that comprise all five structures, and thus parallel to the OO bonds. The  $\eta$  structure

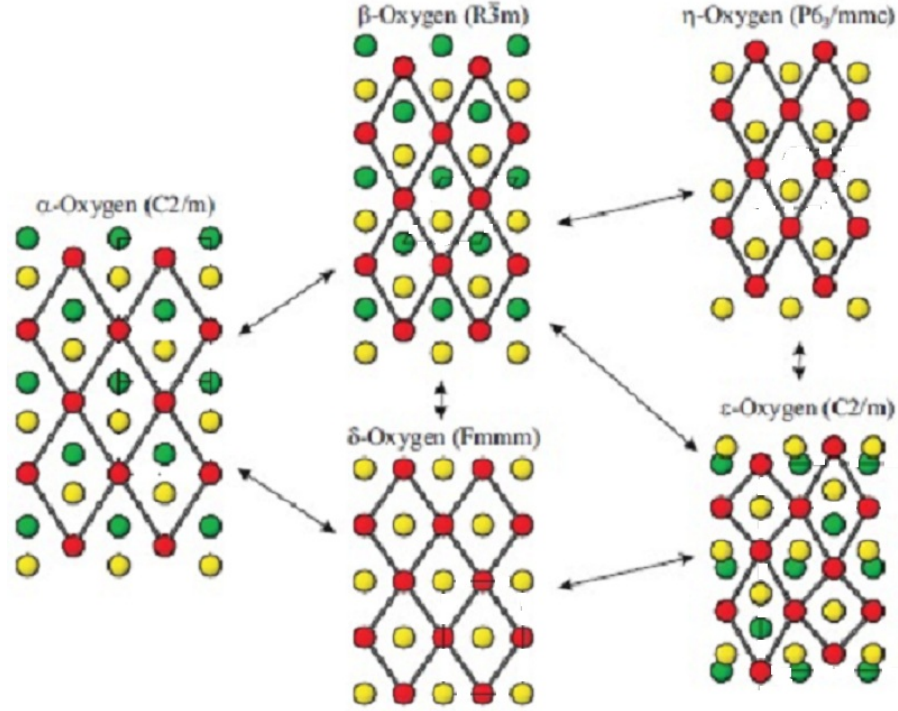


Fig. 26. (color online). Phase transitions between the various structures associated with a change in temperature or pressure. The structures of  $\alpha$ ,  $\beta$ ,  $\delta$ ,  $\eta$ , and  $\epsilon$  oxygen, as viewed perpendicular to the layers of parallel O<sub>2</sub> molecules. The O<sub>2</sub> molecules are thus seen along the OO bond. Different colors are used to identify molecules at different heights within each unit cell and arrows indicate which phases transform to which. (From Ref. [19].)

comprises two such layers of molecules, stacked alternately in an hcp-like *ABAB* stacking, while the  $\beta$  oxygen structure comprises three such layers in an fcc-like *ABCABC* stacking.

## 5.2 Phase transition to the $\eta'$ phase

Goncharov et al. performed single-crystal x-ray and Raman measurements in the range 44 - 90 GPa and found a new molecular phase of solid oxygen [14]. X-ray diffraction data are consistent with the *P6<sub>3</sub>/mmc* space group, that is the new phase was suggested to be isostructural with  $\eta$ -O<sub>2</sub> [19]. The authors called the newly observed phase as  $\eta'$  oxygen to distinguish it from the  $\eta$  phase identified near 18 GPa (Refs. [12,19]) but to stress that both phases are isostructural. The  $\eta'$  phase was found to be stable over a remarkably wide *P - T* range where  $\epsilon$ -O<sub>2</sub> was previously considered to be the stable form. The  $\epsilon - \eta'$  phase transition line found in the x-ray and Raman

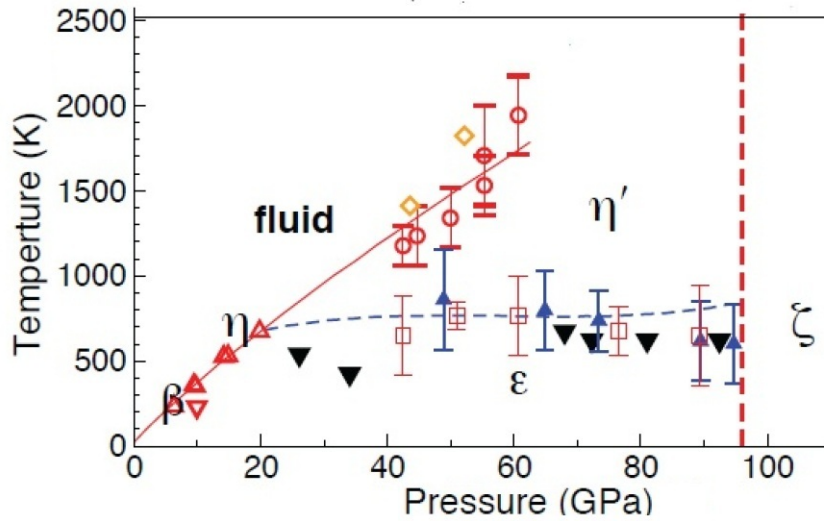


Fig. 27. (color online). High-pressure high-temperature  $P - T$  phase diagram of oxygen. Melting experimental points: open triangles up [29], open circles with the error bars [14], yellow diamonds [37]. The red solid line is the melting line calculated from the Simon equation proposed by Goncharov et al. in Ref. [14] (see Ch. 7). Open triangle down  $\epsilon - \beta$  transition. Black filled triangles down represent conditions where the  $\epsilon$ -O<sub>2</sub> is stable. Open squares and filled triangles up with error bars are  $\epsilon - \eta'$  transition determined by x-ray and Raman, respectively; the curved dashed line is the proposed  $\epsilon - \eta'$  transition [14]. The dashed vertical line shows where the metallization takes place. (Modified from [14].)

measurements turned out to be essentially pressure independent (Fig. 27).

In agreement with the x-ray data, low-frequency Raman peaks of  $\epsilon$  oxygen decrease in intensity abruptly near 1000 K, and a broad band near  $470 \text{ cm}^{-1}$  appears upon further heating (Fig. 28). The Raman vibron at  $1680 \text{ cm}^{-1}$  shows a moderate softening and broadening with temperature (Fig. 29) and also a discontinuous change in frequency at the transition (Fig. 30). The decrease in the vibron frequency at the transition to  $\eta'$  oxygen contrasts with observations for  $\eta$  oxygen [19,12]. This change indicates stronger intermolecular interactions in  $\eta'$  oxygen. The changes in the Raman spectra are very similar to those reported by Santoro et al. [12] at the  $\epsilon - \eta$  transition, except for the vibron discontinuity which has opposite sign in the 16-20 GPa pressure range.

Pressure dependencies of lattice parameters of  $\eta'$  oxygen from Ref. [14] in comparison with the data for  $\eta$  oxygen at 15.9 GPa [17] and for  $\beta$  oxygen at 5.5 GPa [75] are shown in Fig. 31. Pressure dependen-

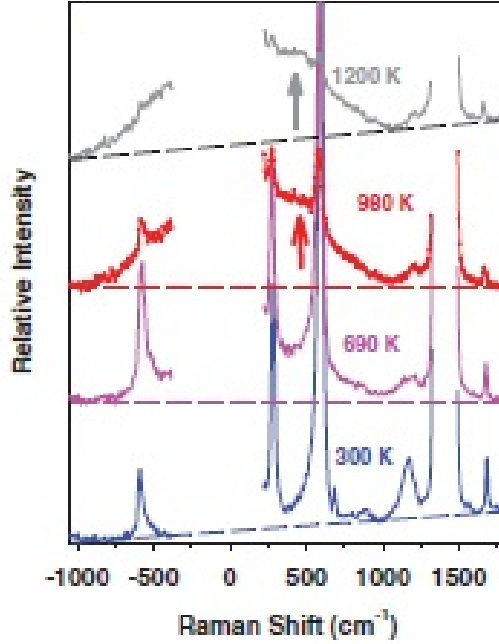


Fig. 28. (color online). Raman spectra through the  $\epsilon - \eta'$  transition showing the lack of sharp peaks in the lattice region. The arrow marks the Raman band appearing at high temperatures. (From Ref. [14].)

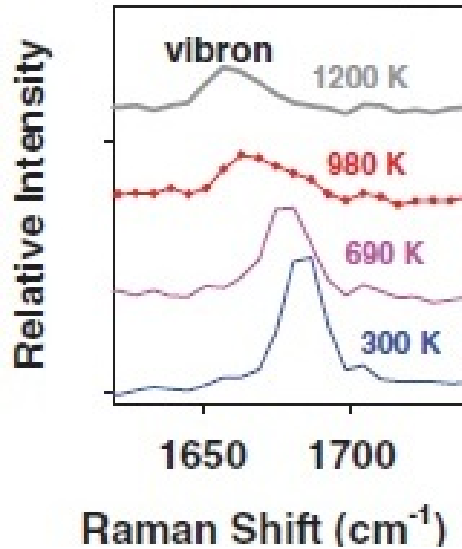


Fig. 29. (color online). Raman spectra of oxygen through the  $\epsilon - \eta'$  transition. (From Ref. [14].)

cies of density and  $c/a$  ratio in comparison with that for the  $\eta$  and  $\epsilon$  phases are shown in Fig. 32. The densities of  $\epsilon$  and  $\eta'$  phases determined in the vicinity of the transition are close to each other; thermal expansion effects are comparable to the experimental uncertainty in density determination. The density of  $\eta'$  oxygen deviates from that of  $\epsilon$  oxygen nonmonotonically; it is less dense than  $\epsilon$  oxygen at all pres-

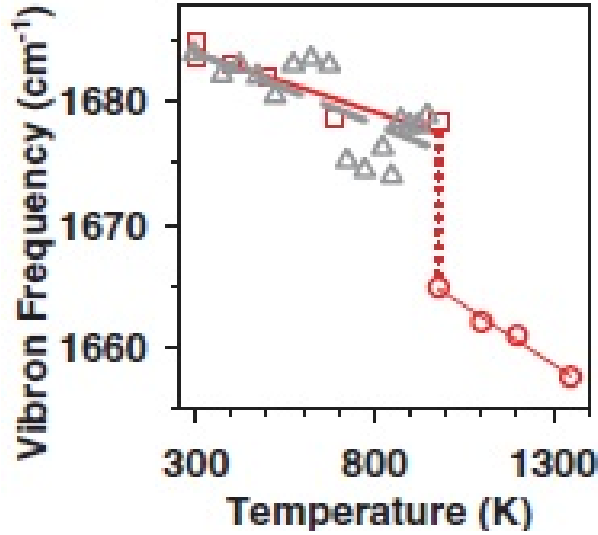


Fig. 30. (color online). Vibron frequency jump at the  $\epsilon - \eta'$  transition at 67 GPa: gray triangles resistively heated DAC; open circles and squares laser heated DAC. (From Ref. [14].)

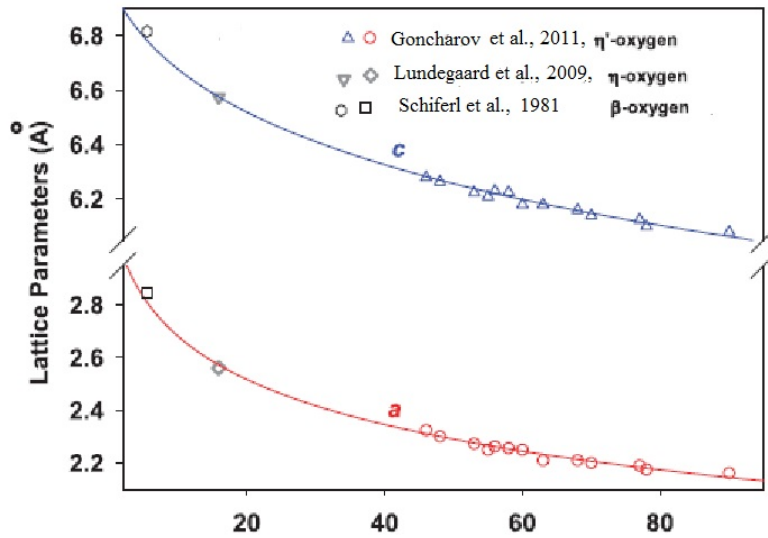


Fig. 31. (color online). Pressure dependencies of lattice parameters of  $\eta'$  oxygen from Ref. [14] in comparison with the data for  $\eta$  oxygen at 15.9 GPa [17] and for  $\beta$  oxygen at 5.5 GPa [75]. (From Ref. [14].)

sures except at 60-80 GPa (Fig. 32) with the pressure dependence of the lattice parameters of  $\eta'$  oxygen matches well to those for  $\eta$  (Ref. [19]) and  $\beta$  oxygen [75] (Fig. 31). Unfortunately, in the pressure range between 25 and 45 GPa, strong optical fluorescence precludes laser heating experiments, and further investigations are needed.

Above a certain temperature the rotational motion becomes so intensive that the rotational energy prevails the energy of molecular associ-

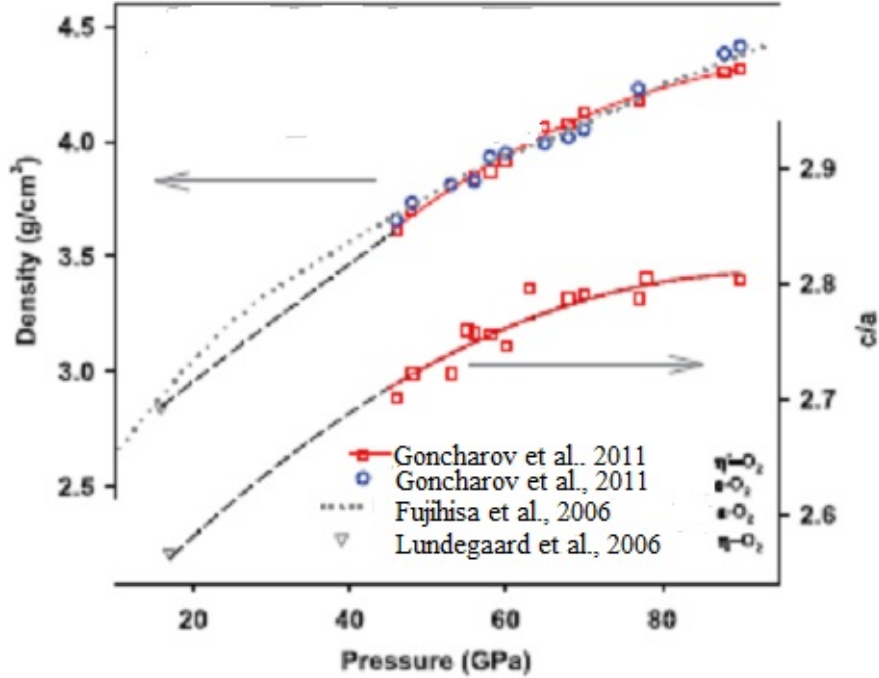


Fig. 32. (color online). Pressure dependencies of the density of  $\eta(\eta')$  and  $\epsilon$  oxygen and  $c/a$  ratio of  $\eta(\eta')$  oxygen in comparison with literature data. (From Ref.[14].)

ation, and the  $O_8$  units breaks up into  $O_2$  molecules. The Raman data (Fig. 28) show the disappearance of phonons characteristic for the  $O_8$  lattice phonons in the  $\epsilon$  phase and the appearance instead of them a new broad low-frequency band supposedly originated from rotationally disordered or weakly ordered states. Combined x-ray diffraction and Raman spectroscopy data [14] suggest that the dissociation of  $O_8$  clusters [17,18] is a signature of the phase transition to a new  $\eta'$  phase. The  $\epsilon - \eta'$  transition temperature is in the range of energy characteristic for the  $O_8$  binding energy (100 meV  $\sim$  1100 K). The  $\epsilon - \eta'$  phase transition line (Fig. 27) [14] was drawn on the base of the experimental data on the densities of  $\epsilon$  and  $\eta'$  phases. This phase line is essentially pressure independent suggesting that the corresponding transition is entropy driven. Taking into account that the *ab initio* search for equilibrium structures is typically performed for  $T = 0$  it is clear that theory could not predict the structure of  $\eta'$  oxygen. The phase boundary reveals unusual re-entrant behavior which usually (the Broken Symmetry Phase or I-II phase transition line in HD or  $He^3$  melting line [99,100]) points to the anomalous behavior of entropy. Goncharov *at al.* [14] inferred that the  $\epsilon - \eta'$  phase boundary is determined by a balance between the compression ( $VdP$ ) and entropy terms ( $SdT$ ) in

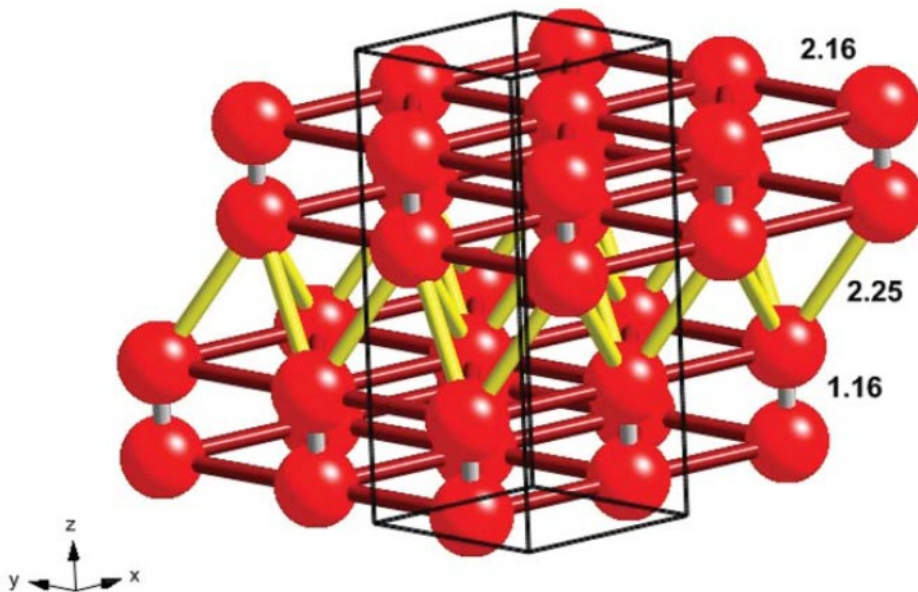


Fig. 33. (color online). Structure of the  $\eta'$  phase of solid oxygen. (From Ref. [14].)

the free energy.

X-ray diffraction data [14] show that at pressures below  $\sim 70$  GPa the  $c/a$  ratio for the  $\eta'$ -oxygen lattice increases rapidly with pressure (Fig. 32). As can be seen from Fig. 31, this happens due to faster compression in the  $a-b$  plane. Since the molecules are oriented perpendicular to this plane this brings the molecules closer to each other in the lateral directions. At pressures above 70 GPa, the shortest in-plane and out-of-plane distances between atoms in different molecules become almost equal reaching  $\sim 2.2$  Å at 90 GPa. In this pressure range, the  $c/a$  ratio is in fact pressure independent (Fig. 32), so the compression becomes isotropic. The structure of  $\eta'$  oxygen, showing the shortest interatomic distances, is depicted in Fig. 33. Each atom in  $\eta'$  oxygen has nine such neighbors, which differs essentially from the  $O_8$  cluster structure of  $\epsilon$  oxygen where each atom has only two closest intermolecular neighbors (Fig. 8) at much shorter distance (1.95 Å at 90 GPa) [18]. For the structure of  $\eta'$  oxygen shown in Fig. 33 the molecular re-association is unlikely which is consistent with a lack of sharp lattice modes in Raman spectra up to the highest observed pressure of 95 GPa [14].  $\eta'$  oxygen remains stable up to pressures close to 100 GPa.

## 6 Magnetic properties

### 6.1 Magnetic structure of the $\alpha$ phase

Magnetism of the oxygen molecule was discovered by Faraday [3] who found that gaseous oxygen is a paramagnet. Paramagnetic nature of liquid oxygen was found by Dewar [52]. The first measurements of the magnetic susceptibility of solid oxygen were performed in Leiden Laboratory by Kamerlingh Onnes and Perrier [101]. The conclusion that the low-temperature  $\alpha$  phase is magnetically ordered, was made by Giaque and Johnston [53] on the base of entropy considerations and confirmed in neutron diffraction studies by Alikhanov [54]. In the  $\beta$  phase the long-range magnetic order is absent, but there is a strong short-range magnetic order [56]. Magnetic interactions are responsible for the structural transition from the rhombohedral  $\beta$  phase to the monoclinic  $\alpha$  phase at 23.8 K at ambient pressure. The phase diagram in the  $P - T$  range of the magnetic phases is shown in Fig. 34. The two-sublattice collinear magnetic structure of the  $\alpha$  phase (Fig. 35) has been established in neutron diffraction study by Alikhanov [55]. Krupskii et al. [5,6] have shown that  $\alpha$ -O<sub>2</sub> is a quasi-two-dimensional magnet, that is, for the inter- and intrasublattice in-plane exchange magnetic constants  $J_1$ ,  $J_2$ , and the interplane exchange interaction constant  $J_3$  (Fig. 35) the inequality  $J_1, J_2 \gg J_3$  holds. The theoretical models with the three exchange constants was shown to describe, in fact, the whole body of the magnetic properties of  $\alpha$ -O<sub>2</sub> [7].

On the basis of thermodynamic and optical data of  $\alpha$ - and  $\beta$ -O<sub>2</sub> Krupskii et al. [5,6] and Slusarev et al. [102,103] found the exchange interaction constants and calculated the contribution of the magnetic subsystem into the total crystal energy. They found that magnetism plays an important role in stabilization of the structures of these phases. A general conclusion was that "solid oxygen is a unique crystal combining properties of a simple molecular solid and of a magnet. Unlike conventional magnets, the exchange interaction in solid oxygen acts on the background of weak van der Waals forces providing a significant part of the total lattice energy. As a result, the magnetic and lattice properties in solid oxygen are very closely related, which is manifested

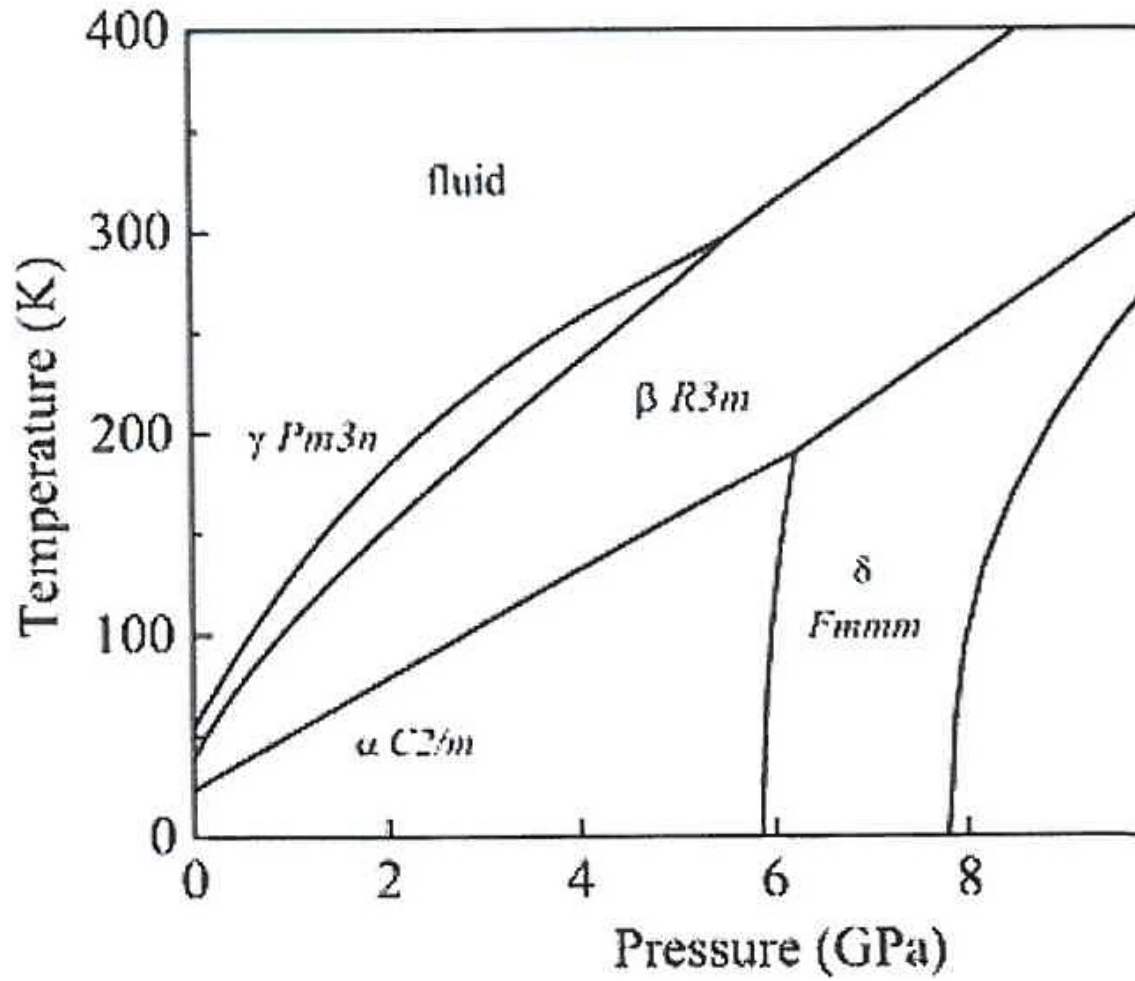


Fig. 34. Phase diagram in the  $P - T$  range of the magnetic phases.

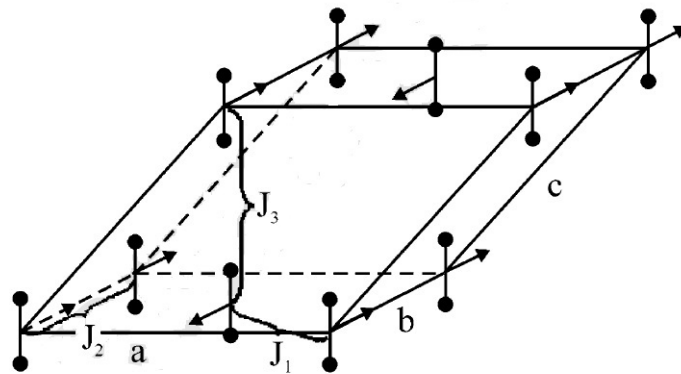


Fig. 35. A model of the magnetic structure of  $\alpha$ -O<sub>2</sub> showing three exchange interaction constants.  $J_1$  and  $J_2$  are the intraplane constants of inter- and intra-sublattice exchange interactions, respectively;  $J_3$  is the interplanar exchange interaction constant. (From Ref. [7].)

itself in a very rich phase diagram and numerous anomalies in the thermal, magnetic and optical properties” [7].

In the region of stability of the  $\alpha$  phase ( $P < 6.2$  GPa) a strong enhancement of magnetic intermolecular interaction was found. The transition temperature to the long-range ordered antiferromagnetic state increases by an order of magnitude, from 23.8 K at  $P = 0$  up to 200 K at  $P = 6.2$  GPa. It was found that the magnetic signal disappears exactly at the  $\alpha - \beta$  transition point. These results provide a direct confirmation of the magneto-structural (magneto-elastic) origin of the  $\alpha - \beta$  transition in a wide range of pressures [104].

### 6.2 Giant magneto-volume effect

The giant magneto-volume effect in solid oxygen was found in x-ray diffraction measurements of  $\alpha$ -O<sub>2</sub> under an applied magnetic field [105]. The volume of  $\alpha$ -O<sub>2</sub> was found to expand with increasing magnetic field: the lattice constants  $a$  and  $b$  elongate, while the lattice constant  $c$  and the angle  $\beta$  are almost independent of the magnetic field. The maximum volume expansion observed was about 1% under magnetic field 7.5 T, which is a giant effect compared to the volume change observed in ferromagnetic metals, such as Fe, Co and Ni. This observation agrees with the field-induced dilation predicted from exchange magnetostriction in the antiferromagnetic  $\alpha$ -O<sub>2</sub> [106].

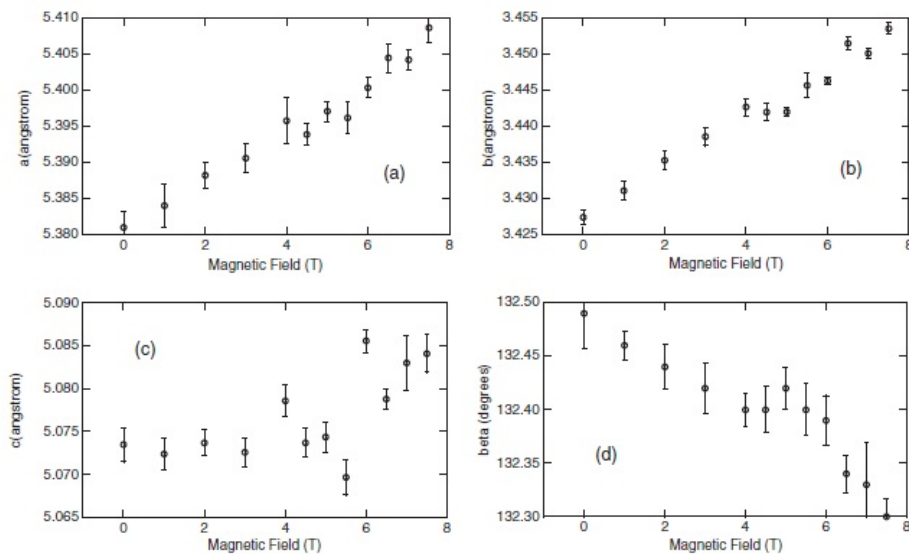


Fig. 36. Giant magneto-striction effect. (From Ref. [105].)

Data derived from diffraction by  $\alpha$ -O<sub>2</sub> in an applied magnetic field up to 7.5 T are displayed in Fig. 36(a)-(d). Seven diffraction peaks, namely, (001), (002), (020), (201), (202), (312) and (311) were used to obtain the lattice constants shown in Fig. 36 from the least-squares fitting. The lattice constants  $a$  and  $b$  increase with increasing magnetic field, while the lattice constant  $c$  changes slightly and the angle  $\theta$  is almost independent of the field. The change in the lattice constant  $c$  is about one-third of that of  $a$  and  $b$ . The maximum volume expansion observed is about 1%. For comparison, it is known that ferromagnetic metals, such as Fe, Co and Ni, show a magneto-volume effect and the volume expansion in Fe is about 0.004% [8].

Baryakhtar et al. studied the  $\alpha - \beta$  transition under an applied magnetic field,  $H$ , and predicted that the transition temperature decreases with increasing  $H$ , because  $H$  diminishes the non-isomorphic,  $\alpha$ -O<sub>2</sub> part of the exchange magnetostriction and the corresponding gain in the magneto-elastic energy. On reaching the saturation field,  $H_s$ , from the antiferromagnetic to paramagnetic phase the non-isomorphic magnetostriction vanishes and the material reverts to its high symmetry, paramagnetic phase [106].

### 6.3 Susceptibility measurements under pressure

Magnetic behavior of a substance can be observed and explained by indirect measurements like neutron, optical and electronic spectra, x-ray scattering and structural analysis or electronic transport measurements. The only direct way of straightforward probing magnetic properties over a wide  $P$ - $T$  range is magnetic susceptibility measurements. Investigations of the magnetic susceptibility of condensed oxygen have a long story and were initiated as early as at 1910 by Kamerlingh Onnes [101]. For a summary and detailed discussion of literature on the magnetic susceptibility data see Sec. 6.1, Ref. [7]. The measurements mostly were performed at ambient pressure, the only measurement at elevated pressure up to 0.8 GPa were done by Meier et al. [107].

The dc magnetic susceptibility (magnetization) of O<sub>2</sub> at elevated pressure was measured by Mito et al. [44] as a function of temperature at

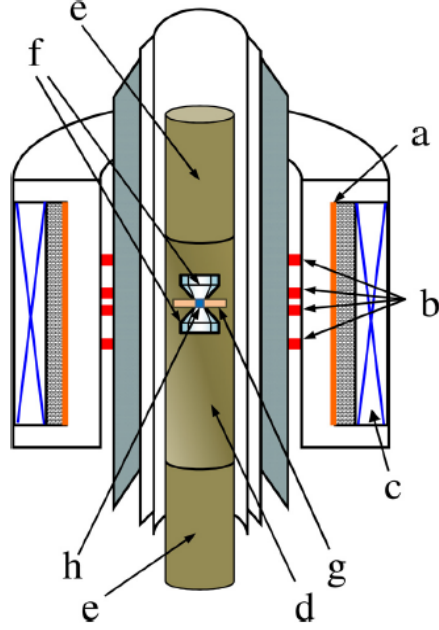


Fig. 37. (color online). Layout of high-pressure magnetic measurement system consisting of SQUID magnetometer and miniature DAC. (a) magnet for ac field, (b) detection coil, (c) superconducting magnet for dc field, (d) mDAC, (e) dummy cells, (f) diamond anvils, (g) gasket, (h) oxygen. (From Ref. [44].)

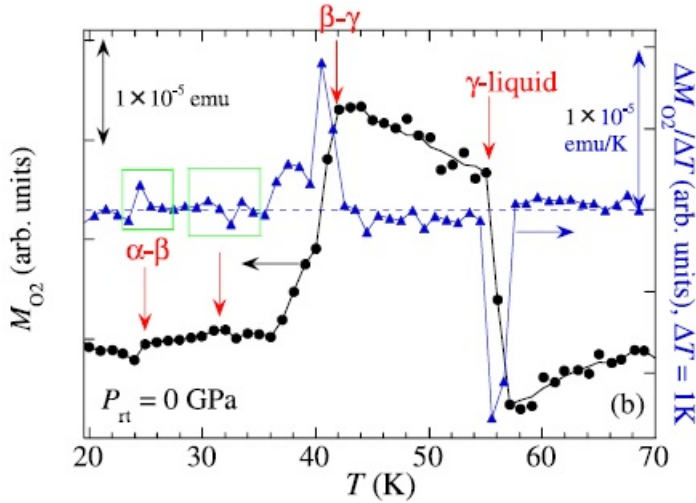


Fig. 38. (color online). Temperature dependence of magnetization  $M$  of solid  $O_2$  at ambient pressure. Temperature dependence of both  $M_{O_2} = M_{total} - M_{background}$  and  $\Delta M_{O_2}/\Delta T$  for  $\Delta T = 1$  K.  $\Delta M_{O_2}/\Delta T$  data are useful for separate consideration of a few anomalies existing in a narrow temperature range. Some magnetic anomalies are marked with arrows. Dotted green squares are guides for the eyes, indicating the existence of magnetic anomalies similar to those observed at  $P = 2.3$  GPa (see Fig. 39). (From Ref. [44].)

a certain dc magnetic field using a SQUID magnetometer. Pressures up to 3.3 GPa were attained using an miniature DAC (mDAC) made of CuBe, which could be inserted into the SQUID magnetometer (Fig. 37). The detection coil is located in a thermal bath of liquid helium,

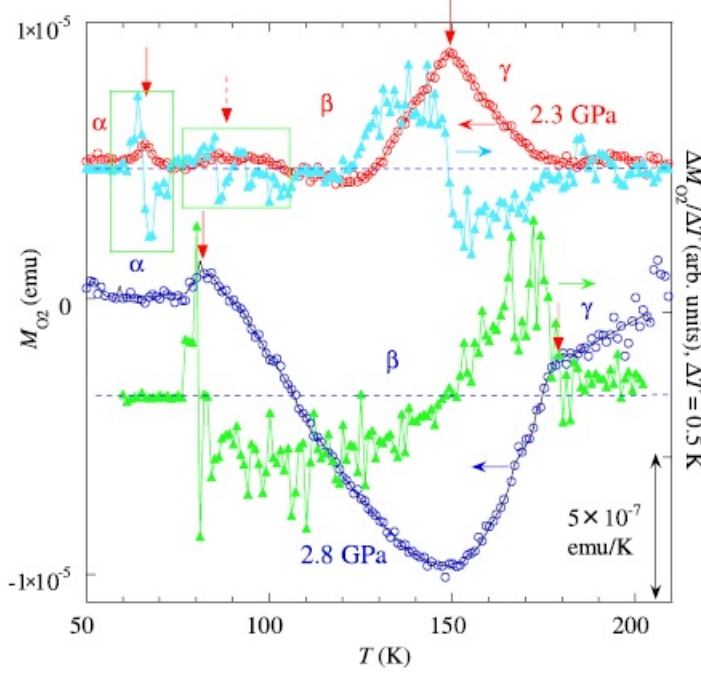


Fig. 39. (color online). Temperature dependence of magnetization  $M$  of  $O_2$  molecules at  $P = 2.3$  and  $2.8$  GPa.  $\Delta M_{O_2}/\Delta T$  evaluated for  $\Delta T = 0.5$  K is useful for separate consideration of small anomalies in a narrow temperature range. Broken horizontal line represents  $\Delta M_{O_2}/\Delta T = 0$ . Some magnetic anomalies are marked with arrows. Dotted green squares are the guides for the eyes indicating magnetic anomalies similar to those observed at ambient pressure (see Fig. ??). (From Ref. [44].)

where the superconducting magnet for the dc field is located. In a refrigerator with liquid nitrogen, the mDAC was immersed in liquid oxygen in order to introduce it into the sample cavity. The experimental shortage of this design which is due to the small size of the mDAC is the very weak signal of  $M_{\text{total}} - M_{\text{background}}$ . Nonetheless, the setup was successfully used to investigate the susceptibility of  $\gamma$ ,  $\beta$ , and  $\alpha$  oxygen at elevated pressures.

Figure ?? shows the temperature dependencies of the magnetization  $M$  of  $O_2$  ( $M_{O_2} = M_{\text{total}} - M_{\text{background}}$ ) and  $\Delta M_{O_2}/\Delta T$  for  $\Delta T = 1$  K at ambient pressure. From the temperature dependence curves the three structural transitions are confirmed as the  $\alpha - \beta$  transition at 24.7 K,  $\beta - \gamma$  transition at 41.7 K, and  $\gamma$ -liquid transition at  $T_c = 55.1$  K. These estimated transition temperatures are consistent with known results of  $T_{\alpha-\beta} = 23.8$  K,  $T_{\beta-\gamma} = 43.8$  K, and  $T_c = 54.4$  K [7]. The three transitions also exhibit characteristic anomalies in the  $\Delta M_{O_2}/\Delta T$  data. The magnitude of the magnetic signal of  $O_2$  at around 50 K is on the order of  $2 \times 10^{-5}$  emu, corresponding to 2.4% of

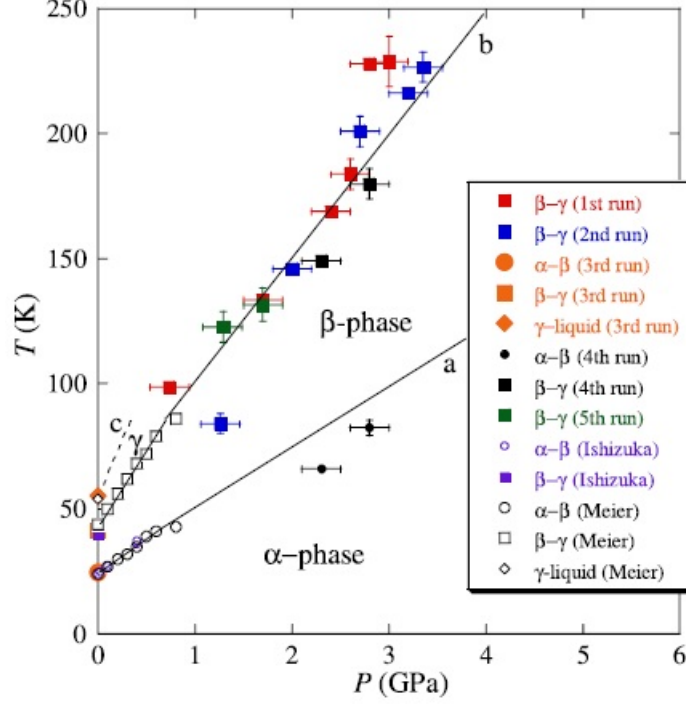


Fig. 40. (color online). Phase diagram of  $T$  vs.  $P(T)$  for  $O_2$  molecules: closed and open circles,  $\alpha - \beta$  transition; closed and open squares,  $\beta - \gamma$  transition, and closed and open diamonds,  $\gamma$ liquid transition. For reference, the data obtained by Meier et al.[107] and Ishizuka [108] are also shown. Lines  $a$  and  $b$  denote the  $\alpha - \beta$  and  $\beta - \gamma$  transition lines determined via x-ray data [74,109] and Raman studies [110,68], respectively. The melting line ( $\gamma$ -liquid transition) reported by Mills and Grilly [111] is also shown (broken curve indicated by  $c$ ). (From Ref. [44].)

the total magnetic signal. The respective curves obtained at elevated pressures are shown in Fig. 39.

As a test of obtained experimental data the authors plotted the phase diagram of solid  $O_2$  as functions of  $P$  and  $T$  obtained from the susceptibility measurements (Fig. 40). For reference, the data obtained by Meier et al. [107] and Ishizuka [108] are also shown. The solid lines ( $a$  and  $b$ ) exhibit the phase boundaries of the  $\alpha - \beta$  and  $\beta - \gamma$  transitions as investigated by x-ray [74,109] and Raman studies [110,68], respectively, are in agreement with transition temperatures from the susceptibility measurements by Mito et al. [44]. The melting line reported by Mills and Grilly [111] is also shown as the broken curve ( $c$ ). Thus, the data obtained in the susceptibility measurements successfully reproduced the phase diagram of solid  $O_2$ . The authors believe that the design they used for the susceptibility measurements at pressures up to 3.3 GPa is technically possible to develop for the measurements in the 8 -12 pressure range and thus to observe the phase transition from

the magnetic  $\delta$  phase to the nonmagnetic  $\epsilon$  phase.

#### 6.4 *Magnetic properties of the $\delta$ phase*

One of the most important questions which emerged immediately after the  $\delta$  phase was discovered in 1979 [57] and its crystallographic structure was identified [76], was the question on the magnetic nature of this phase. Contrary to the case of the  $\alpha$  phase, where this question was solved in direct magnetic and neutron measurements (see review article [7] and references therein), the  $\delta$  phase became available for the diamond anvil cell neutron studies only a quarter century later when Igor Goncharenko<sup>\*\*</sup> developed a specific spectrometer, dedicated to high-pressure neutron powder diffraction.

By this time a large amount of information has been obtained by Bini's optical research group at the European Institute for Nonlinear Optics (Florence)[62–66]. IR spectroscopy is a powerful tool to study the magnetic ordering in solid oxygen. The presence of IR absorption peaks at the intramolecular vibron frequency is related to the long-range antiferromagnetic order of molecular spins. The presence of long-range magnetic order leads to a doubling of the crystallographic unit cell. Without this doubling, the molecular vibron would be inactive in the IR absorption spectra, but only in the Raman spectrum. As a result, the vibron IR absorption is although indirect, but a sensitive probe to study the antiferromagnetic order in the  $\alpha$  and  $\delta$  phases. The results of these studies are reviewed in Ref. [7] (see Section 6.8 and 8.3). In particular, the FTIR (Fourier Transform IR) spectroscopy data provided information on the pressure dependence of the exchange parameters in the  $\delta$  phase, the temperature dependencies of the long- and short-range magnetic order parameters and the effect of the loss of long-range magnetic order under the  $\delta - \beta$  transition on the spectroscopic characteristics. Based on the data on the pressure dependence of the  $\delta$  phase lattice parameters [66], in Refs. [7,113] the pressure dependence of the exchange field in the  $\delta$  phase has been obtained and the Neel temperature has been estimated, which matched the temperature of

---

<sup>\*\*</sup>Igor Goncharenko disappeared in a scuba diving accident in the Red Sea on 4 November 2007 (see Obituary Ref. [112]).

the  $\delta - \beta$  transition.

The first neutron diffraction study of solid oxygen under pressure was performed by Goncharenko et al. [27]. Compression of a sample with the dimensions of about  $0.5 \text{ mm}^3$  was carried out in an anvil cell made of superhard boron nitride. By implementing focusing devices with supermirrors on a diffractometer already equipped with a multi-detector and installed on a cold neutron source Goncharenko created a new technique that made it possible to increase the neutron flux by one order of magnitude. In Ref. [114] he described the pressure cells with diamond and sapphire anvils and neutron instrumentation which according to the project would allow the neutron diffraction experiments to be carried out under pressures as high as 50 GPa, temperatures down to 0.1 K, and applied magnetic fields up to 7.5 T (see Ref. [115]).

Since the crystal structures of  $\delta\text{-O}_2$  and  $\alpha\text{-O}_2$  have similar hexagonal  $ab$  basal planes and can be described by the same monoclinic unit cell with only slightly different lattice parameters, there was the consensus in literature that their magnetic properties should be very close, showing just a small shift in the neutron diffraction peak position due to the small change in lattice parameters [7]. Unexpectedly, a new magnetic peak, indexed as (100), that was not present in the  $\alpha$  phase and not seen in x-ray studies (see Fig. 41). was observed in the region of stability of  $\delta\text{-O}_2$  ( $P = 6.2 \text{ GPa}$  and  $T < 100 \text{ K}$ ). Observation of the

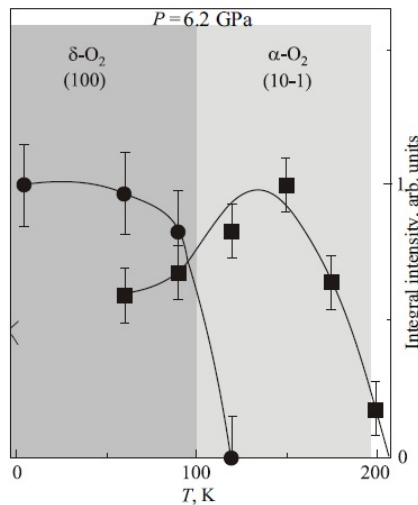


Fig. 41. Temperature dependencies of integrated intensities of the  $(10\bar{1})$  magnetic peak from  $\alpha\text{-O}_2$  and the  $(1\ 0\ 0)$  magnetic peak from  $\delta\text{-O}_2$ . (Modified from Refs. [7,27].)

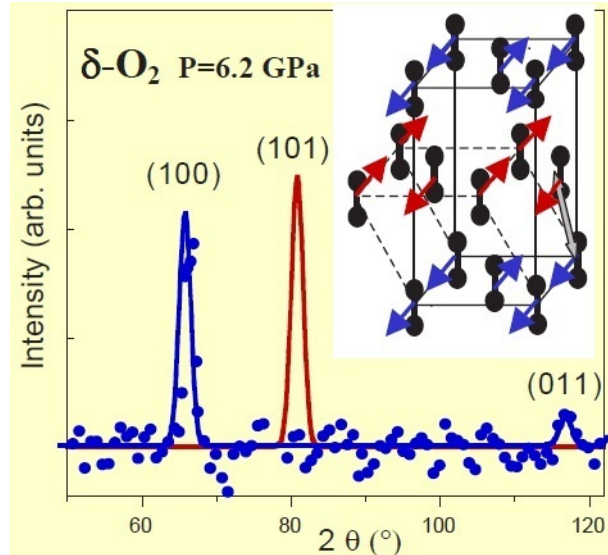


Fig. 42. (color online). Dots: experimental data on magnetic scattering in  $\delta\text{-O}_2$  at  $P = 6.2$  GPa and  $T = 4$  K. Lines: calculated profiles assuming the same type of magnetic structure as in  $\alpha\text{-O}_2$  (in red) and new type of magnetic structure shown in inset (in blue). (Modified from Refs. [7,27].)

magnetic peak was the direct proof of the antiferromagnetic nature of  $\delta\text{-O}_2$ . As can be seen from Fig. 41, with increasing temperature this peak disappears at the  $\delta - \alpha$  transition while the magnetic peak (1 0 -1) characteristic of the magnetic structure of  $\alpha\text{-O}_2$  appears. Surprisingly, comparison of the neutron diffraction patterns of the  $\alpha$  and  $\delta$  phases showed that their magnetic structures are completely different. Analysis of the diffraction pattern shown in Fig. 42 revealed that in contrast to the antiferromagnetic interaction between the nearest neighbors in adjacent close-packed planes in the  $\alpha$  phase, the interac-

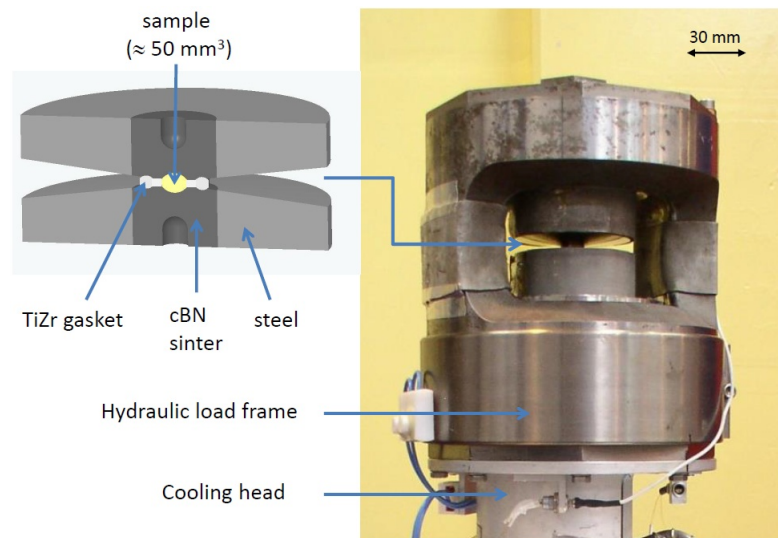


Fig. 43. (color online). DAC for neutron studies [20,115]. By the courtesy of S. Klotz

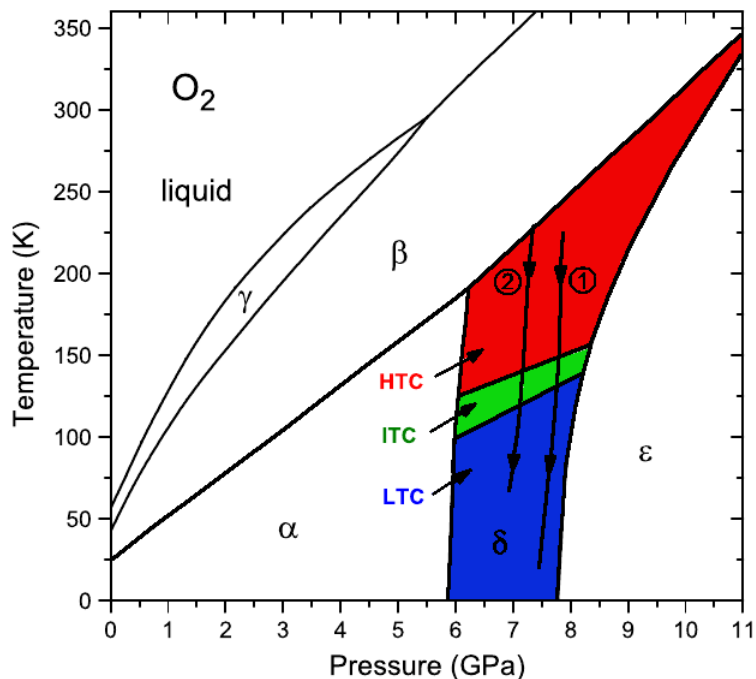


Fig. 44. (color online). Phase diagram of oxygen displaying the section investigated in the neutron diffraction study Ref. [20]. The thin vertical lines (1) and (2) indicate trajectories along which diffraction data were collected in the experiments [20]. Red, green and blue regions represent the HTC (high temperature commensurate), ITC (intermediate temperature commensurate) and LTC (low temperature commensurate) phases, respectively. (Modified from Ref. [20].)

tion between these neighbors in the  $\delta$  phase is ferromagnetic (Fig. 42, inset).

The observed magnetic reflection in  $\delta$ -O<sub>2</sub>, that cannot be described in terms of the primitive chemical unit cell is a direct proof that as is the case for  $\alpha$ -O<sub>2</sub> the magnetic nature of the  $\delta$ -O<sub>2</sub> phase is antiferromagnetic. Nevertheless the comparison of the neutron diffraction data obtained for the two phases showed that while the magnetic order of the molecules located in the close-packed planes in both phases are the same, the three-dimensional magnetic structures are completely different. As can be seen from Fig. 42, the magnetic arrangement obtained for the  $\delta$ -O<sub>2</sub> phase from the analysis of the neutron diffraction pattern, instead of the antiferromagnetic interaction between nearest neighbors in adjacent close-packed planes characteristic for the  $\alpha$  phase, in the  $\delta$  phase the interaction of such neighbors turned out to be ferromagnetic. The strong (100) reflection and the weak (011) reflection suggest that the magnetic moments in the  $\delta$  phase are also directed along the **b** axis.

The ferromagnetic coupling between the O<sub>2</sub> neighboring planes found in  $\delta$ -O<sub>2</sub> was rather surprising. This result was not suggested by indirect optical measurements or *ab initio* calculations where magnetically disordered [75] or the same antiferromagnetic stacking of the O<sub>2</sub> planes as in  $\alpha$ -O<sub>2</sub> were previously suggested [88]. Moreover, this seemed to contradict to the general belief that the exchange interaction between the O<sub>2</sub> molecules is always antiferromagnetic and rapidly decrease with distances [88]. Thus in order to explain the magnetic structure of the  $\delta$ -O<sub>2</sub> phase Goncharenko proposed that it is necessary to take into account the exchange interactions between the spins belonging to the next-nearest neighboring. This suggesting was latter supported by the work of Gomonay and Loktev [31,47].

The IR experiments suggested that the long-range antiferromagnetic arrangement of the molecular spins exists in the whole region of the  $\delta$  phase, but does not reveal the nature of the ordering. Therefore to accomplish this task a second neutron diffraction study of  $\delta$ -O<sub>2</sub> was

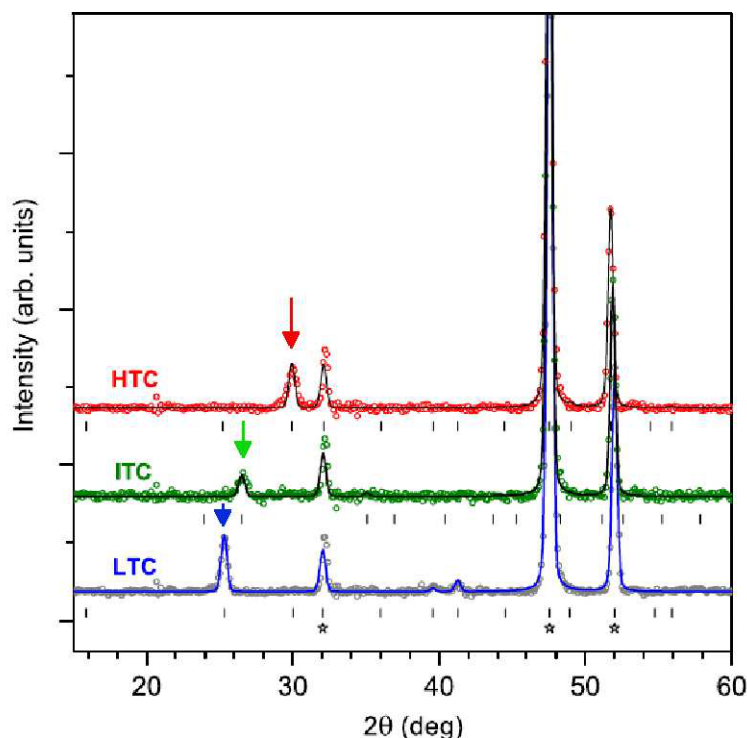


Fig. 45. (color online). Neutron powder diffraction patterns of  $\delta$ -O<sub>2</sub> in three different magnetic phases LTC, ITC and HTC ( $\lambda = 1.87\text{\AA}$ ). The lines through the data (circles) are Rietveld fits to the nuclear and magnetic structure. Tickmarks correspond to positions of magnetic reflections, stars to those of the nuclear (002), (111), (200) Bragg peaks. (Modified from Ref. [20].)

carried out by Klotz et al. [20] using the setup schematically shown in Fig. 43 (see Ref. [115]). This time both the intensity of the beam and the sample size were considerably increased. The intensity of the beam was increased by several orders of magnitude and the size of the sample was increased to about  $70 \text{ mm}^3$ , more than two orders of magnitude. This upgrade in the sample characteristics and the use of Rietveld refinement methods allowed the study of both the crystallographic and magnetic structures of  $\delta\text{-O}_2$  and their mutual interplay. Additionally it was also possible to visit a large region of existence of this phase, in particular, between the phase boundaries of the  $\alpha\text{-}\delta$  and  $\delta\text{-}\epsilon$  transitions (20-240 K and 6-8 GPa). Two trajectories were followed to collect the diffraction data, these two quasi-isochoric trajectories are shown by the lines 1 and 2 in the phase diagram of Fig. 44.

Figure 45 shows the neutron diffraction data obtained by scanning the  $P - T$  phase diagram along the trajectory line 1 shown in Fig. 44. An analysis of these data revealed another unique feature of the

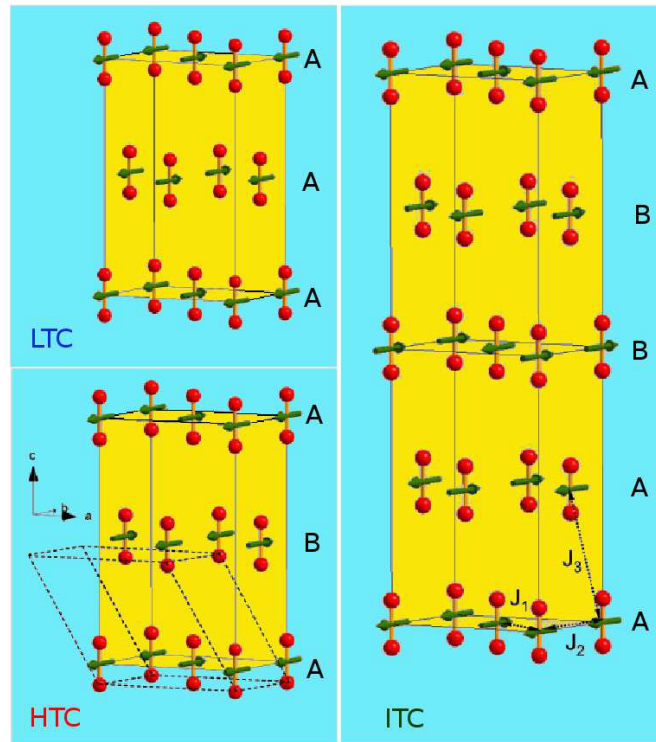


Fig. 46. (color online). Magnetic structures in  $\delta\text{-O}_2$ . Upper Left: the low temperature commensurate (LTC) structure. Lower left: the high temperature commensurate (HTC) phase. Right: the intermediate commensurate (ITC) phase. The unit cell of the low-pressure  $\alpha$  phase (dashed) illustrates the close structural relationship between the two phases, having identical magnetic structures. "A" and "B" denote magnetic stacking sequence,  $J_1$ ,  $J_2$ , and  $J_3$  the intra- and interplane exchange parameters. (Modified from Ref. [20].)

magnetism of solid oxygen (in addition to the fact the exchange interaction is a substantial part of the lattice binding energy [6,7]): it was found that inside the same lattice structure of the  $\delta$  phase there exist three different magnetic structures. The high temperature (above 149 K) diffraction data show a strong magnetic reflection at  $2\theta = 30^\circ$  (marked by the red arrow in Fig. 45), a peak that is different from the one reported in the previous neutron diffraction study [27]. This magnetic reflection corresponds to the spin alignment identical to the one in  $\alpha$ -O<sub>2</sub> and was called the high temperature commensurate (HTC)  $\delta$  phase. At temperatures between 132 K and 149 K a second magnetic reflection was observed at  $2\theta = 26.5^\circ$  (marked by the green arrow in Fig. 45). This reflection peak is also nonconsistent with the one obtained in Ref. [27] but correspond to a more complex antiferromagnetic structure with a doubling along the  $c$  axis. This new magnetic structure was called intermediate temperature commensurate (ITC)  $\delta$ -O<sub>2</sub>. Finally, at low temperatures (lower than 132 K) the results coincides with the one reported in the neutron diffraction studies by Goncharenko et al. [27] having the magnetic reflection peak at  $2\theta = 25^\circ$  (marked by the blue arrow in Fig. 45). This phase was called low temperature commensurate (LTC)  $\delta$ -O<sub>2</sub>. All three magnetic phases are shown in Fig. 46. The same sequence of phases was observed in the path 2 (Fig. 44) shifted downward on 0.5 GPa.

None of these magnetic transitions has an appreciable effect on the spatial structure of the  $\delta$  phase. Thus, no direct connection between the spatial and spin degrees of freedom has been established. Nonetheless an indirect connection exists - the magnetic structures in  $\delta$ -O<sub>2</sub> influence on the  $\alpha - \delta$  phase transition. As was said above in Sec. 2, geometrically the  $\alpha - \delta$  phase transition can be described as a continuous small change of the monoclinic angle  $\beta'$  (see Fig. 2 Left), that is as a second order phase transition (the Lifshitz criterium for the second order phase transitions [116] is satisfied). Nonetheless, the lattice dynamics calculations by Eters et al. [117] supported later by the results of optical studies detecting small jumps both in IR [109] and Raman [28] vibron frequencies indicated to the first order phase transition. As was marked by Klotz [115], the existence of the different magnetic structures in  $\alpha$ -O<sub>2</sub> and LTC structure in  $\delta$ -O<sub>2</sub> shows unambiguously that this transition cannot be of the second order.

Given the similarity of the spatial structures of  $\alpha$ - and  $\delta$ -O<sub>2</sub>, the ratios of the intra- and interplanar exchange parameters  $J_1$  and  $J_2$  are close, and the problem of the magnetic structure of  $\delta$ -O<sub>2</sub> is reduced to determining the orientation of spins in the planes and the nature of plane packing along  $\langle 001 \rangle$ . Study of the magnetic diffraction patterns showed that the  $z$ -components of the spins can be assumed to be zero, i.e., it can be assumed that the spins are in the  $ab$ -planes and, similar to the case of  $\alpha$ -O<sub>2</sub>, are oriented along the  $b$ -axis. The interplane magnetic structure is determined by the nature of the interplane magnetic coupling, ferromagnetic or antiferromagnetic. In the case of a ferromagnetic coupling, the sequence is of the  $A - A - A$  type, and in the case of an antiferromagnetic coupling, it is  $A - B - A$ . The former and the latter correspond to the LTC and HTC structures, respectively (Fig. 42). Identification of the ITC structure proved to be more difficult. The neutron diffraction data indicate that the spatial structure of this phase has a doubled period along the  $c$ -axis as compared to the LTC and HTC structures with the ferromagnetic (F) and antiferromagnetic (AF) coupling between the nearest neighboring spins in the adjacent O<sub>2</sub> planes forming the alternate sequence F-AF-F-AF (Fig. 46). The unit cell of  $\alpha$ -O<sub>2</sub> shown by dashed line illustrates the fact that  $\alpha$ -O<sub>2</sub> and HTC  $\delta$ -O<sub>2</sub> have the same magnetic structure.

As was said above, no connection between the spatial and spin degrees of freedom has been established. In particular, the temperature dependencies of the lattice parameters (Fig. 47) do not exhibit any features at the lines of magnetic phase transitions. As shown in Fig. 47, the coefficient of thermal expansion of the  $\delta$ -O<sub>2</sub>, as well as that in  $\alpha$ -O<sub>2</sub> and  $\beta$ -O<sub>2</sub>, is anisotropic [7]. At the same time there are quite significant differences in the thermal expansion behavior of the three phases. In all three phases, the thermal expansion coefficient is negative along the  $b$ -axis. Based on this fact Krupskii et al. [6] determined the sign of the intra-sublattice exchange constant  $J_2$ . The coefficient of thermal expansion along the  $c$ -axis is positive in  $\alpha$ -O<sub>2</sub> and negative in  $\beta$ -O<sub>2</sub>. At the point of the  $\alpha - \beta$  transition, the temperature dependence of the interplane distance has a characteristic  $\lambda$ -shape anomaly [6,7]. This behavior has been interpreted in Ref. [7] as a manifestation of the interplane correlations. The antiferromagnetic interplane attraction decreases with increasing temperature and the amplitude

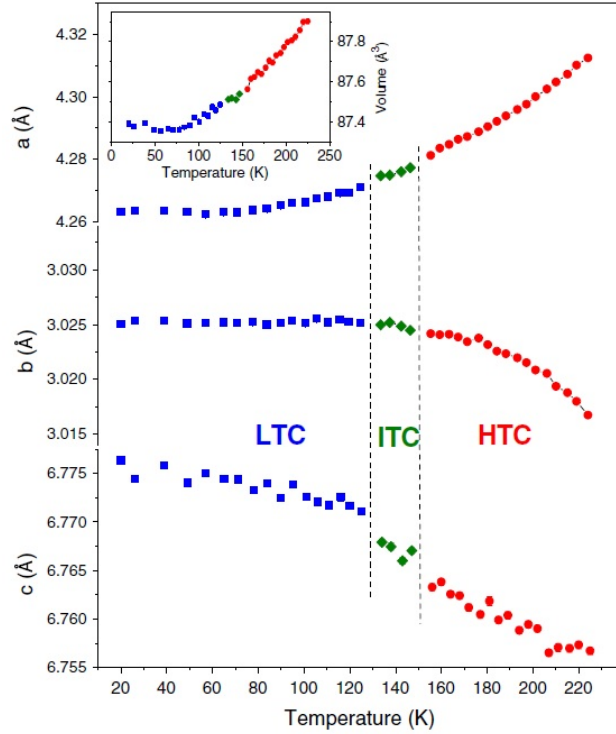


Fig. 47. (color online). Temperature dependence of the lattice parameters (main figure) and nuclear unit volume (inset) along the quasi-isobaric trajectory 1 shown in Fig. 44. (From Refs. [20,47].)

of librations increases. Both factors result in an increase of the interplane spacing with increasing temperature. A positive jump of the interplane distance upon  $\alpha - \beta$  transition may be explained by the disappearance of long-range magnetic order. At the same time, the negative thermal expansion in the  $c$ -axis direction is most likely of nonmagnetic nature, associated with a change in the character of the rotational motion. As shown in Fig. 47, the temperature behavior of the lattice parameters of  $\delta$ -O<sub>2</sub> is similar to that in  $\beta$ -O<sub>2</sub>. The coefficient is positive along the  $a$ -axis and negative along the  $b$ - and  $c$ -axes. The geometry of the close-packed planes and the spin structure remain unchanged in the  $\alpha - \delta$  transition, and therefore the magnetic properties which are determined by the intraplane factors do not undergo qualitative changes during the phase transition. One of such properties is the negative thermal expansion along the  $b$ -axis, which is observed both in  $\alpha$ -, and  $\delta$ -O<sub>2</sub> (Fig. 47). The explanation of this phenomenon for  $\alpha$ -O<sub>2</sub> proposed by Krupskii et al. [6,7] which, as noted by Gomonay and Loktev [31] remains valid for  $\delta$ -O<sub>2</sub>, is as follows. There are two different mechanisms that contribute to the thermal expansion of the lattice. The first of them, which leads to expansion with increasing

temperature, is due to the anharmonic character of the lattice vibrations. The contribution of the second mechanism associated with the exchange coupling may lead to either expansion or compression with increasing temperature. Indeed, if this interaction leads to repulsion, then the contribution to the thermal expansion due to a decrease in magnetization with increasing temperature is negative and vice versa. As shown in Fig. 47, the coefficient of thermal expansion along the  $b$ -axis, i.e., in the direction where the intra-sublattice interaction is the most significant, becomes negative above 120 K (cf. Fig. 13 in Ref. [7]), which clearly indicates the presence of an additional mechanism with a negative contribution. Thus, the intraplane intra-sublattice interaction in  $\delta$ -O<sub>2</sub>, similar to  $\alpha$ -O<sub>2</sub>, is antiferromagnetic.

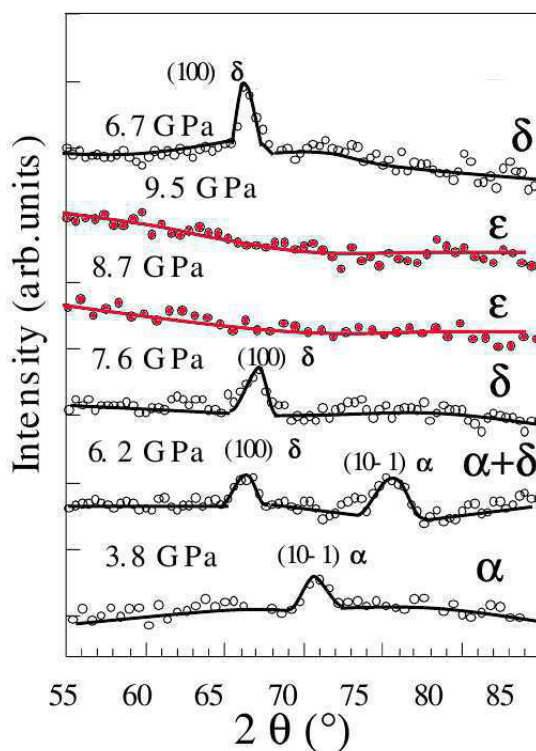


Fig. 48. (color online). Magnetic neutron-diffraction patterns at different pressures at the  $\delta$ - $\epsilon$  transition. (Modified from Ref. [21].)

### 6.5 Magnetic collapse at the $\delta$ - $\epsilon$ transition

At low temperatures the  $\delta$ - $\epsilon$  phase transition takes place at 7.6 GPa. The transition pressure increases with temperature and at  $P \approx 11.5$  GPa and  $T \approx 350$  K the  $\delta - \epsilon$  phase transition line transforms into the  $\beta - \epsilon$  transition line [7]. At a pressure of 100 GPa, the transition to the metallic  $\zeta$  phase takes place. Respectively, the  $\epsilon$  phase occupies the largest portion of the studied phase diagram.

Although the  $\delta - \epsilon$  transition was discovered as far back as 1979, its nature remained unclear in spite of numerous x-ray and optical studies. The structural x-ray studies [59,60] have shown that the  $\delta - \epsilon$  transition is accompanied by a very large jump in volume of 5 – 6%, indicating that a radical change occurs during this transition. Based on optical studies [62–66] (see review Ref. [7]), the Florence group put forward the hypothesis that the  $\delta - \epsilon$  transition is caused by the pairing of  $O_2$  molecules to form an  $O_4$  molecule with a singlet ground state. This would mean that the  $\delta - \epsilon$  transition is accompanied by a magnetic collapse and that the  $\epsilon$  phase is therefore nonmagnetic. An unambiguous answer to the question of the magnetic nature of the  $\epsilon$  phase could be obtained in direct measurements of its magnetic properties.

Neutron diffraction studies of the  $\epsilon$ -phase were first conducted by Goncharenko [21]. Figure 48 shows the neutron diffraction patterns obtained at pressures of 3.8 - 9.5 GPa. With increasing pressure from 3.8 to 7.6 GPa (neutron diffraction data were collected at cold compression), the neutron diffraction patterns show the transformation of the magnetic structure. At  $P = 3.8$  GPa, a single peak (to remove the structural peaks of non-magnetic nature, the spectra recorded in the paramagnetic region were subtracted from the low-temperature spectra) characteristic of the  $\alpha$  phase is observed in the neutron diffraction patterns. As pressure rises to 6.2 GPa, a peak characteristic of the  $\delta$  phase appears next to the  $\alpha$  phase peak in the neutron diffraction pattern, indicating that the sample is in a two-phase state. With increasing pressure, the intensity of the  $\alpha$  phase peak decreases and that of the  $\delta$ -phase increases until 7.6 GPa, when the entire sample is in the single-phase state and only the  $\delta$  phase peak remains in the neutron

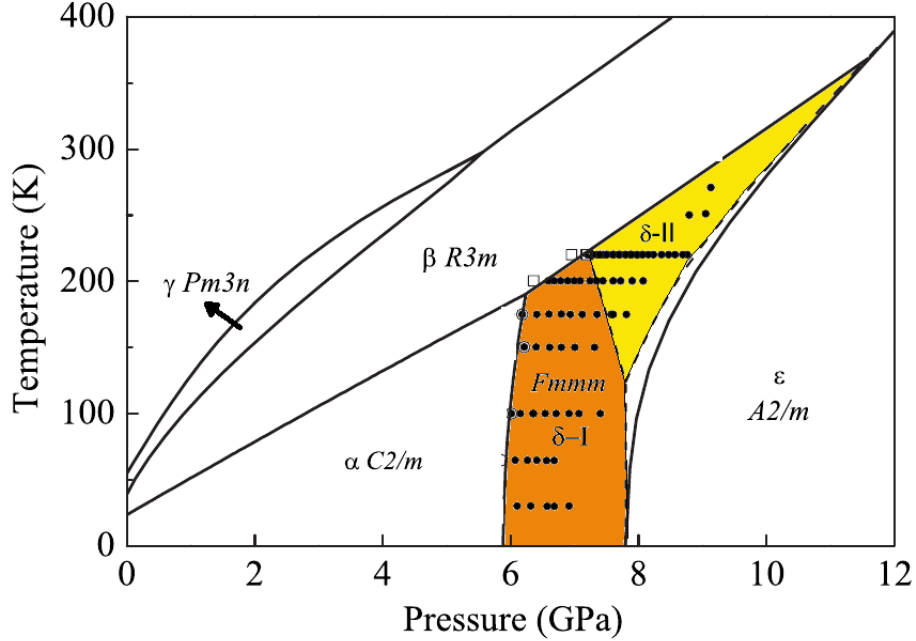


Fig. 49. (color online). Magnetostructural  $P - T$  phase diagram of oxygen. Dashed lines separating the yellow and orange regions are the new phases suggested by Goncharenko in Ref. [21]. Empty squares, full and empty circles represent points where the infrared absorption spectrum has been assigned to the  $\beta$ ,  $\delta$ , and  $\alpha$  phases, respectively. (Modified from Ref. [33])

diffraction pattern. At pressures above 8 GPa, a transition to the  $\epsilon$  phase occurs. The structural transition is accompanied by an abrupt change in the magnetic diffraction pattern. At  $P = 8.7$  GPa ( $T = 4$  K) and  $P = 9.5$  GPa ( $T = 1.5$  K) there is no magnetic peaks in the neutron diffraction patterns. The absence of the magnetic reflections indicates the absence of the long-range magnetic order in the  $\epsilon$  phase. Lowering the pressure to 6.7 GPa restores the pattern of magnetic scattering — the magnetic diffraction peaks reappear, indicating the presence of the long range magnetic order. It should be noted that the antiferromagnetic ( $\delta$ ) to supposedly nonmagnetic ( $\epsilon$ ) phase transition at 8 GPa is well separated from the insulator ( $\epsilon$ ) to metallic ( $\zeta$ ) transition at 96 GPa.

Having found that there is no long-range magnetic order in the  $\epsilon$  phase, Goncharenko came to the conclusion that this fact can be related to the magnetic properties of the  $\delta$  phase. He suggested that there is no long-range magnetic order in the  $\delta$ -phase for  $P > 8$  GPa and  $T > 120$  K (yellow region in Fig. 49).

His reasoning was as follows. According to the phase diagram in Fig.

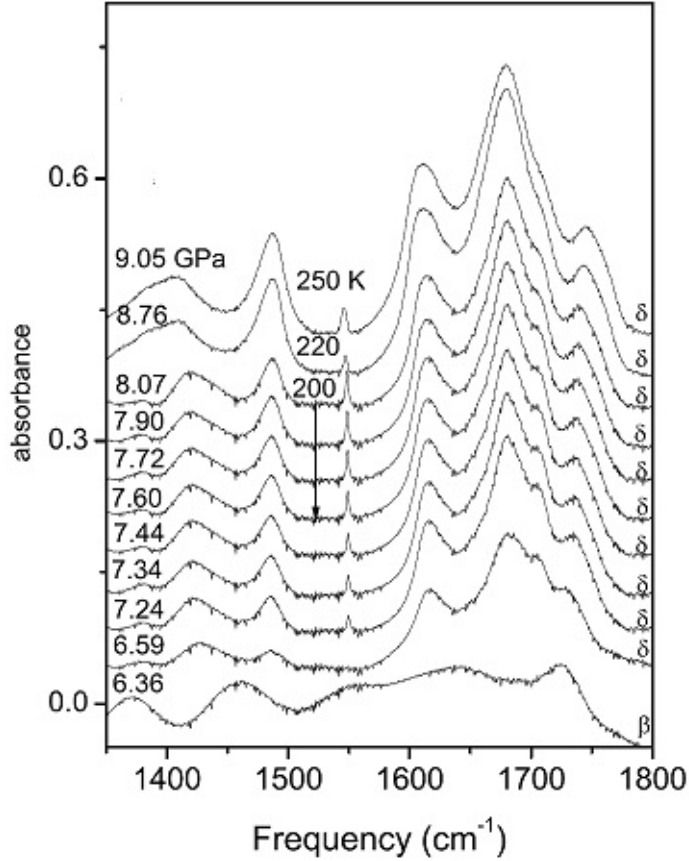


Fig. 50. IR absorption spectra obtained by scanning along the 200 K isotherm (220 K at 8.76 GPa and 250 K at 9.05 GPa). The spectra contain absorption peaks at the vibron mode frequency  $1500\text{ cm}^{-1}$  and the phonon wing in the frequency range of  $1600\text{--}1800\text{ cm}^{-1}$  (Modified from Ref. [33].)

49, in the region  $T > 120\text{ K}$ , the pressure of the  $\delta - \epsilon$  transition increases with increasing temperature, and thus, in the pressure range  $8\text{ GPa} < P < 12\text{ GPa}$ , the  $\epsilon$  phase is transformed into the  $\delta$  phase at constant pressure and temperatures above  $T_{\epsilon-\delta}$ . If there is no long-range magnetic order in the  $\epsilon$  phase, the transition to the magnetically ordered  $\delta$  phase would have meant that the long-range magnetic order appears upon increasing temperature. Although such temperature-induced magnetism is not prohibited by the laws of physics, such a phenomenon has not been observed in experiment. Thus, in Ref. [21] Goncharenko supposed that in the region of existence of the orthorhombic  $Fmmm$   $\delta$  phase, two different magnetic structures,  $\delta$ -I and  $\delta$ -II, are realized. Although his arguments are physically quite justified, this hypothesis is somewhat exotic, as there is a strong correlation between the structural and magnetic properties in all the known phases of solid oxygen. In Ref. [33], IR spectroscopy was employed to check whether the  $\delta$ -II phase is antiferromagnetic, hence subjecting Goncharenko's

hypothesis to experimental verification. Figure 49 shows the points on the  $P - T$  phase diagram in which the IR spectra were recorded to determine to which region of the phase diagram these points actually belong. Figure 50 shows the IR absorption spectra for the frequencies of the vibron mode  $\sim 1500 \text{ cm}^{-1}$  and the phonon wing  $1600\text{--}1800 \text{ cm}^{-1}$  obtained upon scanning along the isotherm 200 K (220 K at 8.76 GPa and 250 K at 9.05 GPa). As shown in Fig. 50, the vibron peak is present throughout the entire 200 K isotherm, but disappears in the  $\beta$ -phase. The 200 K isotherm intersects the hypothetical boundary of the  $\delta$ -I– $\delta$ -II transition at a pressure of about 7.3 GPa, however no features in either the vibron spectrum or the phonon wings have been observed at this pressure. The IR absorption at the vibron frequency is, as a matter of fact, an evidence of the long-range magnetic order in the  $\delta$ -II region, where, according to Goncharenko’s hypothesis, no order was assumed. Two spectra obtained for the 220 and 250 K isotherms (Fig. 50) show the presence of the vibron IR absorption peaks deep inside the region of the hypothetical  $\delta$ -II phase at pressures above the  $\delta - \epsilon$  transition at low temperatures. This observation shows that solid oxygen is apparently the only known substance, in which the magnetic ordering occurs upon increasing temperature. The nonmagnetic  $\epsilon$  phase existing at low temperatures becomes the magnetic  $\delta$  phase at higher temperatures. This exotic behavior is not forbidden from first principles, as the  $\epsilon$  phase is not paramagnetic and the phenomenon is not a magnetic order-disorder transition. This seemingly anomalous temperature-induced ordering is, as a matter of fact, a transformation of the molecular state, which occurs at the  $\delta - \epsilon$  phase transition. The structural component of the  $\epsilon$  phase at low temperatures is a diamagnetic molecule  $\text{O}_8$  [17,18] while the antiferromagnetic  $\delta$  phase at higher temperatures consists of  $\text{O}_2$  molecules with spin  $S = 1$  in the ground molecular state.

### 6.6 Magnetic properties of the $\epsilon$ phase

The experimental determination in 2006 [17,18] of the crystal structure of  $\epsilon$ - $\text{O}_2$  has opened the possibility of shedding light into other mystery of this phase – its magnetic structure. While the magnetic state of the low-pressure, low temperature phases is well understood, and the

high-pressure  $\zeta$  phase is non-magnetic (NM), magnetism of the  $\epsilon$ -O<sub>2</sub> phase remains still an open problem. Unlike two boarding phases, at lower pressures  $\delta$ -O<sub>2</sub>, an antiferromagnetic (AF)  $S = 1$  correlated insulator, and at higher pressures  $\zeta$ -O<sub>2</sub>, a regular and superconducting nonmagnetic (NM) metal,  $\epsilon$ -O<sub>2</sub> is an insulator of more complex nature. X-ray and neutron diffraction studies revealed that at the  $\delta - \epsilon$  transition simultaneously with the structural transition there is a collapse of the long-range AF Neel order. At the same time, that observations did not provide conclusive information about the nature of the ground state in  $\epsilon$ -O<sub>2</sub> and in particular about any further role played in  $\epsilon$ -O<sub>2</sub> by the spin of individual molecules, if any. In principle, a simple scenario is possible where the O<sub>2</sub> molecular magnetic state could simply collapse from  $S = 1$  to  $S = 0$  at the  $\delta - \epsilon$  transition through a Peierls type distortion, for example, dimerizing [63] or tetramerizing [118] the molecules. Further DFT calculations [30] strengthened that picture, showing that the quartet distorted geometry drives the undistorted metal to a band insulator. Moreover, DFT calculations showed that this state exhibits O<sub>2</sub> vibrations whose frequency and pressure evolution are, between 20 and 96 GPa, in good agreement with infrared (IR) and Raman data [38]. The problem is that the properties of the  $\epsilon$  phase are heterogeneous and there are differences in its behavior in the pressure range 8–20 GPa and under higher pressures [62,63,65,67,119].

### 6.6.1 Raman and IR spectroscopic studies the $\epsilon$ phase

As in the case of studies of  $\delta$ -O<sub>2</sub>, to reveal what happens to the magnetic subsystem at the  $\delta$ - $\epsilon$  transition, it is important to involve the analysis of Raman and IR spectroscopy data. The Raman spectrum of the  $\epsilon$  phase observed in experiment consists of three main bands: a high-frequency vibron peak around 1580 cm<sup>-1</sup> and two low-frequency libron bands  $L_1, L_2$  below 500 cm<sup>-1</sup>.

Figure 51 shows the vibrational patterns of the four vibron modes, two of which are Raman active modes and two are IR active. The strongest Raman peak is not visible in experiments as it lies in the diamond anvil absorption frequency region. The weakest Raman peak at around 1600 cm<sup>-1</sup> [67], corresponds to an in-phase vibration of the four molecules, while the strongest Raman mode, not seen in experiments, corresponds

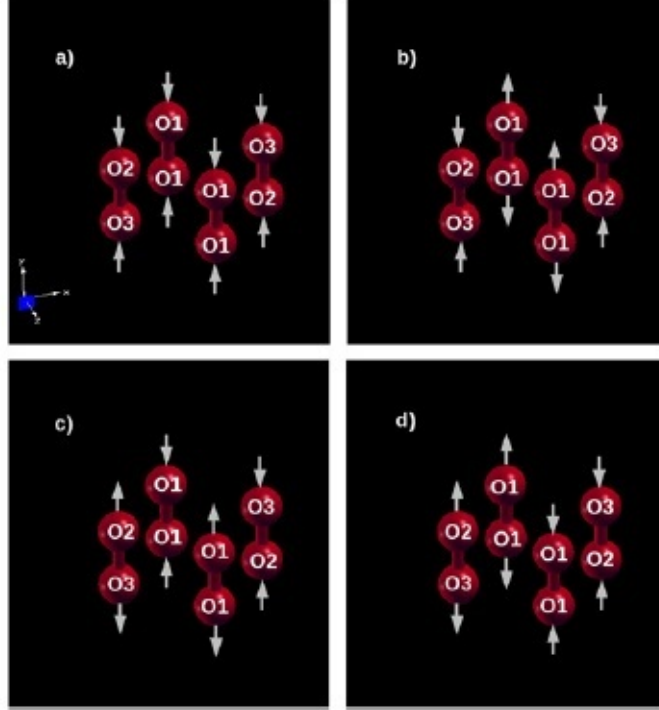


Fig. 51. (color online). Vibrational patterns of the four vibron modes. Modes (a) and (b) are Raman active vibrons with highest and lowest frequency, modes (c) and (d) are IR active. (From Ref. [38].)

to an out-of-phase oscillation with zero dipole moment. Regarding the IR active modes, they correspond to dipole-active out-of-phase oscillations. Their IR intensity depends on the direction of propagation and on the polarization of the incoming light [38].

In the low temperature study of the  $\epsilon$  phase by Carter et al. [119] it has been found that at a pressure of about 20 GPa at 20 K the splitting of the librational modes occurs (Fig. 52, upper Figure) of the order of  $10 \text{ cm}^{-1}$ , which has been interpreted as a new phase transition. In Ref. [67] the study of the pressure behavior of the librational modes (at room temperature) has been extended to the entire range of the existence of the  $\epsilon$  phase. In this work no abrupt splitting was observed but rather a continuous splitting of the librational mode (Fig. 52, bottom Figure).

The pressure dependence of the IR mode [65] (Fig. 53) is nonmonotonic. After the  $\delta - \epsilon$  phase transition the frequency rapidly decreases and reaching a minimum at  $\sim 20 \text{ GPa}$  decreases by  $50 \text{ cm}^{-1}$  and then grows slowly. The pressure dependencies of the intensities of all the modes are also nonmonotonic with the most pronounced maxi-

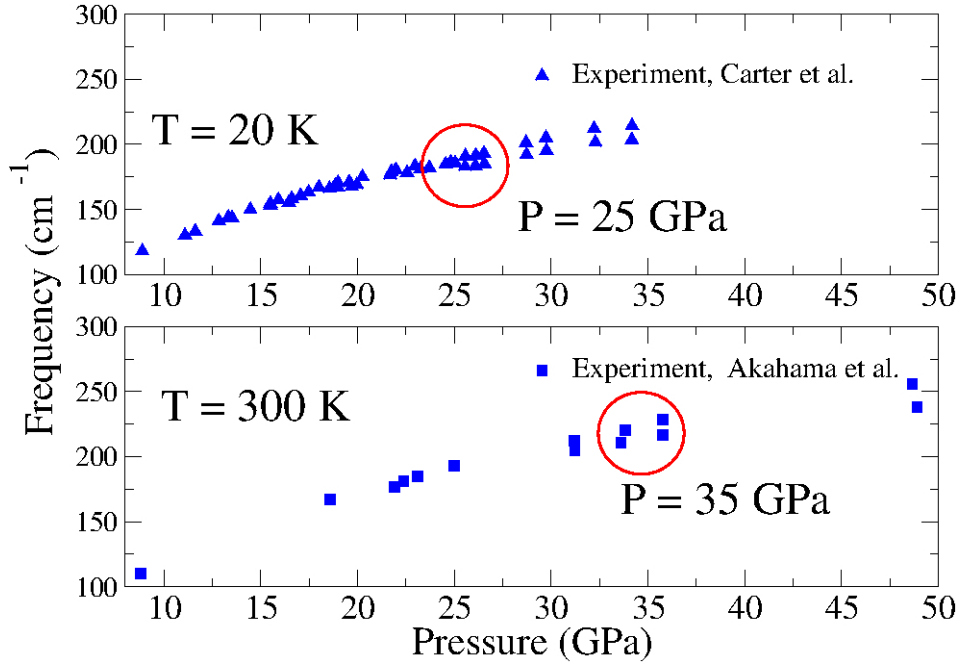


Fig. 52. (color online). Pressure dependence of the librational mode  $\nu_{L1}$ . The upper figure shows the splitting at  $P = 25$  GPa for  $T = 20$  K as obtained in Ref. [119] (modified from Ref. [119]); the bottom figure shows the splitting at  $P = 35$  GPa for  $T = 300$  K obtained in Ref. [67] (modified from Ref. [67]). The regions where the splittings become noticeable are marked by red circles.

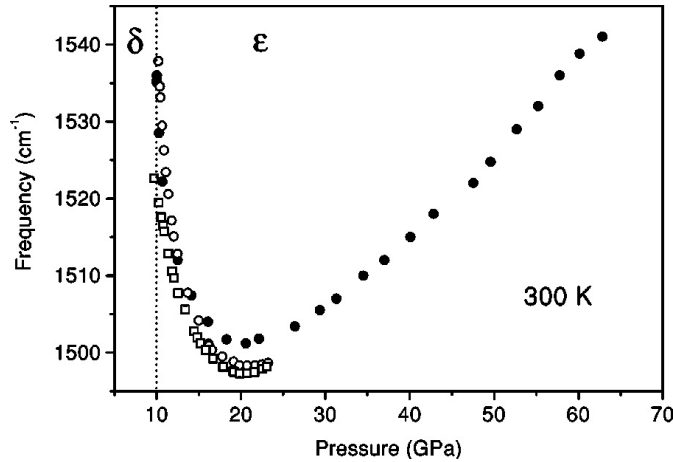


Fig. 53. Pressure dependence of the IR mode in the  $\epsilon$  phase. (From Ref. [65].)

imum displaying by the  $L_2$  libron band between 25 and 35 GPa (Fig. 54). There is another small but nonetheless important experimental evidence shown by the  $O_2$  Raman data [67] that 20 GPa marks a delicate but definite breaking point with a lower rate of decrease of the mode frequency with decreasing pressure (see Fig. 55). The point 20 GPa separates the regions with the different rates of Raman frequency change with pressure. Figure 55 shows the experimental data on the pressure dependence of the frequencies of Raman and IR vi-

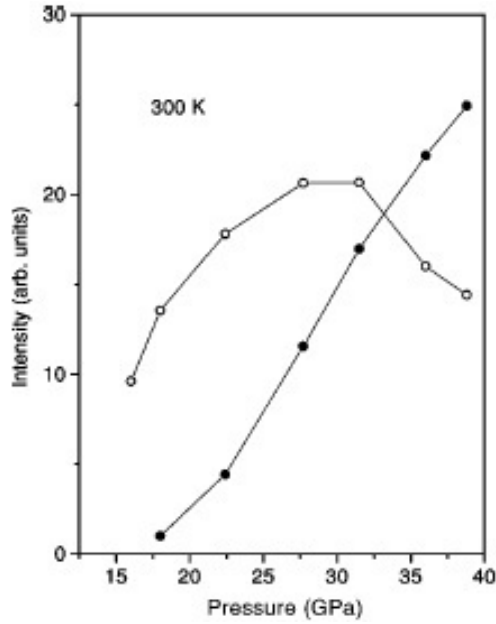


Fig. 54. Integrated intensities of the Raman vibron and  $L_2$  modes, empty and full circles, respectively, (From Ref. [65].)

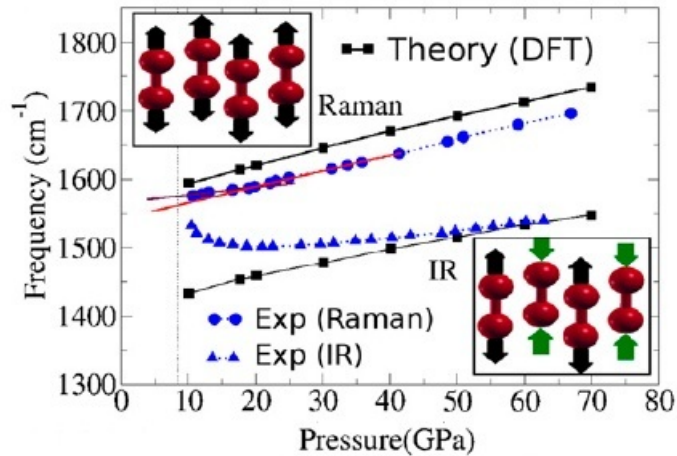


Fig. 55. (color online). Experimental and theoretical pressure dependence of the Raman and IR frequencies in the  $O_2$  vibron region. Theory: solid lines with squares (Ref. [38]). Experiment: Raman data from Ref. [67] - dashed lines with filled circles; IR data from Ref. [63] - dashed lines with filled triangles. Solid red lines are a guide to an eye for a better appreciation of the change of slope around 20 GPa. Displacement patterns for the IR and Raman modes are shown in the lower right inset and upper left inset, respectively. (From Ref. [45].)

bron modes in comparison with theory Ref. [38]. Thus, the pressure behavior of both modes may indicate a possible switch of individual  $O_2$  molecules from  $S = 0$  to  $S = 1$  upon decreasing pressure near 20 GPa. In particular, the frequency gap (see Fig. 56) between the IR mode, where nearest neighbor  $O_2$  vibrate out of phase, and the Raman mode where they vibrate in phase is proportional to the IR effective charge,

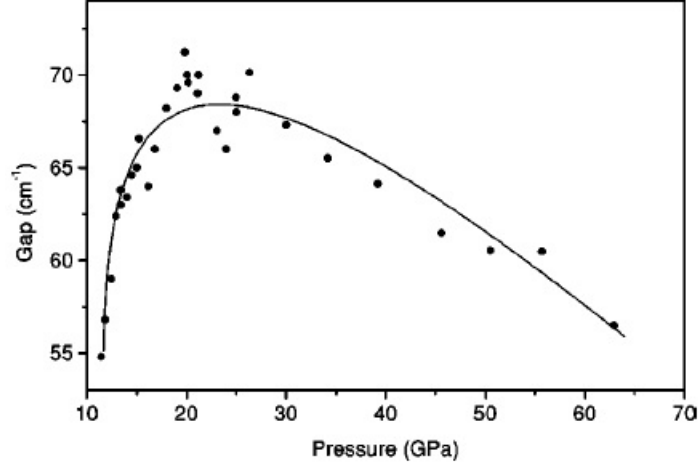


Fig. 56. The evolution with pressure of the gap between the IR and Raman density of states. The solid line is an eye guide. (From Ref. [65].)

connected with electron current between an instantaneously extended molecule (which attracts electrons) and a neighboring compressed one (which expels them) in the IR mode. This electron current is absent in the Raman mode, where neighboring molecules vibrate in phase. If the molecules have spin and correlations are strong, the electron hopping is reduced and the current magnitude, proportional to the IR effective charge, must drop compared with the nonmagnetic band state. Thus, the onset of molecular spin upon decreasing pressure should be accompanied by a collapse of the IR intensity and of the IR- Raman splitting, as is indeed observed in experiment.

### 6.6.2 Theoretical studies of the magnetic properties of the $\epsilon$ phase

Before proceeding further let us consider what could be obtained in standard DFT calculations ignoring a possible role of spin in properties of the  $\epsilon$  phase. Figure 57 shows results of such calculations which were performed in Ref. [46] using DFT with various GGA and different hybrid functionals. Figure 57(Left) shows the pressure evolution of the IR active vibron mode and Fig. 57(Right) shows the pressure evolution of the  $L_2$  libron mode obtained for all the different functionals considered by the authors. These results are compared with experimental data from Ref. [65] and theoretical calculations from Ref. [45]. As can be seen, the standard DFT approaches failed to reproduce the nonmonotonic pressure behavior of IR vibron mode and fast drop of the  $L_2$  mode obtained experimentally and theoretically in

the approach where the magnetic character of the oxygen molecules is keeping inside the low-pressure range 8 - 20 GPa.

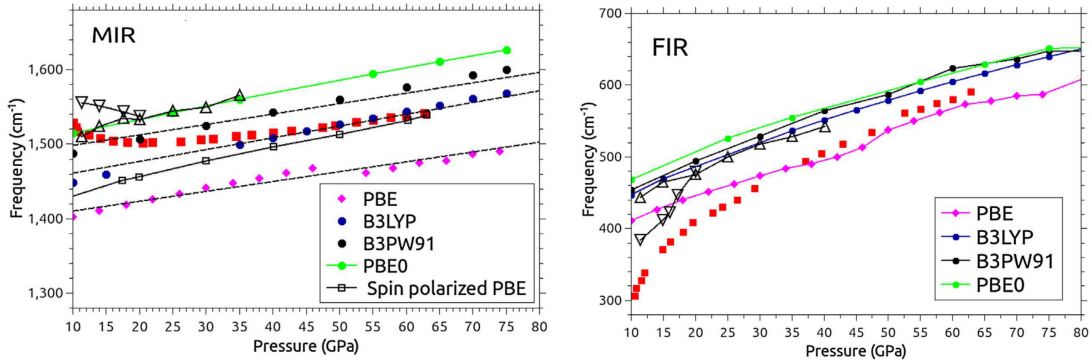


Fig. 57. (color online). Standard DFT calculations - GGA and various hybrid functionals (PBE, B3LYP, B3PW91, PBE0) in comparison with experimental data from Ref. [65] (red squares) and PBE+ $U$  theoretical results [45] (up triangles - non-magnetic calculations and down triangles - antiferromagnetic calculations). Left: Infrared vibron mode, right: Far Infrared libron mode. (From Ref. [46].)

To explain the difference in properties of the  $\epsilon$  phase in the pressure ranges 8–20 GPa and under higher pressures, Crespo et al. [45] proposed the model of the  $\epsilon$  phase in which  $O_2$  molecules either possess the individual spin and form an antiferromagnetic phase or form bonded quartets, leading to a nonmagnetic ground state. The implementation of this model was realized in a DFT +  $U$ , a beyond GGA DFT approach, which have been developed [120] to describe the Mott-Hubbard insulators. The inclusion of a Hubbard  $U$  energy term for the oxygen  $p$ -states had to provide the cancellation of self-interactions present in the simple GGA DFT. The selection of  $U = 1$  eV had to ensure the correct value of the transition pressure (20 GPa) that would fit reasonably the experimental Raman and IR findings described above. The optimized structure had  $O_2$  molecules forming quartets in each plane, quite close to the experimental ones.

The results of the DFT +  $U$  calculations of the enthalpy difference between the non-magnetic and the antiferromagnetic states are shown in Fig. 58. An antiferromagnet (AF) state prevails below 20 GPa, as shown by the enthalpy difference of Fig. 58 between the nonmagnetic (NM) and the AF state, where the molecules are simultaneously quartet distorted and antiferromagnetically spin polarized. This low-pressure "resurgence" of the molecular spin introduces an unrealistic AF static long-range order, which is absent in experiment [21], but

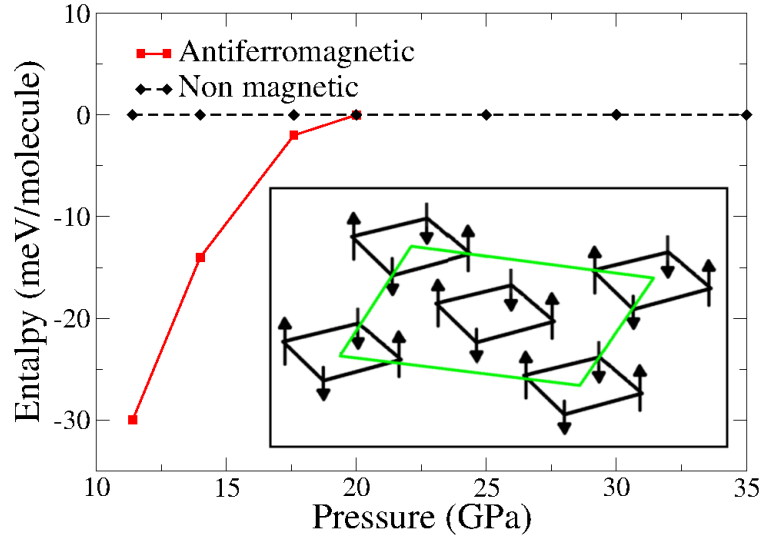


Fig. 58. (color online). Enthalpy difference calculated by DFT+ $U$  between nonmagnetic and antiferromagnetic states in  $\epsilon$ -O<sub>2</sub>. (Inset) Antiferromagnetic configuration inside the (O<sub>2</sub>)<sub>4</sub> quartets. (From Ref. [45].)

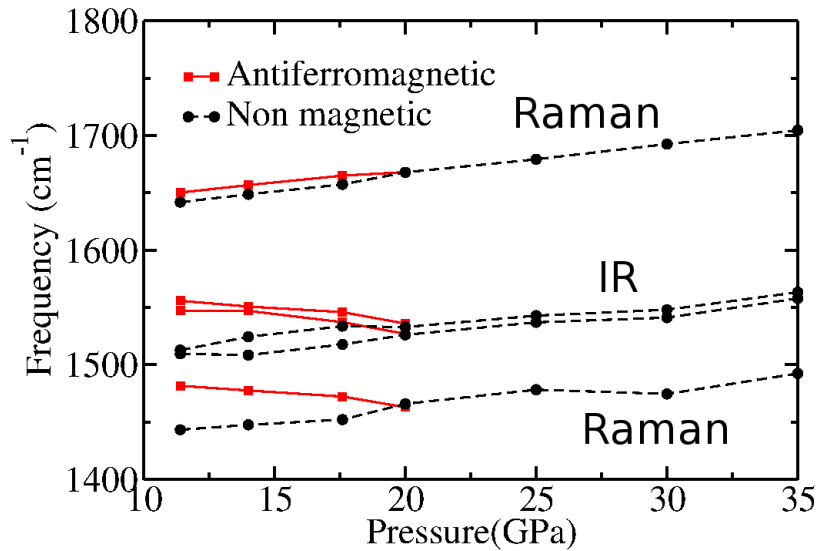


Fig. 59. (color online). Calculated Raman and IR modes for the nonmagnetic (black points) and the antiferromagnetic configurations (red points). Dashed line with circles: Raman mode data. Dashed line with triangles: IR mode data from Ref. [45]. From Ref. [45].

this artificial mean field symmetry breaking is removed by quantum fluctuations. Taking this into consideration and assuming that the mean field theory behind the DFT formulation yields a reasonable total energy, the authors using first-principles calculations obtained the change in the spectroscopic properties of  $\epsilon$ -O<sub>2</sub>, brought about by the instantaneous presence of the molecular spin in the range of interest.

Using this DFT+ $U$  approach Crespo et al. [45], calculated the vibra-

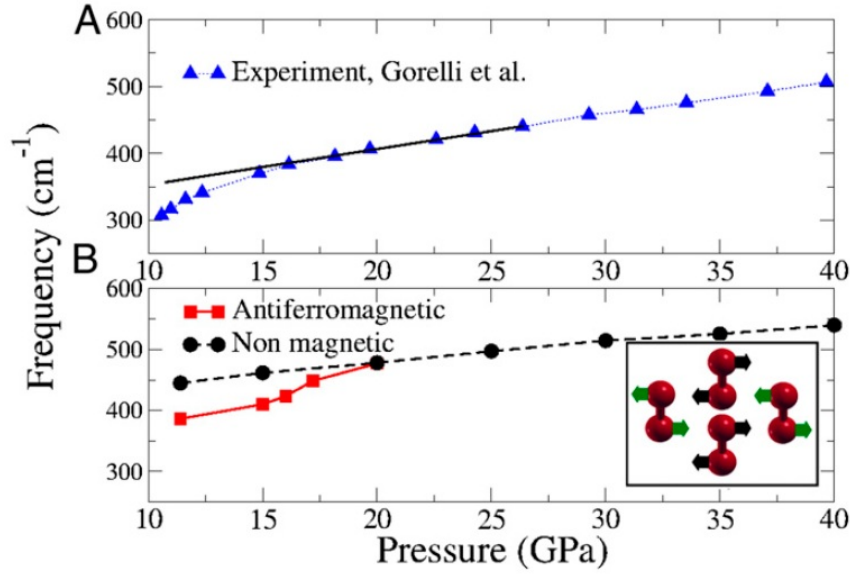


Fig. 60. (color online). Frequency of the far-IR vibrational mode as a function of pressure. Top, experimental data from Ref. [63]. Bottom, calculations using the nonmagnetic and the antiferromagnetic configurations from Ref. [45].

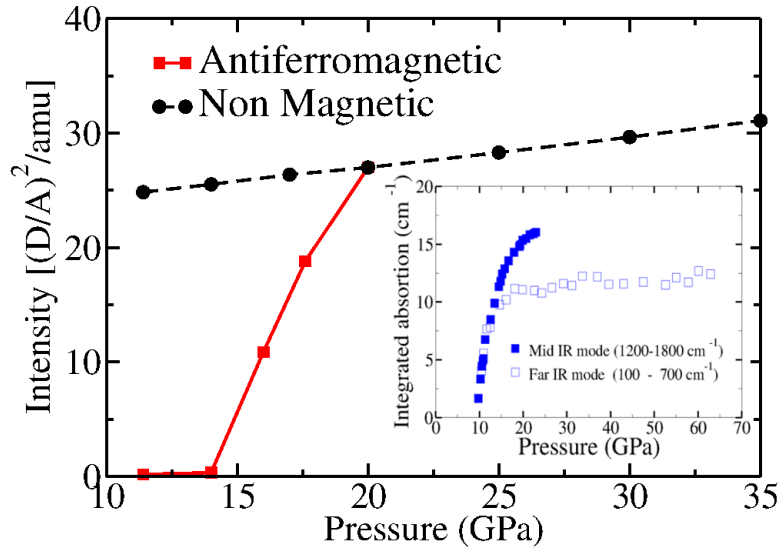


Fig. 61. (color online). Theoretical intensities for mid-IR modes ( $1,500\text{--}1,600\text{ cm}^{-1}$ ) of both nonmagnetic and antiferromagnetic configurations from Ref. [45]. Inset: Experimental IR intensities of the mid-IR mode ( $1,200\text{--}1,800\text{ cm}^{-1}$ ); open squares, far IR mode ( $200\text{--}600\text{ cm}^{-1}$ ) intensities from Ref. [33].

tional spectra of both the nonmagnetic and magnetic states of  $\epsilon\text{-O}_2$ . As shown in Fig. 59, the onset of spin breaks the monotonic drop of both Raman and IR mode frequencies with decreasing pressure, which was predicted for the nonmagnetic state in Ref. [38] but which did not agree with experiment below 20 GPa. Comparison of Fig. 59 with Fig. 55 shows a better agreement, confirming that both the nonmonotonic rise of the IR mode and the slight stiffening of the Raman mode are

spin related.

In Fig. 60, the calculated evolution of the main far infrared vibrational mode (see Fig. 55, Bottom) is shown to drop below 20 GPa in agreement with experimental data (see Fig. 55, Top). This evolution of both high- and low-frequency IR modes upon lowering pressure below 20 GPa goes together with a corresponding change, in fact a decrease, of the mode effective charge. Figure 61 shows that the dramatic drop of the IR intensity observed in this regime (see Fig. 61, Inset), is also well accounted for by the onset of the molecular spin.

The theoretically obtained pressure behavior of Raman and IR modes [45,38] (Figs. 59, 60) is in qualitative agreement with the experimental data shown in Figs. 59, 55. According to the interpretation proposed in Ref. [45], the experimental results of the optical IR and Raman studies [7,65,119,67] (Figs. (52, 53, 54, 55, 60) indicate that the  $\epsilon$ -O<sub>2</sub> region of the phase diagram contains two different phases. The higher-pressure phase exists in the pressure range 20 - 96 GPa. In this phase,  $\epsilon_0$ -O<sub>2</sub>, there is no molecular spin, and the physical properties, including lattice vibrations, can be well described in the framework of the band insulator model, the gap in the spectrum of which arises due to the distortion of the molecular Peierls quartet. The second phase,  $\epsilon_1$ -O<sub>2</sub>, the lower pressure phase, exists between 8 and 20 GPa. This phase exhibits the molecular spin, indicating the existence of strong spin

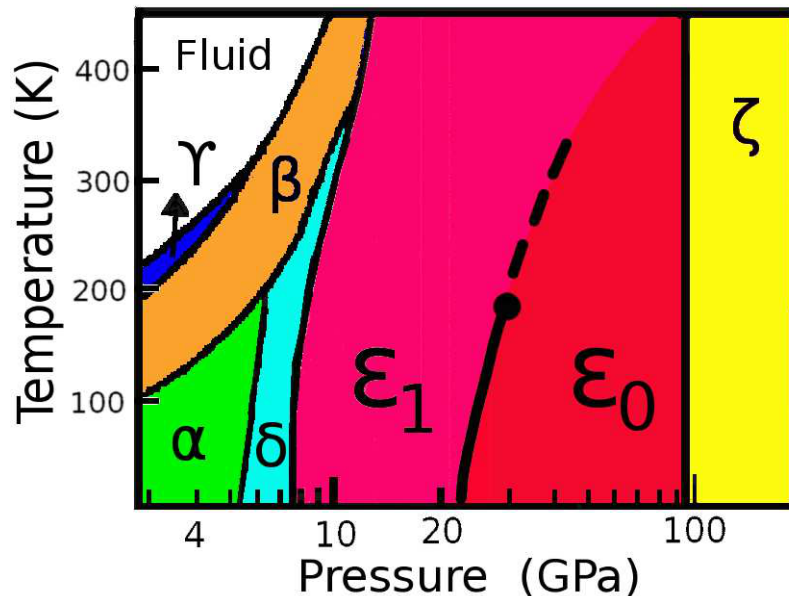


Fig. 62. (color online). Phase diagram of oxygen proposed in Ref. [45]

correlations associated with the distortions of the molecular quartet. The long-range order of the Néel type, similar to that existing in the  $\alpha$  and  $\delta$  phases, is absent in the  $\epsilon_1$ -O<sub>2</sub> phase, as follows from the neutron diffraction data by Goncharenko [21]; however there exists a correlated spin-1 liquid state. The phases  $\epsilon_0$ -O<sub>2</sub> and  $\epsilon_1$ -O<sub>2</sub> are separated by a phase separation line, which starts at around 20 GPa and ends due to the identical symmetry of the phases at a critical point. According to the estimates of Ref. [45], the critical point lies in the vicinity of the  $P - T$  point around 30 GPa, 200 K. The estimated phase diagram has to have the form shown in Fig. 62. As in the case of the gas-liquid critical point, there should exist two different paths connecting the points belonging to the different phases at the phase diagram: the one crossing the phase separation line and a continuous one around the critical point. The attempts to find the critical point experimentally up to now failed [121].

For the experimental investigation of the paramagnetic state of the spin-1 liquid phase,  $\epsilon_1$ , the most accessible magnetic characteristic is the magnetic susceptibility. Magnetic susceptibility measurements of solid oxygen under pressure have recently been conducted in Japan [44] (see Subsection 6.3). The static magnetic susceptibility of solid oxygen at high pressures has been investigated as a function of temperature up to a pressure of 3.3 GPa using a SQUID magnetometer. The pressure was produced using a tiny diamond anvil placed inside the magnetometer. It is realistic to expect that the pressure range of the  $\epsilon_1$  O<sub>2</sub> phase will soon be accessible either for the magnetic susceptibility or for neutron measurements.

The results of the first-principles calculations showed that the resurgence of molecular spin below 20 GPa can explain observed O<sub>2</sub> vibrational anomalies. However, the mean-field long-range AF order obtained by DFT disagree with the established experimentally [21] lack of the long-range spin order. A state where molecular spins are present without  $T = 0$  long-range order would constitute a kind of spin-1 liquid. Crespo et al. extended the picture proposed by Gomonay and Loktev [31] and more recently by Bartolomei et al. [41] consisting of an overall singlet state of an isolated quartet of  $S = 1$  molecules. The quantum mechanical competition between AF long-range order and an overall singlet state should take place in the whole range of ex-

istence of the  $\epsilon_1$ -O<sub>2</sub> phase. For understanding of the magnetic state below 20 GPa, the effective Heisenberg exchange couplings among O<sub>2</sub> molecules were estimated taking into account the interaction between the first, second, third, and fourth neighbors (see Fig. 63, Left). with  $J_1, J_2, J_3$ , and  $J_4$ , the exchange values between the first, second, third, and fourth neighbors. To obtain these parameters the authors carried out constrained spin polarized DFT+ $U$  calculations, based on the experimental structure at  $P = 11.4$  GPa and a variety of six different AF configurations. After parametrization the following estimates were obtained:  $J_1 = 1370 \text{ cm}^{-1}$ ,  $J_2 = 286.3 \text{ cm}^{-1}$ ,  $J_3 = 84.7 \text{ cm}^{-1}$ ,  $J_4 = 116.1 \text{ cm}^{-1}$ . Close values follow from the phenomenological potential proposed for the distance dependence of the exchange constant  $J(R)$  by Helmy et al. in Refs. [122,123].

A simplified system used in the calculations is presented in Fig. (63, Right) as a 2D square lattice model made of plaquettes (quartets) of  $S = 1$  Heisenberg sites. Each site, representing an O<sub>2</sub> molecule, is AF coupled to nearest neighbors within the same plaquette by AF exchange couplings  $J_1 > 0$ , and to nearest neighbors in the next plaquettes by  $J_2 < J_1$ . Two different states compete: the Neel AF configuration, as obtained by DFT and which breaks spin SU(2) symmetry, and a singlet, NM state that is akin to a collection of independent

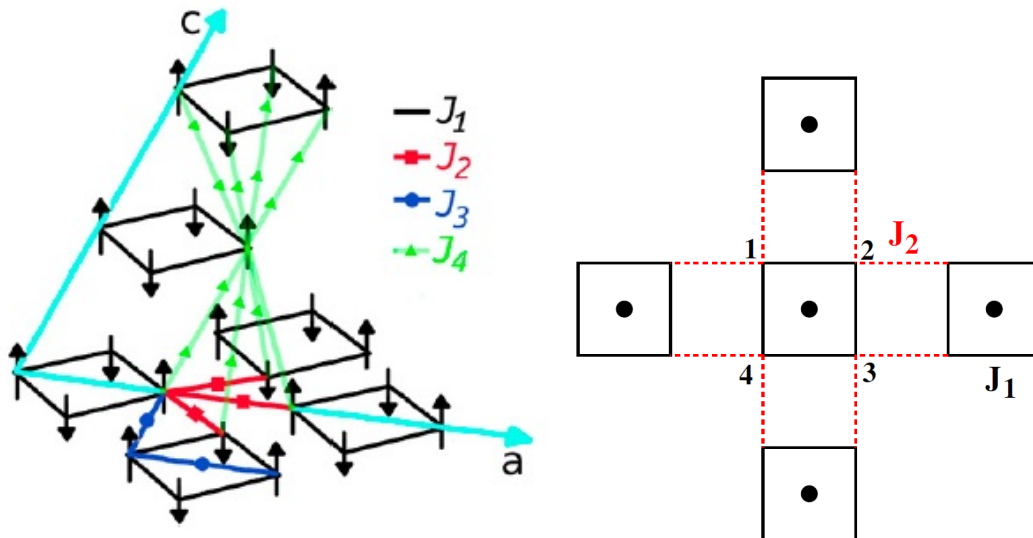


Fig. 63. (color online). Left: long-range antiferromagnetic order and interactions between the first four neighbors  $J_1$  (inside the quartet),  $J_2$  with the two or three nearest quartets,  $J_3$  third nearest neighbors in the plane, and  $J_4$  with molecules located in the planes above and below. Right: simplified 2D Heisenberg model. (From Ref. [45].)

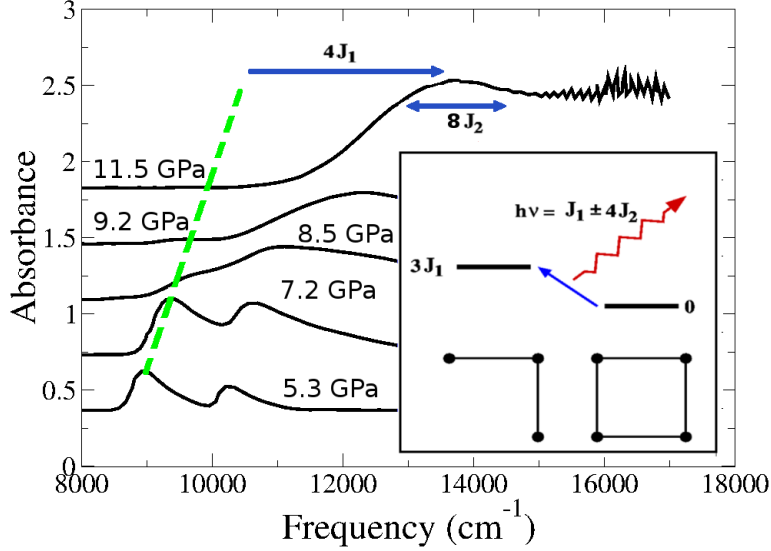


Fig. 64. (color online). Explanation of the blue shift at the  $\delta - \epsilon$  transition. Solid lines are data of the IR absorption from Ref. [66], dashed green line is a linear extrapolation of the peak corresponding to  ${}^3\Sigma_g^- \rightarrow {}^1\Delta_g$  process at 11.5 GPa, and the blue arrow represents the blue shift of  $4J_1$  with a  $8J_2$  broadening represented by the double blue arrow. (Inset) Initial plaquette and final  $S = 1$  trimer state; an itinerant spin 1 excitation is emitted by spin conservation (red wavy arrow), which costs an additional energy of  $h\nu \simeq 4(J_1 \pm J_2)$ .

plaquettes, each in its singlet ground state. The singlet ground state of an isolated plaquette of energy  $E_0 = -6J_1$  is obtained by coupling second neighbor sites 1 and 3 to  $S_{13} = S_1 + S_3 = 2$ , coupling sites 2 and 4 to  $S_{24} = S_2 + S_4 = 2$ , and then coupling  $S_{13}$  and  $S_{24}$  to a total singlet  $S = S_{13} + S_{24} = 0$ . The energy per site of an independent collection of plaquettes thus is (note that the number of plaquettes  $N_{\square}$  is one quarter the number of sites)  $E_{\text{Neel}} = -\frac{3}{2}J_1$ . By comparison, the classical energy per site of the Neel AF configuration is  $E_{\text{Neel}}^{\text{classical}} = -J_1 - J_2$ . Therefore, for  $J_2 < J_1/2$ , the nonmagnetic collection of independent plaquettes will be lower in energy than the Neel configuration. From the obtained estimates it follows that the actual ground state is a collection of independent nonmagnetic plaquettes as proposed in ref. [31]. If one goes further and includes quantum fluctuations the above relation between  $J_1$  and  $J_2$  change to  $J_2 < J_1/4$  imposing a bigger difference between this two parameters. Nevertheless the estimated values of the exchange couplings satisfy also this inequality, confirming the stability of an overall singlet state, even once quantum fluctuations are included. As a conclusion of this results the authors propose a lattice of plaquettes each made of four AF correlated  $S = 1$  sites, with weaker but nonzero interplaquette correlations as their best model for  $\epsilon$ -O<sub>2</sub> phase below 20 GPa.

The occurrence of a magnetic state in  $\epsilon$ -O<sub>2</sub> is consistent in principle also with optical absorption experiments [65]. The lowest optical excitation in  $\epsilon$ -O<sub>2</sub> is in fact dominated by the intramolecular triplet-to-singlet transition, and is therefore controlled by the magnetic state of the molecule. A further important result in support of the model developed in Ref. [45] is the explanation of the near-infrared spectroscopy across the  $\delta$ - $\epsilon$  transition published in 2001 [66] (see also Ref. [7], Secs. 5.2.7 and 5.3) but found its explanation only in the model developed in Ref. [45]. As shown in Fig. 64 when the  $\epsilon$  phase sets in above 8 GPa, the  ${}^3\Sigma_g^- \rightarrow {}^1\Delta_g$  is abruptly blue shifted to  $\approx 12.400 \text{ cm}^{-1}$  and very considerably broadened, to the extent that its vibrational satellites are not anymore distinguishable. That optical observation was explained as follows. In the  $S = 1$  Heisenberg model representation, the  ${}^3\Sigma_g^- \rightarrow {}^1\Delta_g$  excitation of a single molecule amounts to annihilating a spin 1 site in a plaquette, leaving a vacancy in its place. Then we should expect optical absorption at a frequency equal to the  $E_{{}^3\Sigma_g^- \rightarrow {}^1\Delta_g}$  molecular excitation energy plus the energy cost of the molecular vacancy. In the O<sub>2</sub> quartet singlet state, a vacancy costs roughly the energy difference between the ground state of the three surviving O<sub>2</sub> molecules and the initial four-molecule state. This difference is readily found to be  $3J_1$ . Moreover, since the three-molecule state has  $S = 1$ , while the initial four-molecule state was a singlet, an itinerant spin-1 excitation must be created in addition to the vacancy, costing an additional energy  $\omega \in [J_1 - 4J_2, J_1 + 4J_2]$  (see Fig. 64, Inset). Respectively, the absorption line undergoes at the  $\delta$ - $\epsilon$  transition a blue shift of  $\lesssim 4(J_1 - J_2)$  with a large broadening  $\approx 8J_2$  due to interplaquette exchange. With the calculated exchange values at 11.4 GPa, that means  $0.54 \text{ eV} = 4.355 \text{ cm}^{-1}$  and  $0.28 \text{ eV} = 2.258 \text{ cm}^{-1}$ , respectively, values that are reasonably close to the experimental ones [65] (see Fig. 64).

### 6.6.3 Magnetic properties of epsilon phase: concluding remarks

Recently neutron studies were extended to the low-pressure range of the  $\epsilon$  phase (Fig. 65) and no magnetic reflexes were found. Numerous anomalous spectroscopic features displaying in the lower-pressure part of the  $\epsilon$ -O<sub>2</sub> region of the oxygen phase diagram and the failure of theory to describe these anomalies disregarding molecular spin indicate

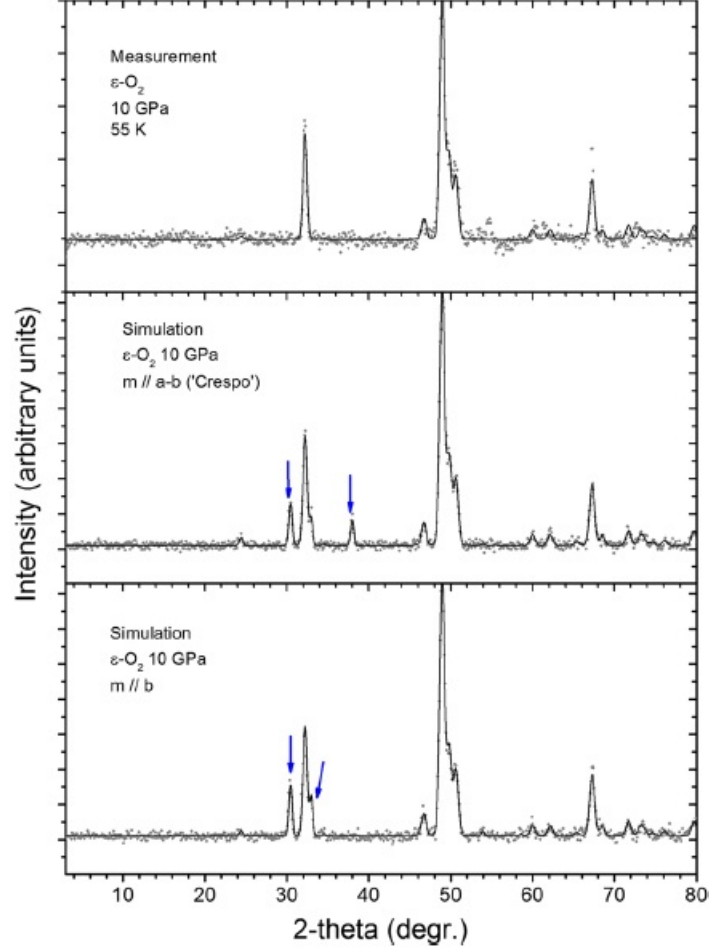


Fig. 65. (color online). Neutron diffraction patterns of  $\epsilon$ -O<sub>2</sub>. Upper panel: measured; the line is a Rietveld fit through the data (dots) assuming no magnetic long-range order. Middle panel: simulated, assuming long-range magnetic order and spin alignment according to Crespo et al. [45](see Fig. 63 Left). Lower panel: same as above, but with spins aligned along **b**-axis. Arrows indicated strongest magnetic Bragg reflections. (From Ref. [115].)

that there is no single broad  $\epsilon$ -O<sub>2</sub> phase from 8 to 96 GPa but instead we have two phases  $\epsilon_1$ -O<sub>2</sub> and  $\epsilon_0$ -O<sub>2</sub> – the former a local singlet spin-1 liquid, and the latter a regular, Peierls band insulator – separated by a first-order phase transition near 20 GPa. The predicted phase line terminates in a critical point, which supposedly lies near 30 GPa and 200 K. The high-temperature region below 30 GPa must be characterized by thermally fluctuating  $S = 1$  spins, whose presence should be directly detectable by magnetic susceptibility measurements in the 8- to 30-GPa pressure range. At low temperatures, the wealth of low-energy spin excitations present in  $\epsilon_1$ -O<sub>2</sub> but absent in  $\epsilon_0$ -O<sub>2</sub> should give rise to very new energy dissipation channels and processes in the former phase.

## 7 High-pressure high-temperature melting line

Investigations of the melting curves play an important role in condensed-state physics. In particular, they help to understand the nature of the fundamental difference between fluid and crystal states at a microscopic level.

Commonly used methods for identifying the beginning of melting include an analysis of Bragg reflections in x-ray diffraction, appearance of jumps or changes in the slope of Raman vibron modes as a function of pressure and temperature, and visual observation of fluid flow or laser spackle. Merits and limitations of the various methods were analyzed by Benedetti et al. [37].

Among the listed above methods, only the x-ray diffraction provides direct information on the physical state of the sample. But even this method is not free from drawbacks, in particular, the disappearance of the Bragg reflections may be caused by other physical phenomena than melting such as crystallite reorientation or solid-solid phase transformations. The direct visual and speckle methods are subjective; besides they cannot be applied when at high temperature the fluorescence emission of fluid is very strong. The natural conclusion drawn by Benedetti et al. from this analysis was that simultaneously monitoring both structural and spectral properties is superior to any single method for identifying the onset of melting.

The melting line of oxygen had already been studied up to about 650 K (16.7 GPa) [68,124] well before the beginning of the period of time covered by this review. The first high-temperature diamond-anvil-cell Raman study of solid oxygen were performed as early as in 1982 year by Yagi, Hirsh, and Holzapfel who managed to measure the melting line and the  $\beta - \epsilon$  phase boundary up to 500 K (13 GPa) [94]. The high  $P - T$  melting line up to 460 K was determined from shifts in the Raman vibron [68]; at higher temperatures the melting was detected only by visual observation under microscope. On the basis of these observations the existence of a new triple point was found which was interpreted as the fluid- $\beta$ - $\epsilon$  triple point. The visual technique was especially effective for this triple point because the three coexisting phases have quite different colors.

The appearance of the chemical reactions between oxygen and the material of the gasket and the diamond anvils, which led to the breaking down of the container, prevented extending of these studies to higher temperatures.

The high  $P - T$  experiments on hydrogen and nitrogen [125,126] have shown that the use of pure Re as the gasket material and very careful execution of the experiment allow to overcome these problems. In Raman measurements of oxygen Santoro et al. achieved temperatures as high as 1250 K ( $\sim 25$  GPa) [12] and did not observe any chemical reactions. The existence of a new molecular phase (which was called  $\eta$  phase) was found with three triple points in the  $P - T$  domain of the new phase. According to the Raman and x-ray data obtained in this work in the range 16 - 20 GPa there is a steep rise of the melting temperature but this was not confirmed in the subsequent studies [29,14]. Analyzing the reasons of this discrepancy Weck et al.

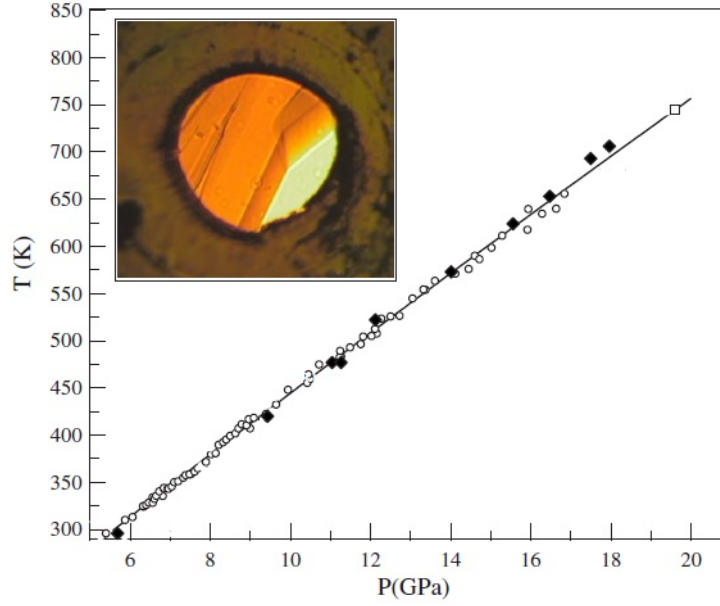


Fig. 66. (color online). Oxygen melting curve. Two sets of measurements are presented. The full line correspond to a least square fit of measurements with the Simon equation. The picture correspond to a solid-fluid equilibrium at  $T = 719$  K and  $P = 18.8$  GPa.(Modified from Ref. [29].)

[29] pointed out that strong pressure variations could arise at melting and the  $P - T$  measurements have to be made when a stable solid-fluid equilibrium is visualized as was the case in their work.

Weck et al. has been measuring the melting curve up to 750 K ( $\sim 20$  GPa) by direct visualization of the solid-fluid equilibrium. Melting can be visually distinguished from the transformation to  $\eta$  oxygen because fluid oxygen is transparent to visible wavelengths at these pressures, whereas  $\eta$  oxygen exhibits visible absorption [19]. To prevent possible chemical reaction between oxygen and rhenium gasket the sample was isolated from the gasket with 10 m $\mu$  thick gold ring - a technique that has been successfully used previously in the measurement of the melting curve of H<sub>2</sub> [127]. The diffusion of oxygen in the diamond anvil which was greatly enhanced above 650 K in the fluid phase near melting pressure above 650 K could be stopped by using Al<sub>2</sub>O<sub>3</sub> coated anvils.

As can be seen, the melting temperature of oxygen is a monotonically increasing function of pressure (Fig. 66). The experimental data were fit to the Simon equation

$$T = [(P + 2.223) / 0.0119]^{1/1.1374} \quad (2)$$

or in a canonical form [128]

$$P = 0.0119 T^{1.1374} - 2.223. \quad (3)$$

( $P$  in GPa,  $T$  in K) with the deviation within the experimental uncertainty ( $(T_{\text{exp.}} - T_{\text{calc.}}) / T_{\text{exp.}} < 2\%$ ). Up to 620 K, the melting curve is in excellent agreement

with the measurements by Yen et al. [68] and Santoro et al. [12] but in contrast with Santoro et al. [12] no sharp increase of the melting curve was detected above 620 K.

This conclusion was confirmed by Goncharov et al. [14] who extended measurements of the oxygen melting line up to 60 GPa, 1750 K (Fig. 27) with the x-ray diffraction and Raman spectroscopy by using resistively- and laser-heated diamond anvil cells [14]. In the overlapped regions the data of both studies agree well. In agreement with Weck et al. [29], they found that the melting curve increases monotonically up to the maximum pressures studied ( $\sim 60$  GPa). A strong optical emission of oxygen when illuminated by near IR radiation precluded extensive laser heating studies below 44 GPa. But at higher pressure this emission was much weaker allowing Raman and spectro-radiometric measurements.

The experimental data by Goncharov et al. [14] were fit to the Simon equation

$$T = \left[ \frac{1}{4.71 \cdot 10^{-3}} (P + 1.07) \right]^{1/1.27} \quad (4)$$

or in a canonical form [128]

$$P = 4.71 \cdot 10^{-3} T^{1.27} - 1.07. \quad (5)$$

( $P$  in GPa,  $T$  in K).

The extension of the melting curve up to 25 GPa (Fig. 27) was obtained in the Raman resistive-heating measurements [14]. At melting, the low-frequency peaks of  $\epsilon$  oxygen disappear, and the vibron frequency increases [12,29] (Fig. 67). In a relatively narrow temperature range a new broad Raman vibron peak appears; it can be observed simultaneously (at 833 K) with the vibron of  $\epsilon$  oxygen (which disappears on the further temperature increase). At melting, the vibron band of  $\epsilon$  oxygen experiences a broadening and a positive frequency shift, unlike at the  $\epsilon$ - $\eta$  transition where no essential broadening is reported [19]. The melting transition is accompanied by a pressure drop. In the fluid phase, oxygen becomes totally transparent in the visible spectral range unlike the case of  $\eta$  oxygen, which has a mottled appearance [19]. The Raman frequency of the vibron in  $\eta$  oxygen is slightly lower than that of fluid oxygen [12]. The resistive heating experiments of Goncharov et al. [14] confirm the results of Santoro et al. [12] in that  $\eta$  oxygen melts directly above 20 GPa (Fig. 67), though at higher melting temperature (Fig. 27). The resistive heating melting data [14] agree with visual data of Weck et al. [29] over the  $P - T$  range of overlap of the two data sets.

Above 44 GPa, the x-ray diffraction experiments [14] revealed melting as manifested by the appearance of a broad diffuse band and a reduction in intensity of the Bragg reflections. The corresponding melting line lies very close to the extension of the previously determined (to 20 GPa) melting line [29] and agrees within the error bars with the results of the laser heating experiments reported in Ref. [37].

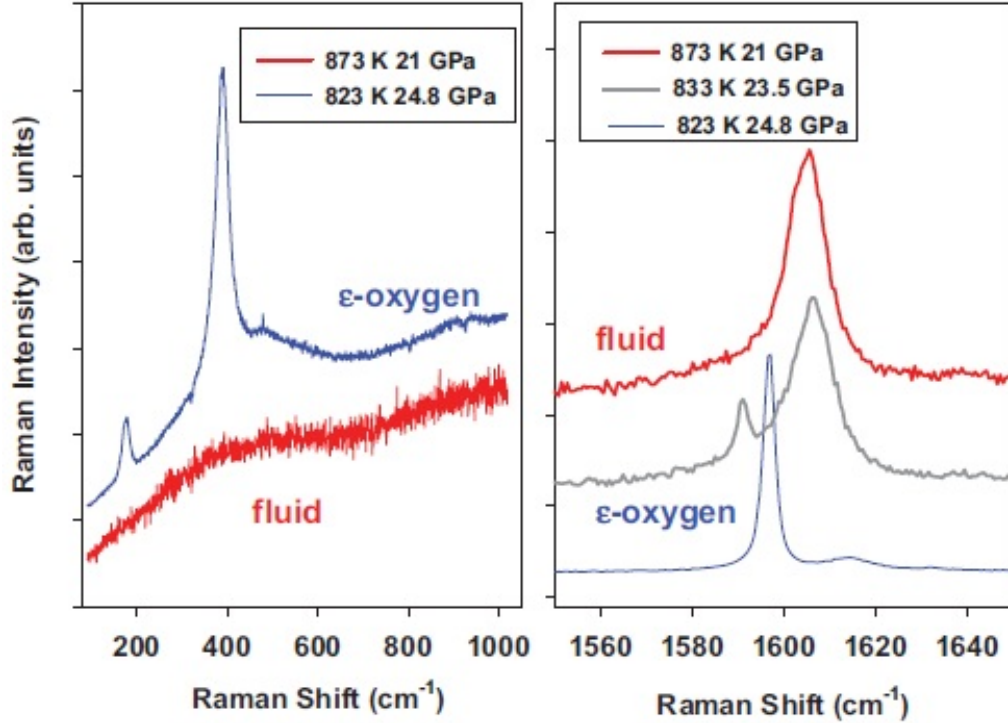


Fig. 67. (color online). Raman spectra of resistively heated oxygen across the melting transition. Left and right panels show spectra in the spectral ranges corresponding to lattice and intramolecular (vibron) modes. (From Ref. [14].)

To illustrate the importance of using a number of complementary techniques for registration of the onset of melting Benedetti et al. [37] investigated melting of  $O_2$  using the concurrence of four phenomena: (1) the loss of x-ray diffraction of Bragg peaks, (2) the onset of sample motion evidenced by x-ray diffraction, (3) the onset of sample motion evidenced by visual inspection, and (4) the change in optical properties. Though the samples were laser heated at four different pressures, the onset of melting have been confidently identified only at two pressures: at 55 GPa, where all four criteria were we observed at  $1850 \pm 450$  K, and at 47 GPa, where three of the four criteria were observed at  $1500 \pm 200$  K. Although at 47 GPa the authors did not observe complete loss of Bragg peaks (supposedly due to longer x-ray diffraction exposures) they observed an optical transition nearly identical to that at 55 GPa concurrent with both visible and x-ray diffraction evidence for the onset of motion. These two melting points are consistent in the limits of the error bars with both Simon equations (Eq. 4) determined for the oxygen melting curve by Goncharov et al. [14] and with extrapolation of Simon equation Eq. (2) determined by Weck et al. for pressures from 5.4 to 20 GPa [29].

As was mentioned above, At pressures over  $\sim 12$  GPa the  $\epsilon$  phase is separated from the liquid phase by the  $\beta$  phase (see phase diagram Fig. 1). The width of the region occupied by the  $\beta$  phase decreases with rising pressures - the  $\beta$  phase is gradually "expelled" by the liquid and  $\epsilon$  phases. Yen and Nicol in their Raman and visual study of the melting line of oxygen [68] found the point of the disappearance of the  $\beta$  phase which they thought is the triple point fluid- $\beta$ - $\epsilon$ . According to their data the  $P - T$  coordinate of this point are 16.3 GPa, 645 K. Santoro et al. found that the

$\epsilon$  phase does not melt at this point and actually this is the triple point fluid- $\beta$ - $\eta$ . There are separate observations referred to this region. Santoro et al. [12] located the triple points  $\beta - \epsilon - \eta$  ( $T_{\beta\epsilon\eta} = 540 \pm 20$  K ,  $P_{\beta\epsilon\eta} = 15.7 \pm 0.2$  GPa) and liquid- $\beta - \eta$  ( $T_{l\beta\eta} = 624 \pm 20$  K ,  $P_{l\beta\eta} = 15.6 \pm 0.2$  GPa). The observation of single-phase  $\eta$  phase samples at 15.7 GPa and 575 K suggests that the  $\beta - \eta$  phase boundary of Santoro et al. [12] is at slightly too high a pressure. The observation of a mixed  $\epsilon$ - $\eta$  sample at 18 GPa and 675 K [19] locates the phase boundary between these phases at or very near to this point and shows that there is no direct melting of the  $\epsilon$  phase at this pressure. The absence of any  $\beta$  phase at the 16.7 GPa and 645 K transition found by Yen and Nicol [68] can then also be explained by a transition from the liquid to the  $\eta$  phase, rather than to the  $\epsilon$  phase. Further detailed spectroscopic studies will be required to determine the exact trajectory of the  $\eta - \epsilon$  phase boundary and to locate the  $\eta - \epsilon$ -liquid triple point if it exists.

## 8 Solid oxygen in ultrahigh magnetic fields

### 8.1 Introductory remarks

Although ultrahigh magnetic fields of a hundred Tesla range are now accessible for experiment, because of technical difficulties only a few studies of solid oxygen in fields up to 50 T were published until recently [107,129,130]. Meier et al. [107] found the spin-flop transition in  $\alpha$  oxygen at  $7.2 \pm 0.2$  T. Beyond the spin-flop field up to approximately 30 T the magnetization curve is almost linear. A marked nonlinearity of the magnetization curve of the  $\alpha$  phase appeared above 30 T but no phase transitions were observed. The magnetization curves of the  $\beta$  and  $\gamma$  phases remained linear up to the highest studied fields.

What makes solid oxygen extremely interesting object for physics of ultrahigh magnetic fields? An analysis of the  $P - T$  phase diagram of solid oxygen indicates the possibility that in addition to the phases that exist in the zero magnetic field, there can exist phases induced by a magnetic field. The strength of the exchange interaction essentially depends on the alignment of  $O_2$  molecules, indicating that the packing structure of solid oxygen is tuned to its magnetic ground state. The low pressure  $\alpha$ ,  $\beta$ , and  $\delta$  phases are realized as a result of a subtle balance between the Van den Waals and magnetic interactions. The competition between them leads to a strong interplay between magnetic, structural, and orientational degrees of freedom of the oxygen molecules. In the rhombohedral  $\beta$  phase,  $O_2$  molecules form a triangular lattice in the basal plane, where the geometrical frustration suppresses the antiferromagnetic long-range order and only a strong short-range magnetic order exists. The geometrical frustration is lifted at approximately 23.9 K (at zero pressure) by the monoclinic lattice deformation in the basal plane, and the  $\beta - \alpha$  phase transition takes place - the high symmetry crystal structure of  $\beta$  oxygen is deformed by the magnetic ordering. Such coupling between the magnetic and structural systems suggests that a sufficiently high external magnetic field could induce

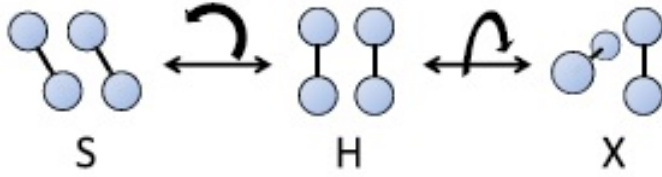


Fig. 68. (color online). The geometrical rearrangement for the O<sub>2</sub>-O<sub>2</sub> dimer, from H geometry (parallel) to S geometry (canted) or X geometry (crossed). The  $\alpha$ ,  $\beta$ , and  $\delta$  phases of solid oxygen are based on the H geometry. (From Ref. [22].)

structural phase transitions.

## 8.2 Magnetization measurements

In 2014 such ultrahigh-field  $\theta$  phase, an eighth phase of solid oxygen, was discovered by Nomura et al. [22] at around 120 T. The mechanism of the  $\alpha - \theta$  phase transition was explained by the authors in analogy with the behavior of an O<sub>2</sub> dimer in a strong magnetic field. The stable arrangement of the O<sub>2</sub> dimer depends on whether the magnetic moments align antiferromagnetically or ferromagnetically. In zero field, the dimer has the rectangular-parallel H geometry corresponding to the maximum  $\pi$  orbital overlapping between the two molecules in the dimer at the given intermolecular distance [131,83,132]. This geometry maximizes the Heisenberg AF interaction. However, when the magnetization of the dimer is saturated by an external magnetic field, AF interaction is no longer favored. The minimal overlap occurs for the crossed X configuration which optimizes the repulsive forces. Thus, the O<sub>2</sub>-O<sub>2</sub> dimer structure can tune the exchange interaction by changing its alignment. Since for the zero-field phases there exists a subtle balance between the VdW and exchange interactions, a high magnetic field can change the packing structure of solid oxygen from that optimizing the AF H geometry to the crossed X or canted S structure (Fig. 68) having smaller AF interaction [133]. The O<sub>2</sub>-O<sub>2</sub> dimer was realized in experiment by using nanoporous coordination polymers [134]. X-ray diffraction measurements at low temperatures revealed that at zero magnetic field the dimer system exactly as solid oxygen has the H geometry. At the same time, the magnetic measurements could not be interpreted based on Heisenberg models and H geometry only. To explain the experimental findings, researchers invoked a scenario in which there are excited states of other geometries, e.g., the S or X type. This scenario indicates that a molecular rearrangement may occur in a magnetic field. It was also found that the thermally excited states lead to deviations from the H geometry at higher temperatures. These combined results, obtained on dimers, led to the anticipation of a field-induced structural phase transition in solid O<sub>2</sub>.

The new ultrahigh magnetic field  $\theta$  phase and the  $\alpha - \theta$  and  $\beta - \theta$  phase transitions were documented using two different methods [22,23]. In the first, the magnetization as a function of magnetic field was measured; in the second, the changes in magneto-transmission with magnetic field were registered.

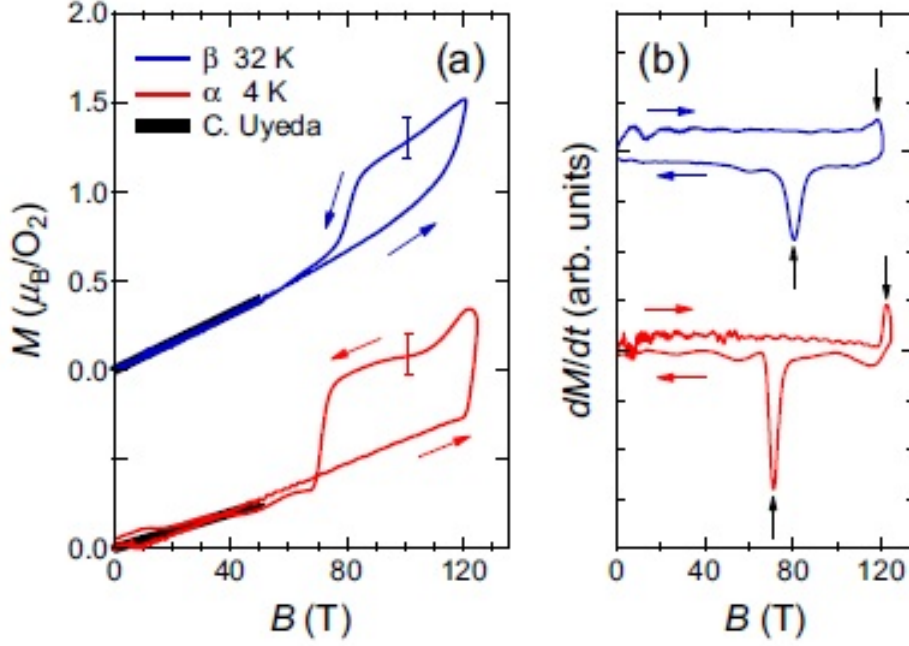


Fig. 69. (color online). (a) The magnetization  $M$  and (b) the  $dM/dt$  curves of solid oxygen.  $B_{\text{Max}} = 124$  T,  $T = 4$  K for  $\alpha$  phase, and  $B_{\text{Max}} = 121$  T,  $T = 32$  K for  $\beta'$  phase. The results of Uyeda et al. [130] are shown by black lines for comparison. The transition fields are determined by the  $dM/dt$  peaks, as shown by the black arrows. (From Ref. [23].)

A single-turn coil (STC) technique was used to generate pulsed magnetic fields. The field was pulsed for approximately  $8 \mu\text{s}$  in a destructive manner. The experimental data on the magnetization  $M$  (in units of  $M_s = 2\mu_B$  per  $\text{O}_2$  molecule) and the time derivative  $dM/dt$  of the  $\alpha$  and  $\beta$  phases are shown in Figs. 69a and 69b [23], respectively. The magnetization curves obtained in the mid-eighties of the last century by the Date group using a nondestructive pulse magnet [130] are shown for comparison by the black solid lines (see also Fig. 92 from Ref. [7]). The magnetization kinks in the up and down sweeps are reproducible, and hence, correspond to intrinsic phenomena identified as the  $\alpha - \theta$  and  $\beta - \theta$  transitions. The transition fields are determined by the  $dM/dt$  peaks, as shown by the black arrows in Fig. 69b. In lower fields the magnetization for the both magnetization curves increases indicating that the  $\alpha - \theta$  and  $\beta - \theta$  transitions in these fields and the sweep speed ranges still do not occur [22]. This finding clearly shows that the field-induced phase  $\alpha - \theta$  and  $\beta - \theta$  transitions take place in ultrahigh magnetic fields greater than 120 T. The pronounced hysteretic behavior suggests that the phase transition is first order.

### 8.3 Magneto-transmission measurements

Another phenomenon which was used to register the magnetic-field induced phase transitions is the change in the light transmission intensity with magnetic field [133,22,23]. The results of the magneto-transmission measurements on the  $\beta - \theta$  phase transition are shown in Fig. 70. The upper panel give the time profile of the pulsed magnetic field ( $B_{\text{Max}} = 141$  T,  $T = 32.5$  K) while the bottom panel shows

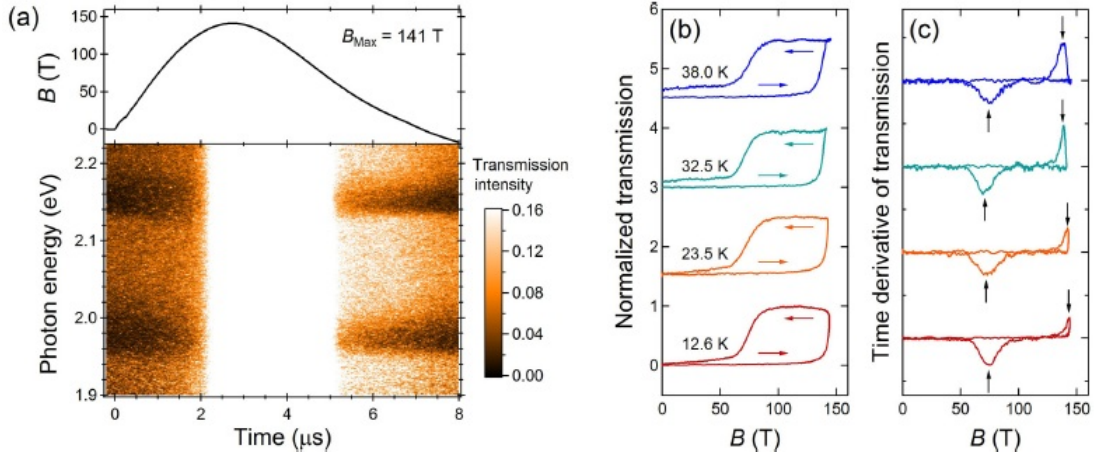


Fig. 70. (color online). (a) Magnetic field dependence of the transmission spectra of the  $\beta$  phase ( $B_{\text{Max}} = 141$  T,  $T = 32.5$  K). (b) Normalized light transmission intensities and (c) their time derivatives at different temperatures. The maximum field strengths are  $143 \pm 3$  T for all curves. (From Ref. [23].)

the relative transmission intensity in the two-dimensional color mapping. The relative transmission,  $I/I_0$ , is represented on a color scale, where  $I$  and  $I_0$  are the intensities of the transmitted light through the sample cell with and without oxygen, respectively. The normalized transmission curves as a function of magnetic field at different temperatures (Fig. 70b) are similar to the magnetization curves (Fig. 69b). Corresponding time derivatives of the transmission are shown in Fig. 70(c). The transmission intensities are normalized so that the difference from minimum to maximum is unity. The transition fields are determined by peaks of the time-derivative signal, as shown by the black arrows. These results are consistent with the magnetization curves shown in Fig. 69. This change in the transmission intensity is considered to be due to the removal of the crystalline anisotropy, which causes light scattering at the domain boundaries and decreases the transmitted light. Therefore, the  $\alpha - \theta$  and  $\beta - \theta$  transitions can also be documented by the change of the light transmission intensity owing to the structural transformations.

Figure 71a shows the waveform of the pulsed magnetic field up to 128 T (upper panel) and the two-dimensional transmission spectra image of  $\alpha$  oxygen at 21.6 K (bottom panel) as a function of time. At zero magnetic field, the transmission is small for the light in the photon energy range 2.15–2.20 eV due to the bimolecular transition of solid oxygen [135–138]. At near the highest magnetic field, 128 T (2.8  $\mu$ s), the transmission of the  $\alpha$  oxygen rises sharply over the whole photon energy range. When the magnetic field decreases, the transmission decreases again at about 60 T. These critical fields are close to those of the phase transition observed in the magnetization measurements; hence, this anomalous optical behavior is likely to be connected with the magnetic phase transition. Figures 71b and 71c show the cross section of the two-dimensional transmission spectra by time and photon energy, respectively. When the field is less than 100 T (i  $\rightarrow$  ii), the shape of the transmission spectrum changes around only 2.14 eV. This peak deformation is caused by the orbital Zeeman effect of the bimolecular absorption [138,9,133]. As the field passes through its maximum (ii  $\rightarrow$  iii), the transmission at all photon energies increases,

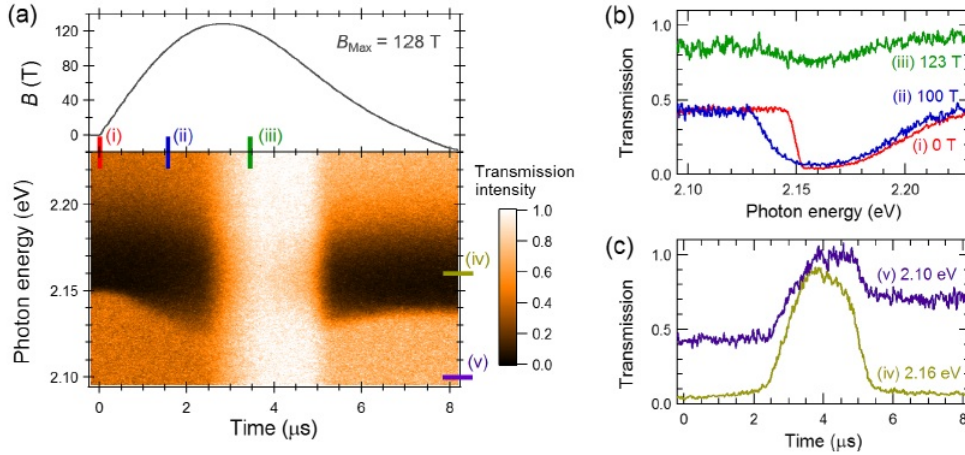


Fig. 71. (color online). (a) Two-dimensional transmission spectra of the solid oxygen  $\alpha$  phase at 21.6 K and the waveform of the pulsed magnetic field up to 128 T are shown as a function of time. The transmission intensity is represented on a color scale. The labels from (i) to (v) show the position of the cross sections in Figs. 71b and 71c. (b) Transmission spectra obtained from the time cross section in Fig. 71a. The magnetic field intensity is shown for each spectrum. (c) Time dependencies of the transmission obtained by the photon energy cross section in Fig. 71a. The photon energy is shown for each spectrum. (From Ref. [22].)

and the bimolecular absorption is considerably diminished. The change in the transmission is clearly shown in cross sections (iv) and (v) in Fig. 71c. At a photon energy of 2.10 eV in cross section (v), the effect of the bimolecular absorption is negligible. In both cross sections (iv) and (v), independent of the existence of the bimolecular absorption, the transmission rapidly increases at  $2.5 \mu\text{s}$  (127 T) and decreases again at  $5.2 \mu\text{s}$  (61 T). The positions almost correspond to the transition field values obtained from the magnetization curve.

The authors proposed two different explanations of the observed change in the light transmission intensity with magnetic field. The abrupt increase in the magnetization (Fig. 69) suggests that the AF long-range order (or the strong short-range order) is disturbed and the spins of  $\text{O}_2$  molecules are forced to align parallel to the magnetic field. This affects the bimolecular absorption: it cannot occur when there are no AF  $\text{O}_2$  pairs [138,9,133,130]. Therefore, in addition to the magnetization jump, the significant suppression of the bimolecular absorption shown in Fig. 71b indicates that the magnetization of the  $\text{O}_2$  molecules is close to the saturation at around 123 T.

The second explanation connects the found phenomenon with a similar changes in transmittance at the temperature induced  $\beta - \gamma$  phase transition in zero magnetic field (Fig. 72). This phenomenon originates from the change in the classical light scattering by the crystal domain boundaries [7]. In the  $\beta$  phase, the transmission is very small because of strong light scattering by the multidomain structure with anisotropic crystal symmetry (rhombohedral). After the transition to the  $\gamma$  phase, the transparency of the crystal strongly increases. The light scattering significantly reduces since the  $\gamma$  phase has an isotropic cubic structure and isotropic optical

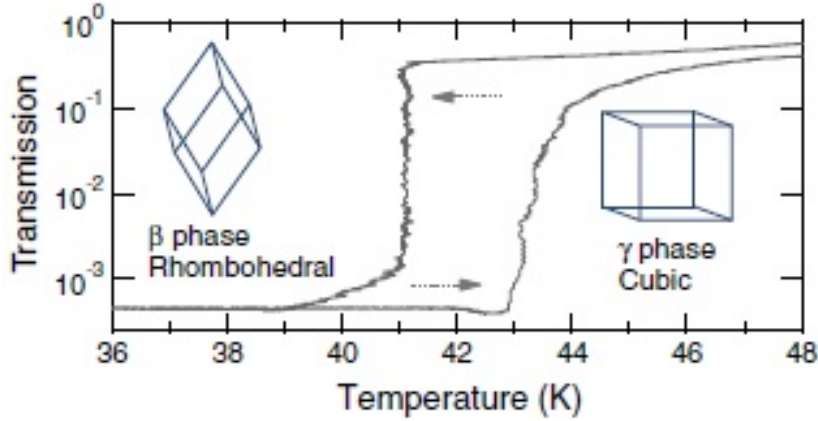


Fig. 72. Temperature dependence of the transmission of light near the  $\beta - \gamma$  phase transition. When the rhombohedral  $\beta$  phase is converted to the cubic  $\gamma$  phase, optical anisotropy disappears and the light scattering from the domain boundary is suppressed. (From Ref. [22].)

properties, which suppress the light scattering at the domain boundaries. The change in transmission can also be directly observed visually: the  $\beta$  phase looks opaque, like frosted glass, whereas the  $\gamma$  phase appears almost transparent. Because the light transmission observed at the magnetic field-induced transition (Fig. 70) and at the temperature driven  $\beta - \gamma$  transition (Fig. 72) are qualitatively similar, it was suggested [22] that the similar crystal structure changes take place from the anisotropic (rhombohedral in  $\beta$  phase or monoclinic in  $\alpha$  phase) to the isotropic cubic one. Both proposed explanations are rather plausible, but in the absence of a quantitative theory, the authors refrained from unambiguous conclusions.

#### 8.4 $H - T$ phase diagram

Recently, the magnetocaloric effect (MCE) technique, was developed for pulsed magnetic field measurements [139] which took into account the non-equilibrium conditions originating from the short duration of the pulse field. In the adiabatic MCE measurements, the  $T$ - $H$  relations are measured with the conserved total entropy (the isentropic curves). Thus the ultrahigh-field magnetization (STC technique) together with the MCE measurements made it possible to discuss the comprehensive magnetic-field-temperature ( $H$ - $T$ ) phase diagram of solid oxygen.

Nomura et al. [25] performed the MCE measurements of condensed oxygen in adiabatic conditions up to 56 T using pulsed magnetic fields. From the measured isentropes, the magnetic field dependencies of  $T_{\beta\gamma}$  and  $T_{\alpha\beta}$  phase boundaries were obtained (Fig. 73) and compared with that derived from the thermodynamical relations [25]. They are described by the magnetic Clausius-Clapeyron equation, relating the slope of the phase transition line with the entropy change:

$$dT_c/dH_c = -\Delta M/\Delta S = -\Delta\chi H/\Delta S. \quad (6)$$

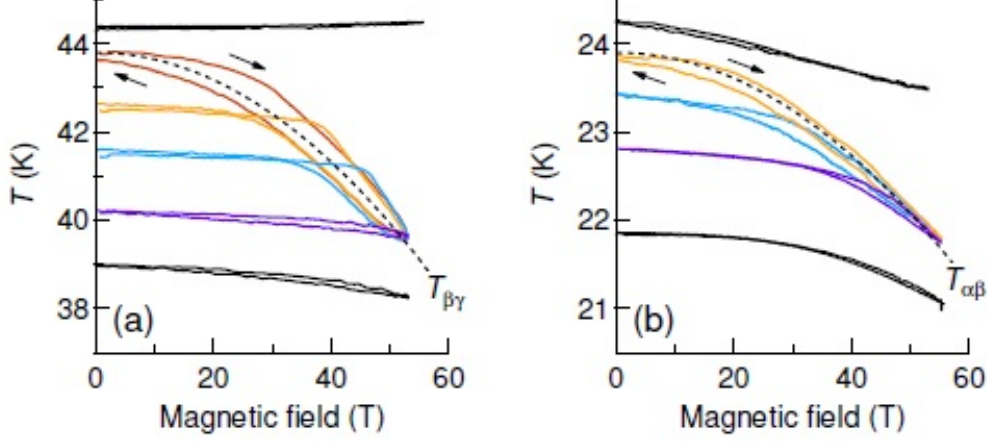


Fig. 73. (color online). MCE curves near the (a)  $\beta - \gamma$  and (b)  $\alpha - \beta$  phase boundaries [25].  $H$  dependences of the phase boundaries are shown by dotted curves. (From Ref. [25].)

Here,  $\Delta\chi$  is the difference of magnetic susceptibility between two phases. If the ratio  $\lambda = \Delta\chi/2S$  is independent on  $H$ , the Clausius-Clapeyron equation can be integrated giving the following equation:

$$T_c(H) = T_c(0) - \lambda H^2. \quad (7)$$

The  $\beta - \gamma$  phase boundary is well fitted by this formula as

$$T_{\beta\gamma}(H) = 43.8 - 1.55 \times 10^{-3} H^2 \text{ (K)}. \quad (8)$$

By using the parameters  $\Delta\chi$  and  $\Delta S$  known from literature:  $\Delta\chi_{\beta\gamma} = 51.2 \times 10^{-3} \text{ JT}^{-2} \text{ mol}^{-1}$  [140] and  $\Delta S_{\beta\gamma} = 16.9 \text{ JK}^{-1} \text{ mol}^{-1}$  [11], for  $\lambda$  at zero field we get

$$\lambda = 1.51 \times 10^{-3} \text{ KT}^2, \quad (9)$$

which is in good agreement with experiment.

In the case of the  $\alpha - \beta$  phase transition the following magnetic field dependence of the phase boundary was obtained in MCE experiments [25]:

$$T_{\alpha\beta}(H) = 23.9 - 0.73 \times 10^{-3} H^2 \text{ (K)}. \quad (10)$$

The comparison of the experimental phase boundary with that obtained theoretically [141] is less satisfactory than in the case of the  $\beta - \gamma$  transition. The theoretical estimate of  $\lambda$  is more than twice the experimental value. The root of this discrepancy lies in the fact that the  $\alpha - \beta$  transition has characteristics of the first- and second-order transitions [7], and the MCE curves near the  $\alpha - \beta$  phase boundary are more difficult to interpret.

Let us turn to the remaining phase boundaries. Important features of the phase diagram may be found from the entropy relations between phases [26]. As follows

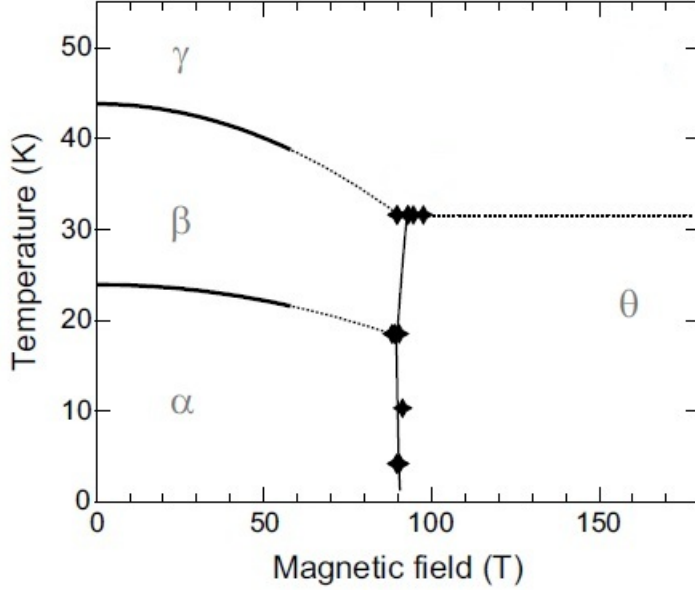


Fig. 74.  $H - T$  phase diagram of solid oxygen. (From Ref. [25].)

from the Clausius- Clapeyron equation (Eq. 6), large  $\Delta M$  and small  $\Delta S$  suggest steep phase lines, and conversely, small  $\Delta M$  and large  $\Delta S$  mean that the respective phase boundary is flat. The entropy relations between the  $\alpha$ ,  $\beta$ , and  $\gamma$  phases are  $S_\alpha < S_\beta \ll S_\gamma$  (at zero field  $\Delta S_{\alpha-\beta} = 0.47R$  and  $\Delta S_{\beta\gamma} = 2.04R$  [53]). Large  $\Delta S_{\theta\gamma}$  suggests that the the  $\theta - \gamma$  phase boundary is flat. The ultrahigh magnetic field region of the phase diagram contains two triple points:  $\beta - \gamma - \theta$  and  $\alpha - \beta - \theta$ . Knowledge of the coordinates of these points makes it possible to draw the  $\gamma - \theta$ ,  $\beta - \theta$  and  $\alpha - \theta$  phase boundary lines. At the  $\beta - \gamma - \theta$  triple point the  $\beta$  phase transforms entirely to the  $\theta$  phase which is detected in experiment. Similarly, at the  $\alpha - \beta - \theta$  triple point, both the  $\alpha$  and  $\beta$  phases transform to the  $\theta$  phase. Without explanations the authors write [26] that the  $\theta - \gamma$  transition (solid-plastic transition) is expected to occur at 31 K and that the thermodynamical  $\alpha - \theta$  transition field was obtained at around 90 T. The resulting  $H - T$  phase diagram of solid oxygen is shown in Fig. 74.

### 8.5 Concluding remarks

In this section we discussed results of experimental studies of solid oxygen in ultrahigh pulsed destructive magnetic fields of up to over 190 T performed by Nomura et al. group [22–26]. The thermodynamical magnetic-field-temperature  $H-T$  phase diagram of solid oxygen is discussed analyzing the results of the ultrahigh-field magnetization, optical magneto-transmission, and adiabatic magnetocaloric effect measurements taking into account the problems of non-equilibrium conditions originating from the short duration of the pulse field. An abrupt increase in magnetization and in light transmission in the visible range were observed when pulsed magnetic fields greater than  $\approx 90$  T were applied. These experimental findings indicated that the  $\alpha - \theta$ ,  $\beta - \theta$  first-order phase transitions occur in solid oxygen in

ultrahigh magnetic fields into a new  $\theta$  phase. The  $\alpha - \theta$ ,  $\beta - \theta$  transition fields are almost temperature independent, with the phase boundary being very steep indicating that the entropy change is very small at these transitions, in contrast to the entropy-driven  $\beta = \gamma$  transition at zero field. It was concluded that the observed field-induced transitions are caused by the antiferromagnetic phase collapsing and a change in the crystal structure with the rearrangement of the  $O_2$  molecules from the original parallel geometry into a high-symmetry crystal structure, that could be cubic, with a high magnetic susceptibility. The phase diagram was obtained by using the magnetic Clausius-Clapeyron equation. The obtained phase diagram manifests the entropy relation between the phases as  $S_\theta \sim S_\alpha < S_\beta \ll S_\gamma$ .

Recently, non-destructive ultrahigh magnetic fields have become accessible for researches in condensed matter physics. In the magnetic field of the 100 T range generated for few ms, various kinds of measurements such as x-ray diffraction, Raman, infrared, ultrasound, and magnetostriction would be applicable to obtain the structural and other necessary information of the  $\theta$  phase.

## 9 Summary and outlook

In 2004, we published a comprehensive review article "Solid Oxygen" (Yu.A. Freiman and H.J. Jodl, Physics Reports 401 (2004) 1-228) [7]. During the intervening years a large number of new studies of solid oxygen have been carried out and many new fundamental results have been obtained in this field. The current review article summarizes the most important results obtained during this time. The title of the review "Solid oxygen revisited" is chosen to emphasize the relationship with our previous review. As is usually the case most often, the studies that were described in the review have not exhausted the problems, but have induced new problems to be studied.

The content of this review is organized in the following way: the two first Sections are introductory - Section 1 gives a general chronological Table of the studies of solid oxygen which have been carried out during 2004 - 2017 years and which were reviewed in this paper; for completeness we consider in Section 2 the structures of low-pressure low-temperature  $\alpha$ ,  $\beta$ ,  $\gamma$ , and  $\delta$  phases which were discussed in the review [7].

Section 3 is devoted to the structure and behavior of lattice parameters with pressure (Sec. 3.1), and the nature of chemical bond in the  $\epsilon$  phase (Sec. 3.2). The efforts of nearly three decades of identifying the lattice structure of  $\epsilon$ - $O_2$  culminated in simultaneous publication in 2006 of results of two diamond anvil-cell x-ray diffraction studies [17,18]. It was discovered that in addition to the well-known  $O_2$  and  $O_3$  molecules existing in a free state, in solid oxygen pressurized up to 8 GPa another modification of oxygen exists, which can be described by the structural formula  $(O_2)_4$ . Lindegaard et al. [17] investigated monocrystalline samples while Fujihisa et al. [18] investigated polycrystalline powder samples. A unique structure of the  $\epsilon$

phase was found in which the molecules  $O_2$  retain their individuality, but there is an additional link leading to the formation of clusters of molecular quartets. Why this structure is formed from the quantum chemistry point of view we discuss in Sec. 3.2.

The insulator-metal transition and properties of the metallic  $\zeta$  phase is discussed in Section 4. We discuss mechanism of the  $\epsilon - \zeta$  phase transition and the evolution of the  $\zeta$  phase with pressure. A continuous displacive phase transition with pressure between 96 and 106 GPa takes place to a new structure. The vibron excitation data showed unambiguously that the  $\zeta$  phase is molecular. After the phase transition is completed the  $O_8$  units are turned out to be connected along the  $\mathbf{b}$  direction, so that the intra- and inter- $O_8$  distances became equal which means the dissociation of the two  $O_8$  units in the unit cell into the eight  $O_2$  molecules.

Section 5 is devoted to results of studies of the high-pressure high-temperature part of the phase diagram of solid  $O_2$ . These measurements become possible owing to the progress in the high-pressure experimental technique including the use of the third generation synchrotron sources for single-crystal diffractometry and the development of the DAC technique. Two new phases,  $\eta$  (Santoro et al. [12]), and  $\eta'$  (Goncharov et al. [14]) were found. The structure of  $\eta-O_2$  is closely related to the structure of  $\beta-O_2$ , other high-temperature structure though  $\eta$  phase is a two-layer hcp-like structure while  $\beta-O_2$  is a three-layer fcc-like structure. Above a certain temperature the rotational motion becomes so intensive that the rotational energy is in excess of the energy of molecular association and  $O_8$  units breaks up into four  $O_2$  molecules. Combined x-ray diffraction and Raman data suggest that the dissociation of  $O_8$  clusters is a signature of the phase transition into a new  $\eta'$  phase. This  $\epsilon - \eta'$  phase transition line is essentially pressure independent suggesting that the corresponding transition is entropy driven.

Section 6 is devoted to magnetism of solid oxygen. The unique feature of magnetism in solid oxygen, the only elemental magnet, is that the exchange interaction acts on the background of the weak van der Waals forces and thus providing a significant part of the total lattice energy. This feature is in fact the ground of all the anomalous properties of solid oxygen. One of them is the giant magnetostriction (Sec. 6.2). The dc magnetic susceptibility measurements at elevated pressures up to 3.3 GPa (the highest pressure accessible at present for the susceptibility measurements) are described in Sec. 6.3. Neutron measurements under pressure are the subject of Sec. 6.4. First neutron study of the  $\delta$  phase (Goncharenko et al., Ref. [27]) revealed the magnetic structure with the ferromagnetic interplane interaction instead of the expected antiferromagnetic that like in the  $\alpha$  phase. In subsequent neutron measurements it was found that magnetism of the  $\delta$  phase is generally unique (Klotz et al., Ref. [20]). Inside the same lattice structure of  $\delta-O_2$  there exist three different magnetic structures: LTC (low temperature commensurate) with the ferromagnetic (F) interplane coupling, HTC (high temperature commensurate) with the antiferromagnetic (AF) interplane coupling, and ITC (intermediate temperature commensurate) having a doubled period along the  $c$ -axis as compared to the LTC and HTC structures. The F and AF coupling between the nearest neighbor spins in the adjacent  $O_2$  planes

form the alternate sequence F-AF-F-AF. Section 6.5 describes the magnetic collapse at the  $\delta - \epsilon$  transition (Goncharenko, Ref. [21]) revealed by the disappearance of the magnetic peaks in the neutron diffraction pattern. The absence of the magnetic reflections indicates the absence of the long-range magnetic order in the  $\epsilon$  phase. The magnetic collapse occurs at 8 GPa, that is, this phenomenon is well separated from the  $\epsilon - \zeta$  (insulator - metal) phase transition at 96 GPa. Section 6.6 is devoted to numerous anomalous spectroscopic features displaying in the lower-pressure part of the  $\epsilon$ -O<sub>2</sub> region of the oxygen phase diagram. The failure of theory to describe these anomalies disregarding molecular spin suggested (Crespo et al., Ref. [45]) that there is no the single broad  $\epsilon$ -O<sub>2</sub> phase from 8 to 96 GPa but instead we have two phases  $\epsilon_1$ -O<sub>2</sub> and  $\epsilon_0$ -O<sub>2</sub> – the former a local singlet spin-1 liquid, and the latter a regular, Peierls band insulator – separated by a first-order phase transition near 20 GPa. The predicted phase line terminates in a critical point, which supposedly lies near 30 GPa and 200 K. The high-temperature region below 30 GPa must be characterized by thermally fluctuating  $S = 1$  spins, whose presence should be directly detectable by magnetic susceptibility measurements in the 8- to 30-GPa pressure range when such experiments become technically feasible (see Sec. 6.3). At low temperatures, the wealth of low-energy spin excitations present in  $\epsilon_1$ -O<sub>2</sub> but absent in  $\epsilon_0$ -O<sub>2</sub> should give rise to very new energy dissipation channels and processes in the former phase.

In Sec. 7 merits and limitations of commonly used methods for identifying the beginning of melting are analyzed. These methods include an analysis of Bragg reflections in x-ray diffraction, appearance of jumps or changes in the slope of Raman vibron modes as a function of pressure and temperature, and visual observation of fluid flow or laser spackle. The conclusion drawn from this analysis was that simultaneously monitoring both structural and spectral properties is superior to any single method for identifying the onset of melting. At present, the oxygen melting line is extended up to 60 GPa, 1750 K (Goncharov et al., Ref. [14]) with the x-ray diffraction and Raman spectroscopy by using resistively- and laser-heated diamond anvil cells. In the region around 20 GPa the laser-heating method does not work because of strong fluorescence from liquid oxygen. Due to this experimental problem the uncertainties in the phase boundaries between liquid,  $\beta$ ,  $\epsilon$ ,  $\eta$ , and  $\eta'$  in the range 16 - 25 GPa are not properly resolved.

In Sec. 8 results of experimental studies of solid oxygen (at ambient pressure) in ultrahigh pulsed destructive magnetic fields of up to over 190 T are discussed. The thermodynamical magnetic field – temperature  $H$ - $T$  phase diagram of solid oxygen is discussed analyzing the results of the ultrahigh-field magnetization, optical magneto-transmission, and adiabatic magnetocaloric effect measurements taking into account the problems of non-equilibrium conditions originating from the short duration of the pulse field. It was found that  $\alpha - \theta$  and  $\beta - \theta$  first-order phase transitions occur in solid oxygen in ultrahigh magnetic fields into a new  $\theta$  phase. The observed field-induced transitions are caused by the antiferromagnetic phase collapsing and a change in the crystal structure with the rearrangement of the O<sub>2</sub> molecules from the original parallel geometry into a high-symmetry crystal structure, that could be cubic, with a high magnetic susceptibility.

Investigations of solid oxygen in ultrahigh pulsed destructive magnetic fields culminated in the construction of the  $H - T$  magnetic field - temperature phase diagram at ambient pressure. Recently non-destructive ultrahigh magnetic fields have become accessible for research in condensed matter physics. In the magnetic field in the 100 T range generated for few ms, various kinds of measurements such as x-ray diffraction, Raman, infrared, ultrasound, and magnetostriction would be applicable to obtain the structural and other necessary information of the  $\theta$  phase. The ultrahigh magnetic field technique combined with the DAC technique would open access to the construction of the complete  $H$ - $P$ - $T$  phase diagram of solid oxygen. The implementation of this exciting program can take many years, creating new instrumentation and possibly the next generation of researchers.

## Acknowledgements

A somewhat unusual idea of writing this review as a continuation of our review of 2004 have been supported by Professor Michael L. Klein. We would like to acknowledge many colleagues for numerous fruitful discussions and enlightening comments of their own results in the field: Alexander Goncharov, Stefan Klotz, Erio Tosatti, Roberto Bini, Federico Gorelli, Mario Santoro.

The authors have no competing interests to declare.

## References

- [1] William Ramsay. The gases of the atmosphere (the history of their discovery), MacMillan and Co. London, 1896.
- [2] Carl Djerassi and Roald Hoffmann, Oxygen, Wiley VCH, 2001.
- [3] M. Faraday. Selected papers
- [4] T. Estreicher, Bull. Int. de. l'Acad. Des Sciences de Cracovia, 1903, 836.
- [5] I.A. Burakhovich, I.N. Krupskii, A.I. Prokhvatilov, Yu.A. Freiman, A.I. Erenburg, JETP Lett. **25** (1977) 33.
- [6] I.N. Krupskii, A.I. Prokhvatilov, Yu.A. Freiman, A.I. Erenburg, Sov. J. Low Temp. **5** (1979) 130.
- [7] Yu.A. Freiman, H.J. Jodl, Physics Reports **401** (2004) 1.
- [8] E.J. Wachtel, R.G. Wheeler, Phys. Rev. Lett. **24** (1970) 233.
- [9] Yu.B. Gaididei, V.M. Loktev, Sov. Phys. - Solid State **16** (1975) 2226.
- [10] A.S. Borovik-Romanov, M.P. Orlova, P.G. Strelkov, DAN USSR **99** (1954) 699.
- [11] C.H. Fagerstroem, A.C. Hollis Hallett, J. Low Temp. Phys. **1** (1969) 3.
- [12] M. Santoro, E. Gregoryanz, H.-k. Mao, R. J. Hemley, Phys. Rev. Lett **93** (2004) 265701.

- [13] G. Weck, S. Desgreniers, P. Loubeyre, M. Mezouar, Phys. Rev. Lett. **102** (2009) 255503.
- [14] Alexander F. Goncharov, N. Subramanian, T.R. Ravindran, Maddury Somayazulu, Vitali B. Prakapenka, Russell J. Hemley, J. Chem. Phys. **135** (2011) 084512.
- [15] Jian Sun, M. Martinez-Canales, D.D. Klug, C.J. Pickard, R.J. Needs, Phys. Rev. Lett. **108** (2012) 045503.
- [16] Alan P. Lightman, The discoveries: great breakthroughs in twentieth-century science, including the original papers. Toronto: Alfred A. Knopf Canada.
- [17] L.F. Lundegaard, G. Weck, M.I. McMahon, S. Desgreniers, P. Loubeyre, Nature **443** (2006) 201.
- [18] H. Fujihisa, Y. Akahama, H. Kawamura, Y. Ohishi, O. Shimomura, H. Yamawaki, M. Sakashita, Y. Gotoh, S. Takeya, K. Honda, Phys. Rev. Lett. **97** (2006) 085503.
- [19] L.F. Lundegaard, C. Guillaume, M.I. McMahon, E. Gregoryanz, M. Merlini, J. Chem. Physics **130** (2009) 164516.
- [20] S. Klotz, Th. Strassle, A.L. Cornelius, J. Philippe, Th. Hansen, Phys. Rev. Lett. **104** (2010) 115501.
- [21] I.N. Goncharenko, Phys. Rev. Lett. **94** (2005) 205701.
- [22] T. Nomura, Y.H. Matsuda, S. Takeyama, A. Matsuo, K. Kindo, Phys. Rev. Lett **112** (2014) 247201.
- [23] T. Nomura, Y.H. Matsuda, S. Takeyama, A. Matsuo, K. Kindo, T.C. Kobayashi, Phys. Rev. **B 92** (2015) 064109.
- [24] T. Nomura, Y.H. Matsuda, S. Takeyama, T.C. Kobayashi, J. Phys. Soc. Jpn. **85** (2016) 094601.
- [25] T. Nomura, Y. Kohama, Y.H. Matsuda, K. Kindo, T.C. Kobayashi, Phys. Rev. **B 95** (2017) 064109.
- [26] T. Nomura, Y.H. Matsuda, T.C. Kobayashi, ArXiv, May29, 2017.
- [27] I.N. Goncharenko, O.L.Makarova, L. Ulivi, Phys. Rev. Lett. **93** (2004) 055502.
- [28] Jrg Kreutz, Sergey A. Medvedev, Hans J. Jodl, Phys. Rev. **B 72** (2005) 214115.
- [29] G. Weck, P. Loubeyre, J.H. Eggert, M. Mezouar, M. Hanfland, Phys. Rev. **B 76** (2007) 054121.
- [30] Y. Ma, A.R. Oganov, C.W. Glass, Phys. Rev. **B 76** (2007) 064101.
- [31] E.V. Gomonay, V.M. Loktev, Phys. Rev. **B 76** (2007) 094423.
- [32] R. Steudel and MingWah Wong, Angew. Chem. Int. Ed. **46** (2007) 1768.
- [33] F. Gorelli, M. Santoro, R. Bini, L. Ulivi, Phys. Rev. **B 77** (2008) 132103.
- [34] Yue Meng, P.J. Eng, J.S. Tse, D.M. Shaw, M.Y. Hu, J. Shu, S.A. Gramsch, C.-ch. Kao, R.J. Hemley, H.-k. Mao, PNAS **105** (2008) 11640.

- [35] D.Y. Kim, S. Lebègue, C.M. Araújo, B. Arnaud, *Phys. Rev. B* **77** (2008) 092104.
- [36] J.S. Tse, Y. Yao, D.D. Klug, S. Desgreniers, *J. Phys.: Confer. Series* **121** (2008) 012006.
- [37] L.R. Benedetti, D. Antonangeli, D.L. Farber, M. Mezouar, *Appl. Phys. Lett.* **92** (2008) 141903.
- [38] T. Anh Pham, R. Gebauer, S. Scandolo, *Solid State Commun.* **149** (2009) 160.
- [39] H. Katzke, P. Toledano, *Phys. Rev. B* **79** (2009) 140101R.
- [40] E.V. Gomonay, V.M. Loktev, *Phys. Rev. B* **82** (2010) 134422.
- [41] M. Bartolomei, E. Carmona-Novillo, M.I. Hernandez, Jesus Perez-Ríos, Jose Campos-Martínez, *Phys. Rev. B* **84** (2011) 092105.
- [42] T. Ishikawa, K. Mukai, K. Shimizu, *High Pressure Research* **32** (2012) 457.
- [43] M.A. Garcia-Revilla, E. Francisco, A. Martin Penda, J.M. Recio, M. Bartolomei, M.I. Hernandez, J. Campos-Martinez, E. Carmona-Novillo, R. Hernandez-Lamoneda, *J. Chem. Theory and Comput.* **9** (2013) 2179.
- [44] M. Mito, S. Yamaguchi, H. Tsuruda, H. Deguchi, M. Ishizuka, *J. Applied Phys.* **115** (2014) 013903.
- [45] Yanier Crespo, Michele Fabriziob, Sandro Scandolo, Erio Tosatti, *PNAS* **111** (2014) 10427.
- [46] A.J. Ochoa-Calle, C.M. Zicovich-Wilson, A. Ramirez-Solis, *Chem. Phys. Lett.* **638** (2015) 82.
- [47] Yu.A. Freiman, *Magnetic properties of solid oxygen under pressure, Low Temperature Physics* **41** (2015) 847.
- [48] B.H Cogollo-Olivo, J.A. Montoya, *J. Phys.: Conf. Ser.* **743** (2016) 012001.
- [49] A. Ramirez-Solis, C.M. Zicovich-Wilson, R. Hernandez-Lamoneda, A. J. Ochoa-Calle, *Phys. Chem. Chem. Phys.* **19** (2017) 2826.
- [50] K. Shimizu, K. Suhara, M. Ikumo, M.I. Eremets, K. Amaya, *Nature* **393** (1998) 767.
- [51] C.S. Barrett, L. Meyer, J. Wassermann, *J. Chem. Phys.* **47** (1967) 592.
- [52] J. Dewar, *Proc. Roy. Soc. (London)* **A 50** (1891) 10.
- [53] W. Giauque, H. Johnston, *J. Amer. Chem. Soc.* **51** (1929) 2300.
- [54] R.A. Alikhanov, *Zh. Eksp. Teor. Fiz.* **45** (1963) 812 (Engl. Transl. *JETP* **18** (1964) 556; R.A. Alikhanov in: *Proceedings of the Third Region Conference on Physics and Technics of Low Temperatures, Prague, 1963*, p. 127.
- [55] R.A. Alikhanov, *JETP Lett.* **5** (1967) 349.
- [56] M.F. Collins, *Proc. Phys. Soc.* **89** (1966) 415.
- [57] M. Nicol, K.R. Hirsch, W.B. Holzapfel, *Chem. Phys. Lett.* **68** (1979) 49.
- [58] D. Schiferl, S.W. Johnson, A.S. Zinn, *High Pressure Res.* **4** (1990) 293.

- [59] B. Olinger, R.L. Mills, R.B. Roof Jr., J. Chem. Phys. **81** (1984) 5086.
- [60] Yu. Akahama, H. Kawamura, D. Hausermann, M. Hanfland, O. Shimomura, Phys. Rev. Lett. **74** (1995) 4690.
- [61] Y. Akahama, H. Kawamura, Phys. Rev. B **61** (2000) 8801.
- [62] F. Gorelli, M. Santoro, L. Ulivi, R. Bini, Physica B **265** (1999) 49.
- [63] F. Gorelli, L. Ulivi, M. Santoro, R. Bini, Phys. Rev. Lett. **83** (1999) 4093.
- [64] F. Gorelli, L. Ulivi, M. Santoro, R. Bini, Phys. Rev. B **60** (1999) 6179.
- [65] F. Gorelli, L. Ulivi, M. Santoro, R. Bini, Phys. Rev. **B 63** (2001) 104110.
- [66] M. Santoro, F. Gorelli, L. Ulivi, R. Bini, H.J. Jodl, Phys. Rev. **B 64** (2001) 064428.
- [67] Yu. Akahama, H. Kawamura, Phys. Rev. **B 54**, (1996) 15602.
- [68] J. Yen, M. Nicol, J. Phys. Chem. **91** (1987) 3336.
- [69] S. Desgreniers, Y. Vohra, A. Ruoff, J. Phys. Chem. **94** (1990) 1117.
- [70] A.L. Ruoff, S. Desgreniers, Very high density solid oxygen: indications of a metallic state, in: R. Pucchi, G. Piccitto (Eds.), Molecular Systems Under High Pressure, North-Holland, Amsterdam, 1991.
- [71] G. Weck, P. Loubeyre, R. LeToullec, Phys. Rev. Lett. **88** (2002) 035504.
- [72] S.W. Johnson, M. Nicol, D. Schiferl, J. Appl. Crystallogr. **26** (1993) 320.
- [73] S. Desgreniers, K.E. Brister, in: W.A. Treziakowski (Ed.), High Pressure Science and Technology, World Scientific, Singapore, 1996.
- [74] Y. Akahama, H. Kawamura, O. Shimomura, Phys. Rev. **B 64** (2001) 054105.
- [75] D. Schiferl, D.T. Cromer, R.L. Mills, Acta Cryst. **B 37** (1981) 1329.
- [76] D. Schiferl, D.T. Cromer, L.A. Schwalbe, R.L. Mills, Acta. Cryst. **B 39** (1983) 153.
- [77] Y. Yao, Thesis "Structures, Bonding and Transport Properties of High Pressure Solids", University of Saskatchewan, Saskatoon, 2008.
- [78] S.F. Agnew, B.I. Swanson, L.H. Jones, J. Chem. Phys. **86** (1987) 5239.
- [79] C.A. Long, G.E. Ewing, J. Chem. Phys. **58** (1973) 4824.
- [80] V. Aquilanti, D. Ascenzi, M. Bartolomei, D. Cappelletti, S. Cavalli, M. de Castro Vtores, F. Pirani Phys. Rev. Lett. **82** (1999) 69.
- [81] J.G. Goodman, L.E. Brus, J. Chem. Phys. **67** (1977) 4398.
- [82] Pauling, L. The Nature of the Chemical Bond (Cornell Univ. Press, Ithaca, New York, 1964)
- [83] P.E.S. Wormer, A. van der Avoird, J. Chem. Phys. **81** (1984) 1929.
- [84] R.F.W. Bader, *Atoms in Molecules A Quantum Theory*, Oxford, Oxford University Press, 1990.

- [85] J.S. Tse, E.V. Boldyreva, Electron Density Topology of Crystalline Solids at High Pressure (Eds.: C. Gatti and P. Macchi). In: Modern Charge-Density Analysis, Ch. 17 (pp. 573 - 623), Springer 2012.
- [86] K. Shimizu, K. Suhara, M. Ikumo, K. Amaya, S. Endo, J. Phys. Soc. Jpn. **65** (1996) 1527.
- [87] A.F. Goncharov, E. Gregoryanz, R.J. Hemley, H.-k. Mao, Phys. Rev. **B 68** (2003) 100102(R).
- [88] S. Serra, G. Chiarotti, S. Scandolo, E. Tosatti, Phys. Rev. Lett. **80** (1998) 5160.
- [89] F. Datchi, G. Weck, Z. Kristallogr. **229** (2014) 135.
- [90] V.G. Manzhelii, Yu.A. Freiman, Physics of Cryocrystals (American Institute of Physics, Woodbury, New York, 1996). English Language Version edited Michael L. Klein, Alexei A. Maradudin.
- [91] M.I. Eremets A.G. Gavriliuk, I.A. Trojan, D.A. Dzivenko, R. Boehler, Nature Mater. **3** (2004) 558.
- [92] L.N. Yakub, Low Temp. Phys. **42** (2016) 1. (Fi. Nizk. Temp. **42** (2016) 3)
- [93] O. Degtyareva, E. Gregoryanz, M. Somayazulu, P. Dera, Ho-kwang Mao, R.J. Hemley, Nature Mater. **4** (2005) 152.
- [94] T. Yagi, K.R. Hirsch, W.B. Holzapfel, J. Chem. Physics **87** (1983) 2272.
- [95] A.F. Goncharov, P. Beck, V.V. Struzhkin, R.J. Hemley, J.C. Crowhurst, J. Phys. Chem. Solids **69** (2008) 2217.
- [96] R. Boehler, K. De Hantsetters, High Press. Res. **24** (2004) 391.
- [97] G. Weck, Oral Presentation, European High-Pressure Research Group (EHPRG) Conference, Valencia, Spain, 2008 (unpublished).
- [98] E. Uemura, Y. Akahama, H. Kawamura, T. Le Bihan, T. Shobu, Y. Noda, O. Shimomura, J. Phys.: Condens. Matter **14** (2002) 10423.
- [99] Yu.A. Freiman, S.M. Tretyak, A. Jezowski, R.J. Hemley. J. Low Temp. Phys. **113** (1998) 723.
- [100] Yu.A. Freiman, Y. Crespo, Low Temp.Phys. **43** (2017) (Fiz. Nizk. Temp. **43** (2017) 1687.
- [101] H. Kamerlingh Onnes, A. Perrer, Leiden Commun. **16** (1910) 1.
- [102] V.A.Slusarev, Yu.A. Freiman, R.P. Yankelevich JETP Lett. **30** (1979) 270.
- [103] V.A.Slusarev, Yu.A. Freiman, R.P. Yankelevich Sov. J. Low Temp. Phys. **6** (1980) 105.
- [104] Yu.B. Gaididei, V.M. Loktev, Sov. J. Low Temp. Phys. **7** (1981) 634.
- [105] K. Katsumata, S. Kimura, U. Staub, Y. Narumi, Y. Tanaka, S. Shimomura, T. Nakamura, S.W. Lovesey, T. Ishikawa, H. Kitamura J. Phys. Cond. Matt. **17** (2005) L235.

- [106] V.G. Bar'yakhtar, V.M. Loktev, S.M. Ryabchenko, *Sov. Phys.Solid State* **28** (1986) 801.
- [107] R.J. Meier, C.J. Schinkel, A. de Visser. *J. Phys. C: Solid State Phys.* **15** (1982) 1015.
- [108] M. Ishizuka, unpublished data, cited in Ref. [44].
- [109] F. Gorelli, M. Santoro, L. Ulivi, M. Hanfland, *Phys. Rev.* **B 65** (2002) 172106.
- [110] H.J. Jodl, F. Bolduan, H.D. Hochheimer, *Phys. Rev.* **B 31** (1985) 7376.
- [111] R.L. Mills, E.R. Grilly, *Phys. Rev.* **99** (1985) 480.
- [112] I. Mirebeau, J.-M. Mignot, *High Pressure Res.* **28** (2008) 141.
- [113] Yu.A. Freiman, *Sov. J. Low Temp. Phys.* **16** (1990) 559.
- [114] I.N. Goncharenko, *High Pressure Res.* **28** (2004) 193.
- [115] S. Klotz, *J. Low Temp. Phys.* (2018) To be publish.
- [116] L.D. Landau, E.M Lifshitz, *Statistical Physics*,, third ed. , Pt. 1, Pergamon Press, Oxford, 1980.
- [117] R.D. Eppers, K. Kobashi, J. Belak, *Phys. Rev.* **B 32** (1985) 4097.
- [118] B. Militzer, R.J. Hemley, *Nature* **443** (2006) 150.
- [119] W.B. Carter, D. Schiferl, M. Lowe, D. Gonzales, *J. Phys. Chem.* **95** (1991) 2516.
- [120] V.I. Anisimov, J. Zaanen, O.K. Andersen, *Phys. Rev.* **B 44** (1991) 943.
- [121] A.F. Goncharov, Private communication.
- [122] A. Helmy, K. Kobashi, R.D. Eppers, *J. Chem. Phys.* **80** (1984) 2782.
- [123] A. Helmy, K. Kobashi, R.D. Eppers, *J. Chem. Phys. Errata:* **82** (1985) 473. 18.
- [124] D.A. Young, C.-S. Zha, R. Boehler, J. Yen, M. Nicol, A.S. Zinn, D. Schiferl, S. Kinkead, R.C. Hanson and D.A. Pinnick, *Phys. Rev.* **B 35** (1987) 5353.
- [125] E. Gregoryanz, A.F. Goncharov, R.J. Hemley, H.-k. Mao, M. Somayazulu, *Guoyin Shen Phys. Rev.* **B 66**, 224108 (2002).
- [126] E. Gregoryanz, A.F. Goncharov, K. Matsuishi, H.-k. Mao, R.J. Hemley *Phys. Rev. Lett.* **90** (2003) 175701.
- [127] F. Datchi, P. Loubeyre, R. LeToullec, *Phys. Rev.* **B 61** (2000) 6535.
- [128] F. Simon, G. Glatzel, *Z. Anorg. Allg. Chem.* **178** (1929) 309.
- [129] R.J. Meier, J.H. Colpa, H. Sigg, *J. Phys. C: Solid State Phys.* **17** (1984) 4501.
- [130] C. Uyeda, K. Sugiyama, M. Date, *J. Phys. Soc. Jap.* **54** (1985) 1107.
- [131] M.C. van Hemert, P.E.S. Wormer, A. van der Avoird, *Phys. Rev. Lett.* **51** (1983) 1167.
- [132] B. Bussery, P.E.S. Wormer, *J. Chem. Phys.* **99** (1993) 1230.

- [133] T. Nomura, Y.H. Matsuda, J.L. Her, S. Takeyama, A. Matsuo, K. Kindo, T.C. Kobayashi, *J. Low Temp. Phys.* **170** (2013) 372.
- [134] A. Hori, T. Yamaguchi, T.C. Kobayashi, A. Matsuo, K. Kindo, D. Tanaka, S. Kitagawa, *J. Low Temp. Phys.* **150** (2013) 122.
- [135] Y.B. Gaididei, V.M. Loktev, A.F. Prikhotko, L.I. Shanskii, *Phys. Stat. Sol. B* **72** (1975) 795.
- [136] Y.B. Gaididei, V.M. Loktev, A.F. Prikhotko, L.I. Shanskii, *Phys. Stat. Sol. B* **73** (1976) 415.
- [137] T. Fujiwara, *J. Phys. Soc. Jpn.* **36** (1974) 1530.
- [138] Y.G. Litvinenko, V.V. Eremenko, T.I. Garber, *Phys. Stat. Sol. B* **30** (1968) 49.
- [139] T. Kihara, Y. Kohama, Y. Hashimoto, S. Katsumoto, M. Tokunaga, *Rev. Sci. Instrum.* **84** (2013) 074901.
- [140] G.C. DeFotis, *Phys. Rev. B* **23** (1981) 4714.
- [141] A.P.J. Jansen, A. van der Avoird, *J. Chem. Phys.* **86** (1987) 3597.
- [142] Yu.A. Freiman, H.J. Jodl, Y. Crespo, *Physics Reports* (2018) To be published.